12-2014

The Role of Channel-Land Architecture, Diffusion Media Transport Properties, and Aging Effects on Water Transport and Storage in Polymer Electrolyte Fuel Cells

Jacob Michael LaManna
University of Tennessee - Knoxville, jlamann1@vols.utk.edu

Recommended Citation

To the Graduate Council:

I am submitting herewith a dissertation written by Jacob Michael LaManna entitled "The Role of Channel-Land Architecture, Diffusion Media Transport Properties, and Aging Effects on Water Transport and Storage in Polymer Electrolyte Fuel Cells." I have examined the final electronic copy of this dissertation for form and content and recommend that it be accepted in partial fulfillment of the requirements for the degree of Doctor of Philosophy, with a major in Mechanical Engineering.

Matthew M. Mench, Major Professor

We have read this dissertation and recommend its acceptance:

Feng-Yuan Zhang, Subhadeep Chakraborty, Thomas A. Zawodzinski

Accepted for the Council:
Carolyn R. Hodges

Vice Provost and Dean of the Graduate School

(Original signatures are on file with official student records.)

The Role of Channel-Land Architecture, Diffusion Media Transport Properties, and Aging Effects on Water Transport and Storage in Polymer Electrolyte Fuel Cells

A Dissertation Presented for the
Doctor of Philosophy
Degree
The University of Tennessee, Knoxville

Jacob Michael LaManna
December 2014

ACKNOWLEDGEMENTS

I owe a great deal of thanks to my wife, Sarah, for her continuous support of my endeavors and pushing me through. I would like to thank my parents and family for their encouragement and support. I would like to thank my advisor Dr. Mench for his mentoring, the opportunities that he provided, and asking me to join his group at UTK. To all of my lab mates in the Electrochemical Energy Storage and Conversion Laboratory, I have enjoyed my time working with you immensely. I would like to thank General Motors Electrochemical Energy Research Laboratory for their countless discussions, materials, and expertise that helped to complete this project. Many thanks to Dr. Dan Hussey and Dr. David Jacobson of the NIST Center for Neutron Research for their aid and discussion in developing, running, and analyzing the neutron imaging experiments.

ABSTRACT

Thermally driven transport of water vapor in polymer electrolyte fuel cells, also known as the heat-pipe effect or phase-change-induced flow, can transport several times the generated amount of water given enough temperature differentials. Understanding this transport process is necessary to properly engineer the water balance in the fuel cell to ensure high performance and long operational life. Channel-land architecture, diffusion media heat and mass transport properties, and operational age can all have an influence on thermally driven flow. High resolution neutron imaging was used to determine the steady-state water accumulation in various cell configurations to understand the influence of these parameters. A novel non-dimensional parameter was proposed to predict the influence of engineering parameters on water balance. The thermal transport number (TTN) compares the strength of anode and cathode thermally driven flow to determine a bias for transport to the anode. Channel-land architecture, specifically asymmetric flow field patterns with larger anode lands, was found to pump water to the anode and allow for large accumulations of water with saturation approaching 60%. Water transport was facilitated to the anode by a delta-T inversion caused by the insulating effect of the cathode gas channel located opposite of the center of the large anode land. To limit anode water accumulation, a new experimental high diffusion resistance anode diffusion media was evaluated. This material was found to be effective at reducing anode water accumulation primarily due to the increased tortuosity of the material but also due to the higher thermal conductivity reducing the thermal transport effect. Material age was shown to reduce cell water content due to increased hydrophilic nature and increased thermal conductivity that increased from

inlet to outlet with greater effects on the anode. A parametric study was performed to determine what parameters have the strongest influence on thermally driven transport. It was found that porosity and tortuosity of the diffusion media, and channel-land architecture can be engineered to drive water balance in a favorable direction. Temperature and thermal conductivity primarily influence the strength of thermal transport. This work demonstrated methods to properly design thermal management for optimized and predictive water transport.

TABLE OF CONTENTS

LIST OF TABLES

LIST OF FIGURES

CHAPTER 1:   Introduction

1.1 Background and General Information

Polymer electrolyte fuel cells (PEFC), also known as polymer electrolyte membrane fuel cells (PEMFC), are electrochemical energy conversion devices that convert hydrogen and oxygen gas into water and electricity. William Grove first invented fuel cells in 1839 [1] which he called a gas voltaic battery. This system used platinum and zinc electrodes to convert hydrogen and oxygen gas into electricity. Due to the low surface area of the electrodes, performance was poor and interests in fuel cells diminished. It wasn't until the Cold War and the Space Race between the United States of America and the U.S.S.R that reignited interests in fuel cells to power spacecraft. The NASA Project Gemini was the first program to use PEFCs in space as batteries could not provide the longevity required for the endurance missions lasting up to 14 days [2]. Because of reliability issues with PEFC cells of the time, NASA elected to use alkaline fuel cells in their Apollo and Shuttle spacecraft.

Today, PEFCs are seen as a viable alternative to internal combustion engines (ICE) used in the automotive sector after interest was rekindled in the early 1980's when a breakthrough significantly reduced precious medal loadings [2, 3]. The need to reduce foreign energy dependence and fossil fuel emissions has put significant research emphasis on fuel cells. PEFCs are the fuel cell technology of choice due to their low temperatures, rapid start-up, and relative high performance compared to other fuel cell technologies, see Table 1-1. To be competitive with current ICE technology and performance, significant research has had to go into increasing performance and reliability while reducing costs of PEFCs.

Table 1-1: Advantages and disadvantages of different fuel cell types for automotive applications.

Fuel Cell Type	Electrolyte	Exchanged Ion	Temperature [°C]	Advantages	Disadvantages
Polymer Electrolyte Fuel Cell	Solid polymer membrane, i.e. Nafion	H^+	50-100	Low temperature, fast startup, high efficiency, high power density	Corrosive environment, liquid water removal, expensive catalyst
Solid Oxide Fuel Cell	Solid ceramic, i.e. yttria stabilized zirconia	O^{-2}	500-1100	Fuel flexibility, high-quality waste heat, non-noble catalyst, CO tolerant	Long startup time, poor durability under thermal cycling, poor electrolyte conductivity below ~600°C
Phosphoric Acid Fuel Cell	Liquid phosphoric acid	H^+	150-200	Some CO tolerance, moderate-quality waste heat, proven durability	Low power density, high platinum loading, slow startup, loss of electrolyte
Alkaline Fuel Cell	alkaline solution, i.e. potassium hydroxide	OH^-	<80	High efficiency, improved environment for metal components, low ORR losses	Must run pure oxygen, loss of electrolyte, CO_2 contamination
Direct Methanol Fuel Cell	Solid polymer membrane, i.e. Nafion	H^+	90-120	High energy density fuel, easier refueling	low efficiency, high platinum loadings
Molten Carbonate Fuel Cell	Molten carbonate salt	CO_3^{-2}	600-650	Fuel flexibility, high-quality waste heat, non-noble catalyst, CO tolerant	Electrolyte dissolves cathode catalyst, long startup, CO2 injection required on cathode, electrolyte maintenance

1.2 Polymer Electrolyte Fuel Cell Overview

1.2.1 PEFC Overview

A PEFC consists of two halves, the anode and cathode, which are separated by a proton conducting polymer membrane. Located on either side of the membrane are the catalyst layers, diffusion media, flow fields, and current collectors as shown in Figure 1-1. Hydrogen gas flows through the channels in the anode flow field where it diffuses through the DM to the anode catalyst layer where it reacts with the catalyst to form protons and electrons. The membrane has high ionic conductivity and low electronic conductivity, thus the electrons must conduct back through the DM and flow field to the external circuit while the protons transport through the membrane. On the cathode side, oxygen (usually in air) enters through the flow channels and diffuses through the DM to the cathode catalyst layer. When oxygen, protons, and electrons meet on the cathode catalyst, water, heat, and electricity is produced. Detailed descriptions of the above components and electrochemical reaction will be discussed in detail in the follow paragraphs.

1.2.2 PEFC Membrane

The membrane is the critical component that separates the two halves of the cell and allows a fuel cell to generate electricity. To do this, the membrane must be electronically nonconductive, ionically conductive, relatively impermeable to gas phase transport. Typically, the membrane is made from Nafion, a polytetrafluoroethylene (PTFE) and polysulfonyl fluoride vinyl ether copolymer. The PTFE acts as a chemically inert support structure for the sulfonic acid groups. These groups are hydrophilic and
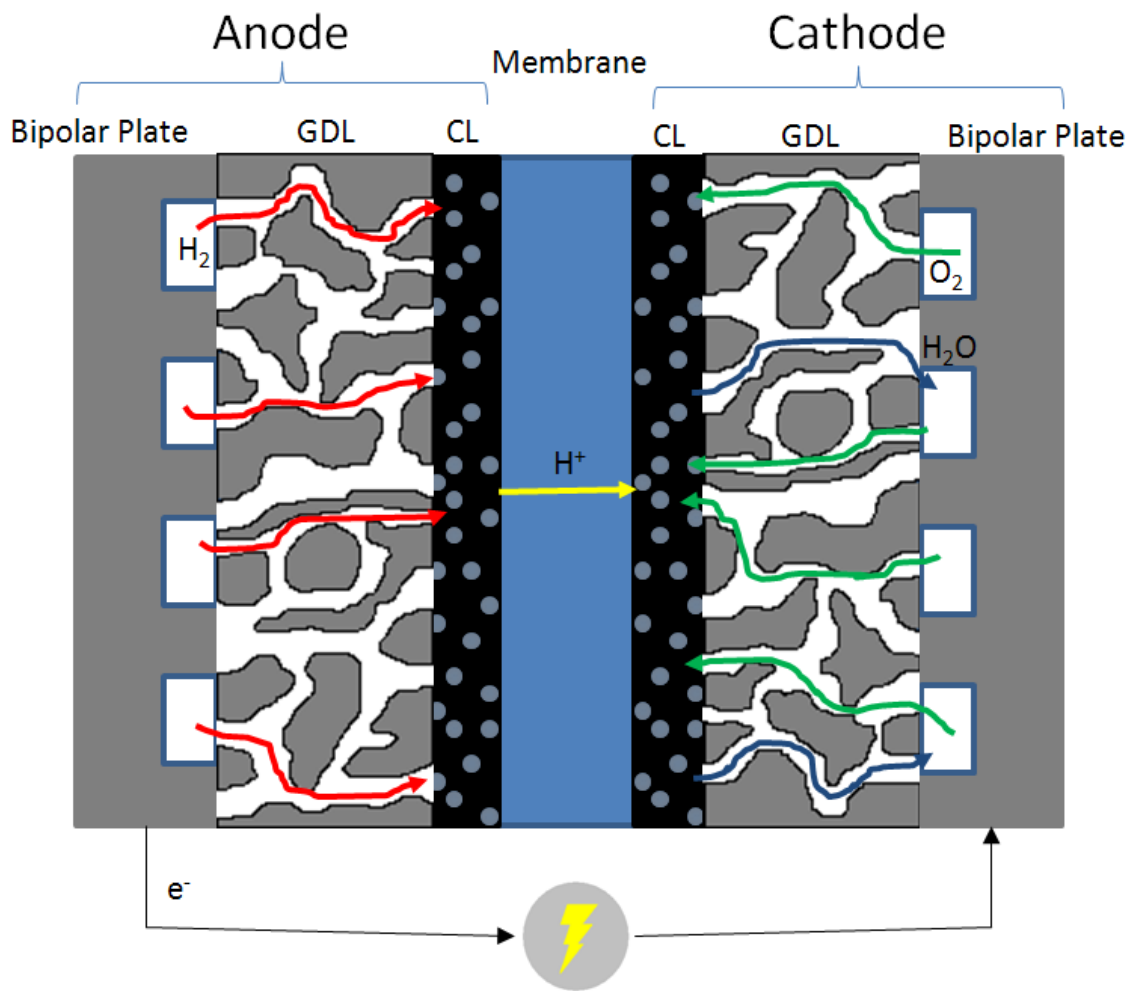
Figure 1-1: Schematic of a polymer electrolyte fuel cell

ionically conductive. This material must be properly hydrated to conduct protons across it as water provides the pathways for the protons to transport between sulfonic acid groups [4, 5]. Proper membrane hydration to ensure proton conductivity highlights the need for proper water management within PEFCs.

1.2.3 PEFC Catalyst Layer

The catalyst layer facilitates the hydrogen oxidation reaction and the oxygen reduction reaction and is located on both sides of the membrane. To facilitate the reaction, platinum nanoparticles are dispersed throughout a carbon particle support structure. This structure produces a porous material that allows for gaseous transport of reactants to the catalyst cites and removal of product water. This region must be both electronically and ionically conductive to bridge the gap between the membrane and the diffusion media to allow electrons and protons to conduct their respective directions. To facilitate this, ionomer is present in the catalyst. Platinum loading of the catalyst layer typically range from 0.05-0.4 mg Pt cm^{-2} on the anode and 0.1-0.4 mg Pt cm^{-2} on the cathode. The anode tends to have lower loadings than the cathode due to the diffusion speed and facile kinetics of hydrogen.

1.2.4 PEFC Diffusion Media

The diffusion media typically consists of a single layer (macro-porous) or double layer (macro/micro-porous) material that is located between the catalyst layers and the flow fields. This layer has five tasks that is must perform:

1. Thermal transport – the DM must be able to conduct the heat of reaction from the cathode catalyst layer to the flow field where coolant channels are typically embedded. Thermal conductivity of the DM can be tailored to influence water management, i.e. low thermal conductivity produces a high (3-5°C) gradient from catalyst layer to channel which maintains a temperature higher than condensation at the catalyst allowing for water vapor transport that does not hinder reactant transport [6].

2. Gas phase transport – the DM provides a transition zone between the gas channels in the flow field and the catalyst layer to allow even distribution of reactants at the catalyst sites. Without the DM, the catalyst sites located above the land areas of the flow field would be starved of reactants which would lead to poorer performance and degradation of the fuel cell as shown in Figure 1-2.
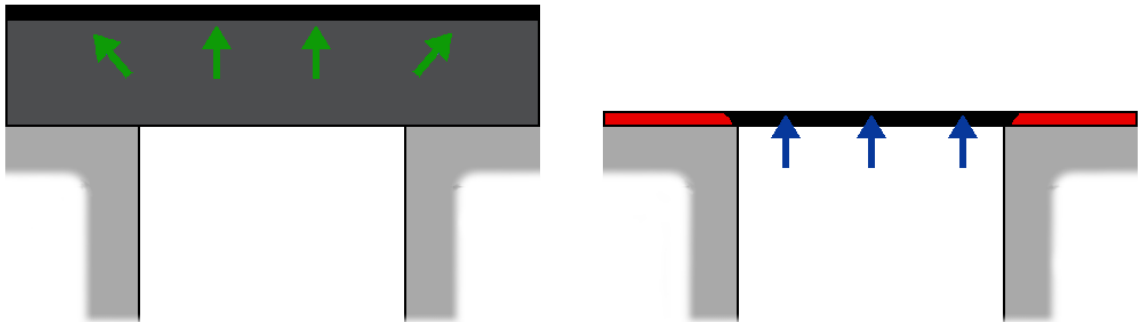
Figure 1-2: Channel-land interaction with catalyst layer. Left: The GDL provides a 2-D diffusion path for reactants to reach all areas of the CL: Right: Without the GDL, reactants are unable to reach catalyst sites located above the lands creating reaction dead zones (red) that can lead to degradation and poor performance.

3. Liquid phase transport – the DM must provide a path for product water to transport from the catalyst layer to the gas channels for removal without significantly reducing gas phase diffusion for reactants. Often, PTFE is added to increase the hydrophobicity of the material to improve water removal.

4. Electronic transport – the DM must provide a low resistance path for the electrons to travel from the anode to the cathode to provide the highest potential possible to the external circuit. [ref: electrical conductivity and performance]

5. Mechanical support – the DM must provide mechanical support to the catalyst layers and membrane to avoid shearing from the edges of the gas channels. Any holes in the membrane would cause gas cross-over and performance degradation.

Macro-porous layers, also called gas diffusion layers, are typically constructed of graphite fibers in either a paper like layup or cloth like layup. These fibers use a polyacrylonitrile precursor that is graphitized at temperatures greater than 1600°C. Examples of paper and cloth DM are shown in Figure 1-3. This produces a porous structure with a pore distribution of 10-30 µm [7].

Micro-porous layers (MPL) are coatings applied to the macro-porous layer to improve electrical contact with the catalyst layer and to improve water transport characteristics of the cell. The MPL is typically made from an emulsion of carbon black, PTFE, and solvent. This mixture creates a layer with an average pore diameter of 0.1 to 0.5 µm. The small pore size restricts the flow of liquid water causing a higher back diffusion rate to maintain membrane hydration [8-11].
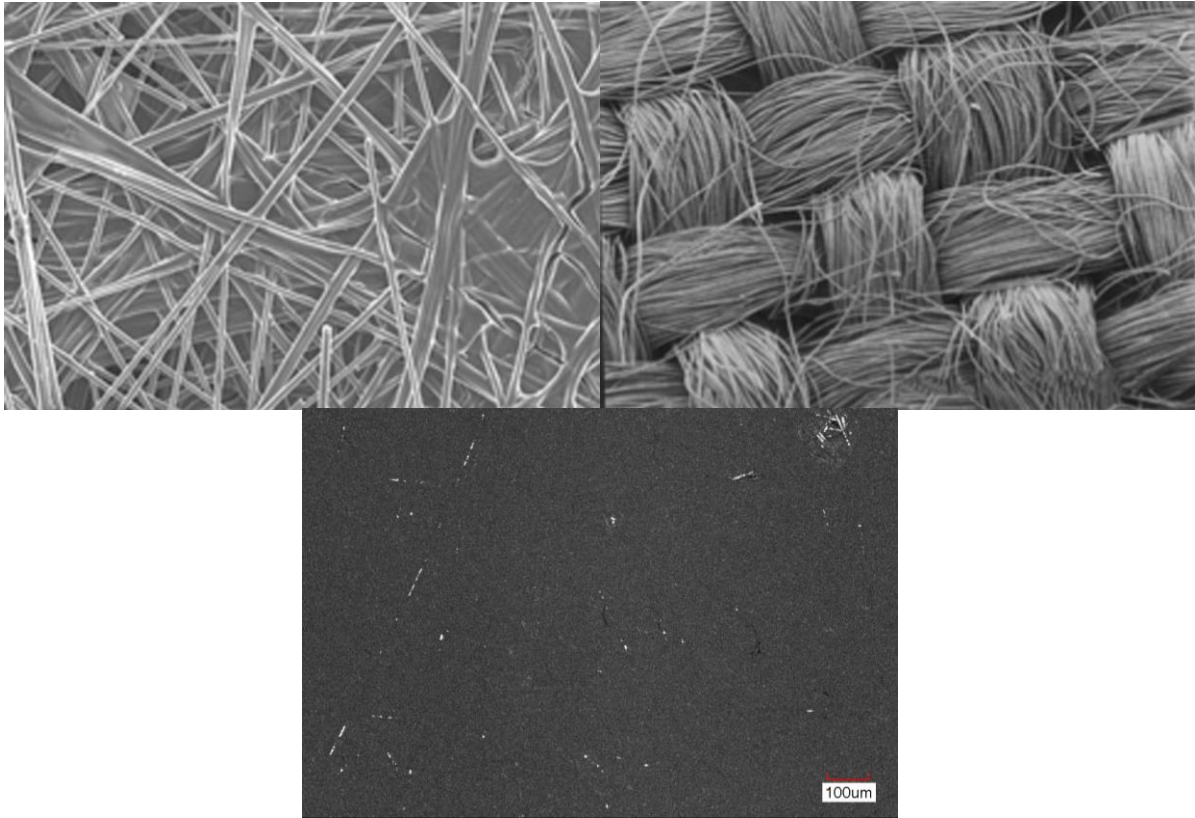
Figure 1-3: SEM images of paper type DM (top left), cloth type DM (top right), and MPL coating.

1.2.5 PEFC Flow Field

The flow field consists of channels that distribute the reactants and remove product water. Channel cross-sections can very across several shapes such as square, rectangular, semi-circular, triangular, or some variation thereof. The shape of the channel can have significant influence on liquid water removal dynamics, such as small angles wicking water to prevent slug formation [12, 13]. Flow patterns typically seen in PEFCs are serpentine, parallel serpentine, parallel, and interdigitated (examples shown in Figure 1-4). These patterns can be optimized to increase convective flow through the DM to improve reactant concentration at the catalyst layer or to force water out of the DM such as the interdigitated pattern [14-16]. In this flow pattern, the outlet channels are not connected to the inlet channels causing all flow to travel through the DM.

1.2.6 PEFC Electrochemical Equation

A stated earlier, PEFCs operate by oxidizing hydrogen on the anode and reducing oxygen on the cathode to produce electricity, water, and heat. Hydrogen enters the anode and diffuses to the anode catalyst layer where it is oxidized on a platinum site. This oxidation splits the H_2 molecule into its constituent parts, i.e., protons (H^+) and electrons (e^-), as shown in equation (1.1). As described previously, the protons are able to transport through the membrane to the cathode catalyst layer whereas the electrons must conduct through the external circuit. Once at the cathode catalyst layer, the protons and electrons combine with oxygen in a reduction reaction on a platinum site. This reaction requires four protons and four electrons for each O_2 molecule that reacts

Figure 1-4: Typical flow patterns seen in PEFCs. Top: Serpentine (left), Parallel (right). Bottom: Parallel Serpentine (left), Interdigitated (right).

to form two molecules of water as shown in equation (1.2). The overall cell reaction is given in equation (1.3).

Anode: $H_2 \leftrightarrow 2H^+ + 2e^-$ (1.1)

Cathode: $O_2 + 4H^+ + 4e^- \leftrightarrow 2H_2O$ (1.2)

Overall: $2H_2 + O_2 \leftrightarrow 2H_2O$ (1.3)

1.3 Channel-Land Geometry and DM Tortuosity Effects on Water Management

1.3.1 Significance of DM Liquid Water Saturation

Water plays a significant role in the performance of a PEFC and must be properly balance to maintain appropriate operation. A lower bound of water must be maintained in the cell to ensure proper membrane hydration and proton conductivity while the upper bound on water is limited by the ability of the reactant gases to reach the catalyst layers. Large quantities of water in the cell can lead to several modes of degradation such as fuel starvation and freeze-thaw damage. Since the gas channels and the DM are the primary routes for liquid water storage and removal in the cell, they will be the primary interest in the follow literature survey.

1.3.2 Literature Survey

In PEFCs, the gas channels and the DM are two important components for engineering better performance as they have significant influence on the water balance

and reactant distributions in the cell. Beyond optimizing the specific flow pattern, i.e. serpentine versus parallel as mentioned previously, it is possible to optimize the channel and land (space between channels) widths [17-22]. Excessively wide channels (>1 mm) can cause problems with additional stress on the MEA due to bending in the DM and can increase cell resistance if land widths are too small [17]. At the opposite extreme, excessively small channels increase pressure drop through the cell and increase unwanted system parasitic losses. Channel cross-sectional shape can have significant influences on water removal properties of the cell. Triangular channels have been shown to increase wicking of water from the DM and tend to keep water from forming solid slugs that block reactant flow [21]. Land width plays an important role in cell performance as it controls the reactant distribution and cell resistance. Large lands increase the diffusion length that reactants and product water must travel through the DM to reach the catalyst and channels, respectively. But if land width is reduced too much and channel width remains large, cell resistance will increase due to lack of contact area between the DM and flow field.

The influence of the channels on cell performance is directly coupled with properties of the DM such as permeability, diffusion coefficient, tortuosity, wet-proofing treatment, and engineering modifications like laser cut holes. These properties tie directly with channel-land design as permeability and diffusion coefficient influence the rate at which reactants and product water can move through the DM. It would be undesirable to use wide land widths with DM with low oxygen diffusion coefficients as this would result in concentration limitations on reaction rates for the catalyst sites in the center of the land

area. The determination of these properties has been critical to the understanding of the operation of a PEFC.

The diffusion coefficient of the DM can be measured with multiple methods that include ex-situ techniques [23-28] and in-situ techniques [29-32]. These methods give important information on the rate at which reactants such as oxygen travel through the porous material and the tortuosity of the material. Tortuosity is a measurement of the path length a given particle must travel to reach the opposite side of the material. The ex-situ techniques allow for the direct measurement of the diffusion coefficient for the material whereas the limiting current in-situ method it is not possible to completely decouple all of the layers and non-Fickian effects. The electrochemical diffusimetry method [23, 24] can measure both the in-plane and through-plane diffusion coefficients for the DM as these values can be significantly different due to the fiber orientation of the DM.

As stated in Section 1.2.5, channel geometry can be designed to increase convective flow through the DM. The ability of the flowing gas to jump through the DM from one channel to the next is primarily controlled by the land width between channels and the permeability of the DM. Measurement of the permeability of the DM has been conducted extensively in the literature [11, 33-37]. Due to the anisotropic nature of the DM, it is necessary to measure both the in-plane and through-plane permeabilities of the material. In-plane permeability is strongly influence by compression as the porosity decreases as compression increases. Gostick et al. [35] found that in-plane permeability ranged from approximately 8×10^{-11} m^2 to 1×10^{-12} m^2 depending on brand and compression pressure. These values can be upwards of an order of magnitude higher

than the values seen for the through-plane direction. Permeability and diffusivity of the DM can be influenced by the fiber diameter and manufacturing process. These parameters can be engineered to optimize transport properties of the DM [7, 38].

To improve the ability of the DM to discharge water, PTFE is often added as a wet-proofing agent to the material. This is typically accomplished by creating a solution of PTFE particles in solvent which the DM is dipped into. The PTFE is affixed to the DM by a sintering process. The quantity of PTFE must be balanced as high levels of PTFE increase water removal at the cost of porosity and thus the ability of the DM to transport reactants [39-41]. In addition to adding PTFE it is possible to modify the DM to increase water removal. Examples of modification include large diameter, i.e. 100-300 µm diameter, cut through the thickness of the DM with lasers. This allows preferential channels for water removal allowing gas phase transport in the non-perforated regions [42-44].

Water buildup in the DM and gas channels leads to performance loss and is a significant area of research [45-49]. Excessive buildup of water during flooding conditions cause issues such as voltage instability at constant current operation, voltage reversal during fuel starvation, cell startup and shutdown parasitic losses, and freeze damage if not properly purged. Therefore, it is critical to determine where water accumulates within the cell which requires special diagnostic tools.

Through-plane neutron imaging has developed into an important tool for fuel cell diagnostics over the past six years. The advent of high resolution detectors has made it possible to determine through-plane water saturation profiles in state-of-the-art diffusion media materials. Neutron imaging has several advantages over other imaging

techniques such as x-ray imaging [42, 50, 51], nuclear magnetic resonance (NMR) imaging [52, 53], or optical imaging [39, 54]. The primary advantage of neutron radiography is that it allows for the use of standard fuel cell materials with no substantial change in fuel cell design. This allows for proper thermal boundary conditions to exist in the cell for realistic single-cell water saturation profiles.

Hussey et al. [55] demonstrated one of the first through-plane images of a PEFC in 2007 with a 25 µm microchannel detector. The detector allowed the authors enough resolution to resolve changes in water content through the diffusion medium (DM). Actual data analysis was complicated due to the swelling of the Nafion 117 membrane that shifted the boundaries of the imaging area. Since then, multiple papers have discussed improvements to resolution for neutron imaging, e.g. [56-63], with best-case detector based resolutions approximating 10 µm.

Hickner et al. [64] developed a narrow active area single serpentine flow field fuel cell for through-plane imaging. It was found that water content remained relatively constant in the membrane, except at elevated temperatures and current densities, also measured by Spernjak et al. [65]. A condensation zone was observed within the DM. Water thickness results obtained from the cell were used to validate a model developed by Weber [66]. Condensation within the DM along thermal gradients was predicted by the model, and validated by the neutron radiography. This phenomenon is called phase-change-induced (PCI) flow and was further investigated by Kim and Mench [67] and Hatzell et al. [68]. Kim and Mench determined PCI flow to be a dominant driving force in hydrophobic catalyst layers and DM with water vapor transport from the hot to the cold regions. At a critical saturation, determined for the given fuel cell architecture by Hatzell

et al. to be approximately 30% for the given cell configuration, liquid water became connected enough in the DM to achieve funicular regime and enable rapid capillary action. The microporous layer (MPL) was found to block liquid water transport and provided a barrier to capillary water transport to and from the catalyst layer. Fu et al. [69, 70] developed an ex situ test to determine thermal gradient induced transport of liquid water across a cell. By precisely controlling the inlet humidity levels and the thermal gradient across the cell, water was found to transport from the warm side to the cold side. Neutron radiography data showed good agreement with water balance measurements.

Neutron radiography has been used to determine location and phase of water during sub-freezing start-up. Mishler et al. [71] operated a cell at 80°C which was shut down and purged before being cooled to -30°C. The cell was then restarted at constant current density of 0.04 A/cm^2 while being observed with neutron imaging. Ice formation was found to occur predominately in the cathode DM. Oberholzer et al. [72] determined that super-cooled water existed in the CL, DM, and channels during sub-freezing startup. Once enough super-cooled water accumulated within the MEA, a rapid freezing process would occur that caused voltage failure of the cell. This conclusion was supported by work from Chacko et al. [73].

Manahan et al. [43] and Manahan and Mench [44] used neutron radiography to determine water location in laser perforated DM. Diffusion media were perforated through both the macro- and microporous layers in grid patterns using several types of lasers to produce 100 and 300 μm holes. The perforated DM showed increased performance over unmodified DM at current densities above 1.4 A.cm^2 due to water

pooling in the perforations. Lasers that caused heat affected zones around the perforations in which PTFE was removed helped to wick water into the perforation due to the increase in hydrophilicity. Mukundan et al. [74] investigated modifying the MPL by addition of hydrophilic fibers to increase cell performance. It was found that the hydrophilic fibers in the MPL helped wick away water from the cathode catalyst layer thus improving oxygen diffusion and high current density operation.

The impact of channel-land variation on DM water content has been studied by several groups. Turhan et al. [75] studied the effects of channel hydrophobicity on cell water content with a single serpentine channel cell. It was found that hydrophobicity directly impacts water removal from the DM in areas above the lands. Hydrophilic channels pull water out of the DM above the lands whereas hydrophobic channels impede this draining action. The hydrophobicity of the channels was not found to significantly influence water transport by PCI flow in the DM. Cho and Mench [18] studied evaporative water removal from PEFCs during shutdown. Neutron radiography was used to validate a composite purge cycle of cell water content for a single serpentine flow field. The composite purge cycle was found to remove water with reduced parasitic loss. Channel-land geometry for straight, parallel channels was investigated by Tabuchi et al. [76] with neutron radiography. Increased channel and land width was found to reduce cell performance and increase the non-uniformity of liquid water saturation levels within the DM. Channel land variation was also studied by Oberholzer et al. [20] with specially developed "0D" interdigitated, "1D" narrow land width parallel, and "2D" wide land width parallel flow fields that controlled the direction of diffusional transport. Two-dimensional diffusion was found to cause bulk diffusion

limitations in the operation of the cell. Radiographs showed accumulations of liquid water over the large land areas in the "2D" case, which were nonexistent in the other two cases.

1.3.3 Motivation

The above literature survey and component descriptions have shown the importance of cell water content on performance and durability. Diffusion media and gas channel properties play a significant role in determining the liquid water content of the cell. These two components represent materials that can be engineered to influence their transport properties and thus the water content of the cell. This work will use high resolution neutron imaging to determine how channel shape, width, and pitch and DM tortuosity can be optimized to provide ideal water balance for high performance and reduced degradation.

CHAPTER 2:   Method of Approach

In this study, through-plane high resolution neutron imaging and real-time water balance measurements were used to determine gradient influence on liquid water accumulation in an operating PEFC. The high-resolution neutron imaging was conducted at the National Institute of Standards and Technology (NIST) Center for Neutron Research in Gaithersburg, Maryland.

2.1 High Resolution Neutron Radiography

Neutron radiography (NR), also referred to as neutron imaging, is an imaging technique that passes neutrons through the material of interest to determine internal structures and points of interest. This technique relies on the scattering and absorption cross-sections of the elements of the material being imaged to produce contrast. Figure 2-1 compares the x-ray and neutron cross-sections of typical fuel cell materials. As can be seen in from the figure, neutron imaging offers the advantage over x-ray imaging due to the high contrast between hydrogen and carbon. Since carbon and aluminum have relatively small neutron cross-sections, typical fuel cell materials can be used to construct NR compatible cells. This minimizes any potential changes to thermal, electrical, and wetting property boundary conditions to the cell resulting in realistic water content. Other imaging techniques used in fuel cells typically require significant modifications to the cells to make them compatible with the technique. X-ray imaging requires non-metallic parts as X-ray attenuation increases with atomic mass [77-83]. Nuclear magnetic resonance imaging requires non-metallic and non-magnetic parts [52,
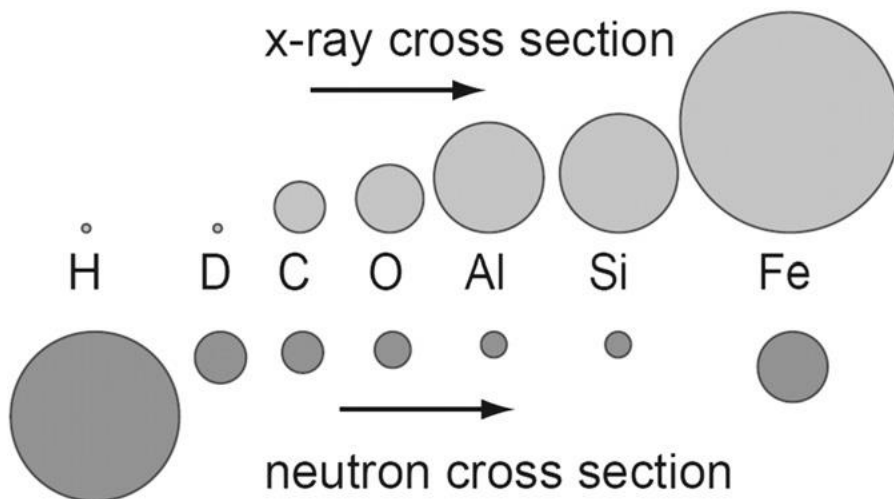
Figure 2-1: X-ray vs neutron cross-section for typical fuel cell material, from Tsushima [84].

53] and visible and infrared optical imaging requires transparent (with respect to wavelength of light used) windows to be placed in the cell [13, 39, 54].

Imaging of water in the DM with neutrons first started with Satija et al. [85] whereas earlier work focused on membrane water content [86, 87]. Satija et al. demonstrated initial imaging with the newly developed beamline at NIST. Most initial fuel cell NR work was limited to imaging the in-plane direction due to limitations in detector resolution. In-plane imaging does not allow for the uncoupling of anode and cathode water as the image is the integration of the two halves but allows for the imaging of channel interaction with the DM [14, 21, 88-91]. High-resolution through-plane imaging of fuel cells began when detector resolutions achieve ~25 μm in the mid-2000's [55, 64].

The Neutron Imaging Facility at NIST has been developed to facilitate high resolution studies of fuel cells. Figure 2-2 shows the overhead schematic of the imaging facility with associated neutron beam conditioning equipment and fuel cell testing
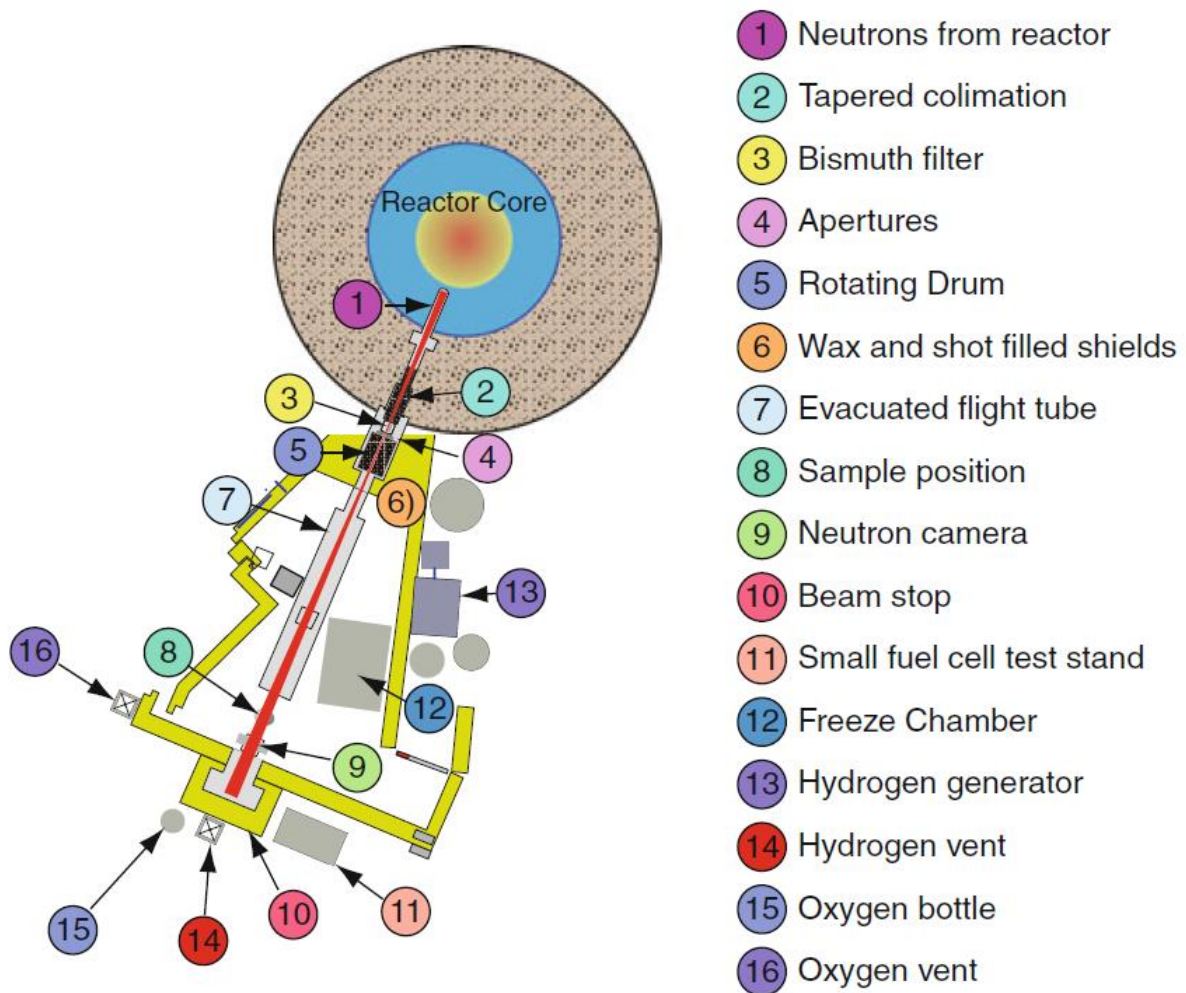
Figure 2-2: Schematic overview of Neutron Imaging Facility at NIST (adapted from Hussey [92])

hardware. The fuel cell testing equipment allows for operating cells with 0-100% H2, 0-100% oxygen, -40 to 100°C, 0-100% relative humidity, and elevated exhaust pressures.

The neutron imaging system at NIST is based around pinhole optics where the beam passes through a small hole to collimate it, i.e. the aperture in Figure 2-2. The diameter of this hole, in addition to the distance from the aperture to the detector, forms one of the two primary figures of merit for neutron imaging facilities, the L/D ratio and the neutron fluence rate. The sample to detector distance and the L/D ratio determines the geometric blur which describes the minimum spatial resolution for a beamline given that the detector is capable of a similar resolution. Geometric blur is calculated using Equation (2.1) [92].

$$\lambda_g = zD/(L-z) \approx zD/L \qquad\qquad (2.1)$$

Where λ_g is the geometric blur, z represents the sample to detector distance, D is the aperture diameter, and L is the aperture to detector distance as shown in Figure 2-3. This geometric blur can be reduced by using small D values to obtain high L/D values, minimizing the z distance, and reducing the thickness of the object being imaged. For this study, the aperture used was a slit with dimensions of 10 mm x 1 mm which gives an L/D ratio of 6000 in the x (through-plane) direction and 600 in the y (in-plane) direction. The fuel cell was placed within ~2 cm of the detector. This gives a value of 3 µm for λ_g which is 5 times smaller than the detector resolution. The fluence rate for the aperture used was 6.54 x 10^5 cm^{-2}s^{-1}. Design considerations for the cell must be taken to ensure that the geometric blur can remain low. Therefore, the cell must be designed
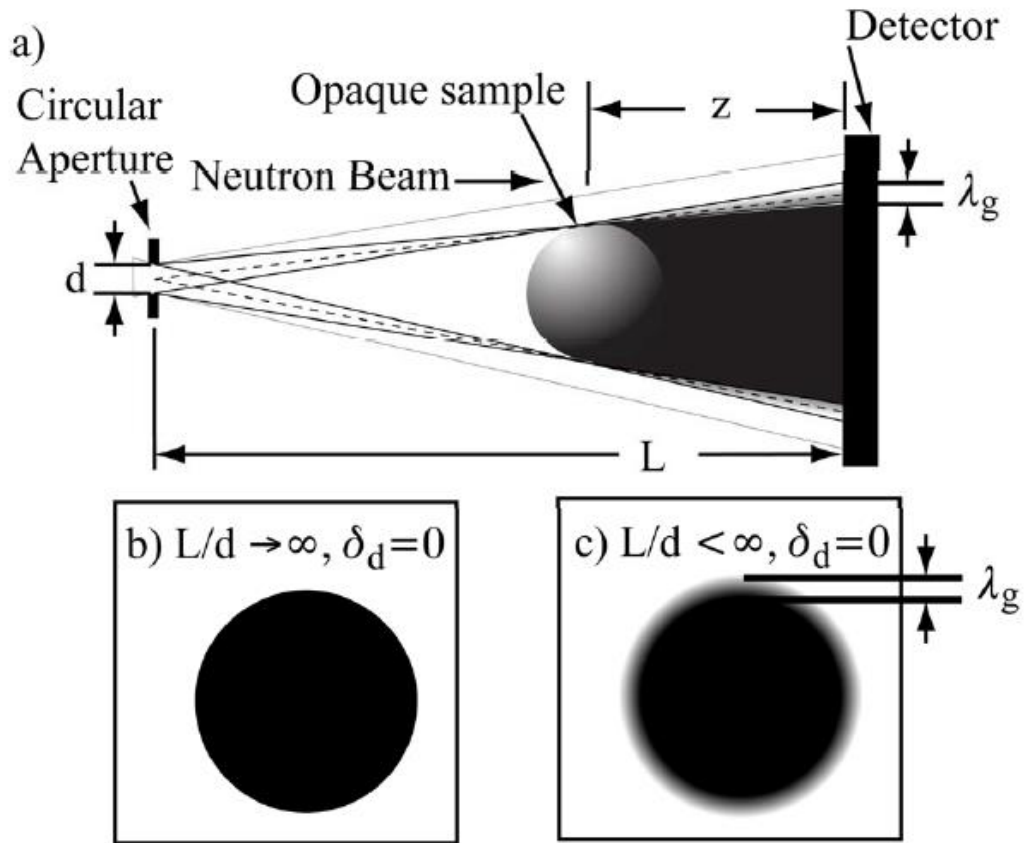
Figure 2-3: Geometric unsharpness due to the point spread function of the pinhole optic system (adapted from [93]).

to allow the active area to be as close to the detector as possible and to have a narrow active area so that the edge furthest from the detector is reduced.

To achieve the highest image resolution possible at NIST, a microchannel plate (MCP) detector was used. This detector is able to achieve a 15 μm resolution. The operating principle of this detector is to convert the neutrons to electrons for detection. A glass plate doped with gadolinium or ^{10}boron captures neutrons and release high energy, charged particles. The charged particles enter the 6 to 12 μm channels in the plate causing electrons to be stripped from the surface. These electrons are then accelerated towards the two-dimensional resistive array. As the electrons move along the channels due to the high voltage field present, amplification occurs that increases the amount of electrons by a factor of 10^6 to 10^7. A schematic of the MCP detector is given in Figure 2-4.

Neutron detections are converted to water thickness through a calibration process for each detector. A calibration wedge is used that has a staircase pattern machined in it to vary the thickness of water. These wedges will typically start at 0 mm water thickness and increase to 5 mm water thickness in known steps. The attenuation coefficient can be calculated from the images taken with the wedge allowing for conversion from neutron count to water thickness as shown in Figure 2-5.

Before the cell is imaged it is necessary to align it with the beam so that the materials are edge on in respect to the beam. This prevents shadowing and water content influences from layers behind or in front of the layer of interest. After alignment, dry images are taken with no water present in the cell. These images will be used to remove the structure of the cell from the wet images leaving only water present. Other
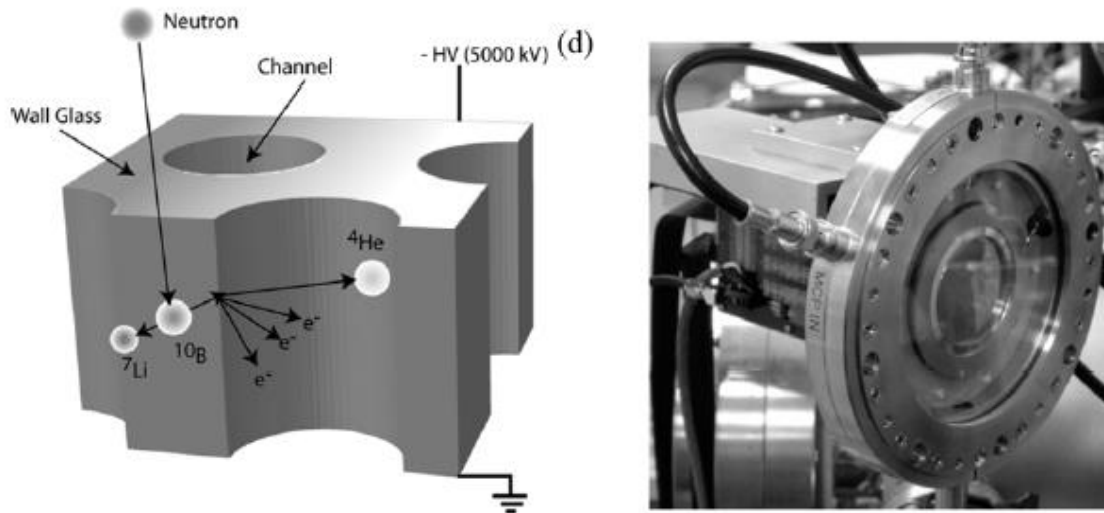
Figure 2-4: NIST MCP detector operates by detecting neutrons by conversion to electrons (adapted from Hussey [93]).

additional corrective images are necessary to remove error induced by unwanted gamma rays and inherent detector structure. Additional information on this process will be given in Chapter 3.

2.2 Real-Time Water Balance Measurements

Real-time data on cell water balance is obtained using high accuracy, high temperature dew point temperature transmitters produced by Vaisala. These HMT337 sensors measure the dew point temperatures of the anode and cathode gas inlets and outlets as shown in Figure 2-6. The HMT337 allows for high humidity and high temperature measurements, as typically seen in fuel cell operation, with accuracy of ±0.6°C. A National Instruments USB-9174 four module chassis with NI-9207 8 channel current module are used to collect the 4-20 mA signal from the HMT337. Labview is
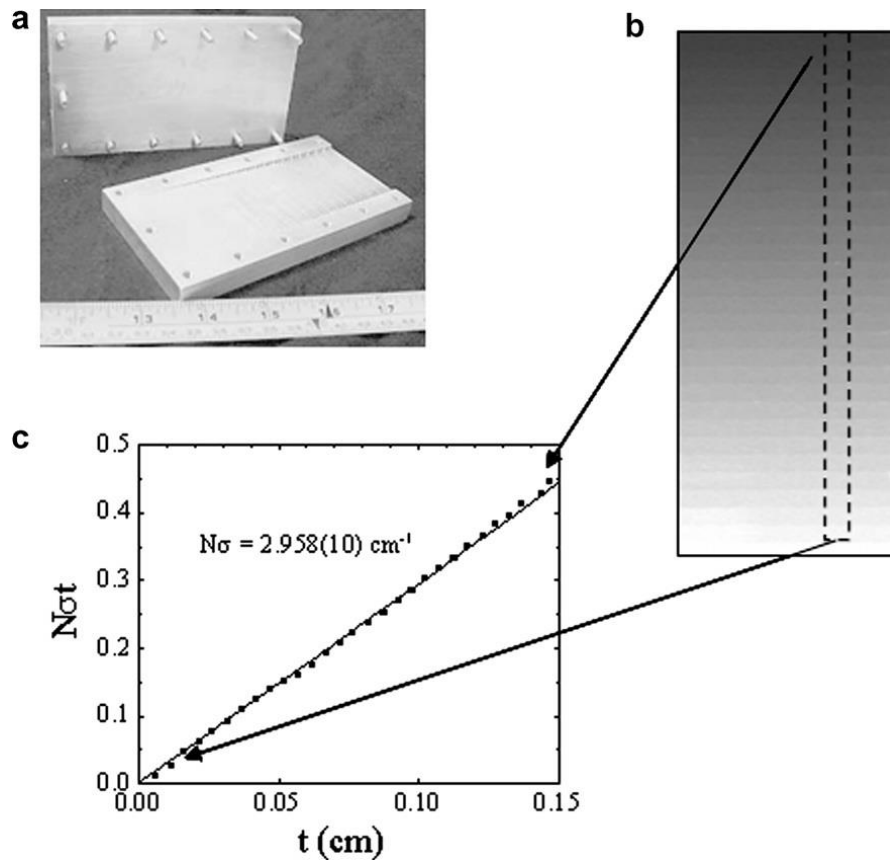
Figure 2-5: Calibration wedge used to convert neutron count to water thickness (adapted from Owejan [14])

used to view and collect the data during acquisition. This system has been shown to produce repeatable data for several sizes of fuel cells [94-96].

The dew point temperatures collected with the electronic system are then used to calculate the net water drag (NWD) which is defined as the net amount of water molecules transferred across the membrane per proton transferred as defined by equation 2.2. A positive NWD implies a net flux of water from the anode to the cathode which implies that electro-osmotic drag is dominant. Whereas, a negative NWD describes a net water transport from the cathode to the anode implying that back diffusion, temperature or pressure gradients, or a combination thereof has become dominant.
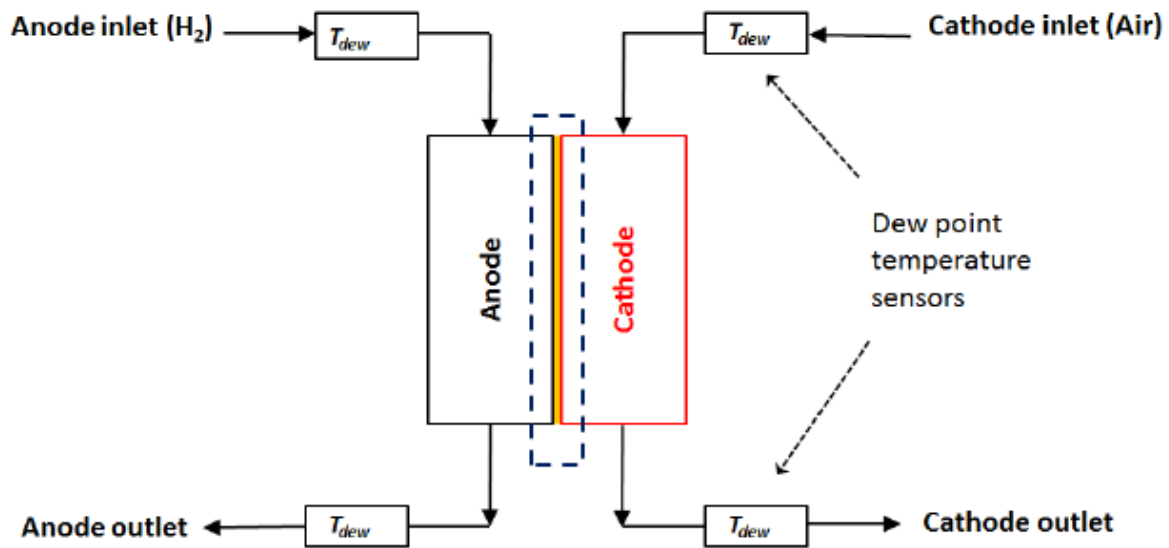
Figure 2-6: Schematic of real-time water balance measurements using dew point temperature sensors (adapted from Ashraf Gandomi [94])

$$C_{NWD} = \dfrac{\dot{n}_{H_2O}^{in,an} - \dot{n}_{H_2O}^{out,an}}{\dfrac{iA}{F}} \tag{2.2}$$

The values of the moles of water entering and exiting the cell in equation 2.2 can be calculated from the dew point temperature sensors with equation 2.3 for the inlet and 2.4 for the outlet. All four sensors are used to ensure mass balance and that steady state has been reached.

$$\dot{n}_{H_2O}^{in,an} = \lambda_{H_2} \dfrac{iA}{2F} \dfrac{P_{sat(Tdew_{an,in})}}{(P - P_{sat(Tdew_{an,in})})} \tag{2.3}$$

$$\dot{n}_{H_2O}^{out,an} = (\lambda_{H_2} - 1) \dfrac{iA}{2F} \dfrac{P_{sat(Tdew_{an,out})}}{(P - P_{sat(Tdew_{an,out})})} \tag{2.4}$$

CHAPTER 3:   Baseline Results

This chapter is revised based on the published paper [97]:

J.M. LaManna, S. Chakraborty, J.J. Gagliardo, M.M. Mench, "Isolation of transport mechanisms in PEFCs using high resolution neutron imaging", International Journal of Hydrogen Energy, 39 (2014) 3387-3396.

My primary contributions to this paper include: 1) Design and development of experiment, 2) final data reduction and presentation, 3) analysis and interpretation of the experimental data and 4) writing of most of the manuscript.

3.1 Introduction

The work presented in this chapter is motivated by the need to further quantify the impacts of imposed gradients of relative humidity (RH), temperature, and pressure on water redistribution in an operating cell and to provide standardized, repeatable high precision data over a broad range of operating conditions with off-the-shelf components for the purpose of multi-phase model validation. Several papers have used neutron radiography to validate models [66, 76, 98, 99] but these datasets are not publically available. The data and analysis from this work can be used to provide detailed computational model validation through a publicly available internet database, www.pemfcdata.org [100]. The neutron imaging in this study was accomplished at the high-resolution neutron imaging facilities at the NIST Center for Neutron Research in Gaithersburg, MD. The channel geometry used in the fuel cell (described below) is designed to simulate full cell automotive fuel cell hardware and appropriately reflect

industrial conditions including generic manifold design and asymmetric channel architecture features. Operating conditions and channel architecture are sufficiently wide-ranging to provide conditions which stress the limits of multi-phase models in extreme conditions.

3.2 Method of Approach

3.2.1 Cell Design

A 4.8 cm^2 fuel cell was developed and used in this work. This fuel cell has a narrow active area of 9 mm by 53 mm to reduce neutron scattering and geometric unsharpness, and enable sufficient neutron flux for relatively rapid image acquisition. The flow field consists of triple serpentine channels with a square cross-section of 0.5 mm width machined into conductive BMCI 13905 graphite-polymer composite. Asymmetric land widths are utilized in this work based on a previous US Department of Energy supported project [101] with 0.5 mm cathode lands and 1.5 mm anode lands, as illustrated in Figure 3-1. The triple serpentine flow field pattern was used to facilitate cross-sectional imaging of the channels and lands.

To precisely control the thermal boundary conditions of the cell, coolant channels were placed directly adjacent to the current collector plates. Circulator baths with ±0.2°C precision were used to control the water temperature and flow rate through the coolant channels. The temperature of the coolant was verified as it enters the cell. Coolant flows
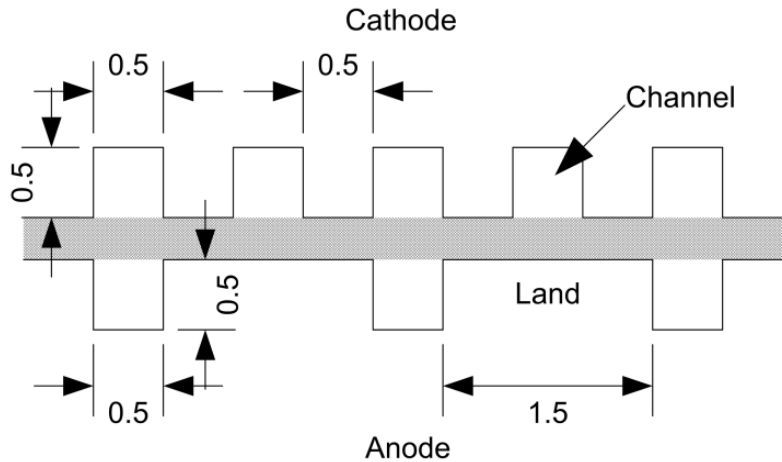
Figure 3-1: Channel dimensions for high-resolution neutron imaging cell. MEA represented by hashed area. All dimensions are in millimeters.

upward from bottom to the top of the cell, which was oriented vertically, to allow for removal of air pockets in the coolant channels. Gases enter the top of the cell and flow downwards with gravity to assist in the removal of liquid water slugs, as illustrated in Figure 3-2. The flow rate of the coolant was high enough to ensure uniform thermal boundary conditions along the entire flow field. Neutron radiographs are taken from approximately the center 2 cm of active area of the cell as outlined by hash marks in Figure 3-2.

The diffusion media (DM) used in this work was 230 μm thick Mitsubishi Rayon Corporation U105 with 6% PTFE by weight and 30 μm thick MPL coating. Gore Select Series 5720 18 μm membranes with 0.3 mg/cm^2 cathode loading and 0.05 mg/cm^2 anode loading were used. More detailed descriptions of the materials can be found on www.pemfcdata.org [100].
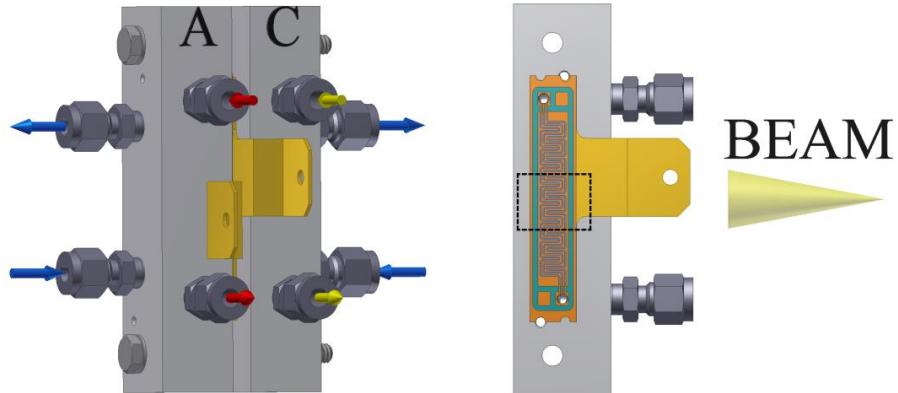
Figure 3-2: Schematic of cell orientation. Cell is oriented vertically and gas enters the cell at the top and exits at the bottom whereas coolant flows from the bottom to top to facilitate the removal of air when filling coolant. Approximate area imaged with neutrons shown with black hashed box.

3.2.2 Test Facility

Testing was conducting at the BT-2 Neutron Imaging Facility at the NIST Center for Neutron Research located in Gaithersburg, Maryland. The high-resolution detector used in this work was the microchannel plate (MCP) detector [55, 63]. The MCP detector allowed for the highest resolution imaging obtainable at NIST with an image resolution of approximately 15 μm and a 3 cm diameter field of view. Fuel cell testing equipment available at NIST allows for precision control of gas flow rates, current, voltage, gas temperature, gas humidity, and exhaust pressure.

3.2.3 Test Conditions

Test conditions were chosen to isolate individual gradients while providing datasets that stress the extremes of wet and dry operation for model validation. Recent model

validation has shown the critical importance of capturing dry out as well as flooding to verify the accuracy of multi-phase models, as only polarization-based predictions are often inadequate [102]. Conditions selected to be varied during testing include current density, boundary temperature, exhaust pressure, and inlet relative humidity. Values for each variable are given in Table 3-1. Constant flow rates across all conditions regardless of current density were selected with an equivalent stoichiometric ratio of 2:2 at 1.2 A/cm^2. This was done to ensure consistent convective boundary conditions existed between all test conditions. Not all current densities were achievable for the conditions shown due to issues such as flooding. Concentration gradients were not tested at 40°C due to the difficulty of providing accurate humidification at low temperature and flow rates. When the pressure gradient was varied, relative humidity was held constant at 95|95 (anode|cathode) %RH whereas when concentration gradient was varied, exhaust pressure was held constant at 150|150 (anode|cathode) kPa(a). Use of an asymmetric flow field architecture provides data on channel/land impact on retention, which has been shown to be important by various authors but is not normally included in models. The data discussed in this work is a subset of the complete dataset available for download at www.pemfcdata.org [100].

Table 3-1: Operating Parameters

Operating Parameters	Values [units]
Current Density	0.1, 0.4, 0.8, 1.2, 1.5 [A/cm^2]
Temperature	40, 60, 80 [°C]
Pressure Gradient anode|cathode	100|150, 150|150, 150|100 [kPa(a)]
Concentration Gradient anode|cathode	50|50, 95|50, 50|95, 95|95 [inlet %RH]

3.2.4 NR Data Reduction and Analysis

At each current density, the fuel cell was allowed to attain and maintain steady state for 30 minutes. A 13 µm pixel size microchannel plate (MCP) imaging system at NIST was utilized for these tests [103]. Images were collected with an exposure time of 5 minutes, which yielded 5 images for each test condition. A single compiled image was extracted by averaging these 5 images. The images were then corrected and normalized to remove noise caused by gamma and fast neutron radiation and to remove detector structure effects.

The resulting image was further normalized with respect to an invariant part of the image to compensate for small changes in neutron fluence during each test condition, and then a ratio of intensities for the wet and dry image was calculated. For the saturation profile plots, a ratio of the sum of intensities along the axis (Transmission ratio (Tr)) was calculated for each pixel location across the thickness of the DM and MEA.

The neutron transmission through water is non-trivial as the total scattering cross-section (σ_T) is neutron energy dependent. The cross-section (σ_T) in general increases with decreasing neutron energy. The result is that the optical density is non-linear in t_w, an effect known as beam hardening. Beam hardening for water is well-modeled [92, 104] by a quadratic function where the optical density as a function of water thickness is $OD(t_w) = \mu t_w + \beta t_w^2$

The water thickness is then obtained via

$$t_w = -\sqrt{\left(\frac{OD}{\beta}\right) + \left(\frac{\mu^2 \times 0.25}{\beta^2}\right)} - \left(\frac{\mu \times 0.5}{\beta}\right) \qquad (3.1)$$

Where [104]

$$\mu = (0.374 \pm 0.005)mm^{-1} \qquad (3.2)$$

$$\beta = (-0.0086 \pm 0.0004)mm^{-2} \qquad (3.2)$$

The saturation is calculated as $s = t_w/\phi d$, where the water thickness t_w is obtained from the above correlations, ϕ is the compressed porosity and d is the width of the active area. The compressed porosity of the DM was calculated to be 67.7%.

For the density images, the intensities were not summed in any direction, rather the transmission ratio was calculated for each pixel. The final images were filtered with a 6x6median filter, to de-noise the images.

3.3 Results and Discussion

3.3.1 Hydraulically Driven Flow

Cell exhaust pressure was manipulated to control hydraulically driven flow through the cell at all three temperatures. The 1.2 A/cm^2 and 1.5 A/cm^2 tests at 40°C and 60°C could not be completed for the 100|150 kPa cases due to poor cell performance. False color neutron images of the lower portion of the imaged area of the cell in Figure 3-3 for 0.8 A/cm^2 at all three temperatures show the decrease in overall

cell water content with increasing temperature. Liquid water was found to be driven to the low pressure side of the cell with the anode saturation changing significantly, while the cathode remained nearly the same at lower temperatures. Figure 3-4 shows liquid water saturation profiles across the thickness of the cell for RH conditions at 40 and 60°C averaged down the entire length of the neutron image. The large changes in anode saturation, as shown in Figure 3-4, can be attributed to the asymmetric flow field used in this study. Large anode land areas allow for greater water retention in the DM due to large low temperature regions and reduced channel/DM interfaces [75]. The ability to store larger quantities of water results in the anode DM achieving high levels of saturation, around 50%, as shown with the 1.5 A/cm^2 case in Figure 3-4. This high level of anode saturation is likely what kept the cell from reaching acceptable performance at higher current densities at 40 and 60°C, through reduced anode performance or shifted water balance toward the cathode. As a reference electrode was not used in testing, the electrode responsible for the performance loss was not verified. The presence of an internal saturation peak in the DM is a result of condensation within the DM.

The cathode invariance with changing pressure gradients is primarily attributed to the relatively larger channel surface area. The large area allows for efficient vapor phase removal. High velocity at the channel exits relative to the anode and greater water carrying capacity at sub-saturated conditions also aid in the removal of liquid water from the cell. The cathode lands are 1/3 the size of the anode lands and are not capable of as significant water buildup as the anode since there is less heat removal to drive condensation and any buildup of water would drain to the channels. This helps to highlight channel-land interaction as a critical parameter in DM water content and

36
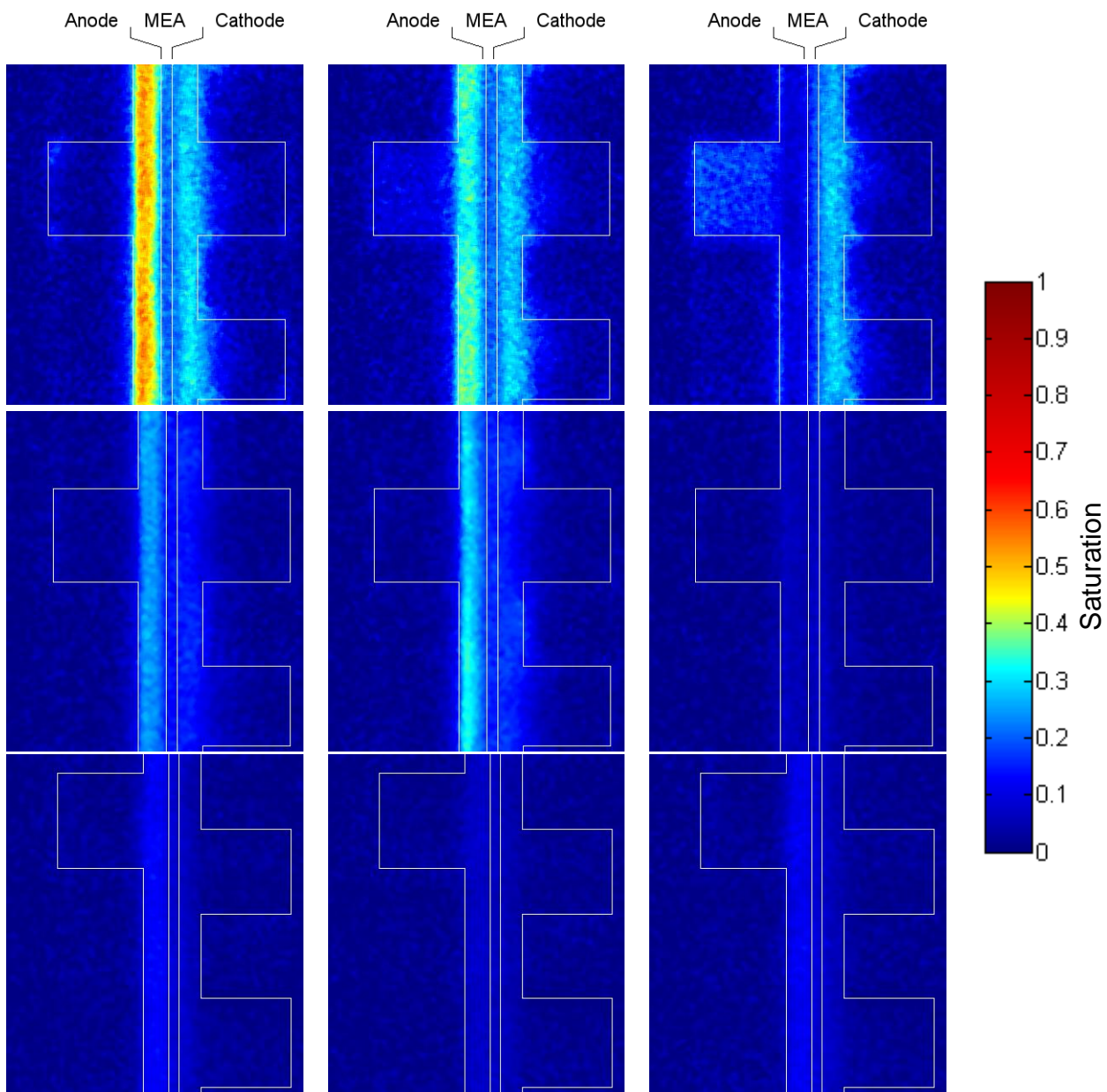
Figure 3-3: Radiographs showing influence of exhaust pressure gradients on cell water content at 40°C (Top), 60°C (middle), and 80°C (bottom). Anode|Cathode pressure: 100|150 kPa (left), 150|150 kPa (middle), 150|100 kPa (right). Test conditions: 0.8 A-cm^{-2}, 2/2 stoichiometry at 1.2 A-cm^{-2}.
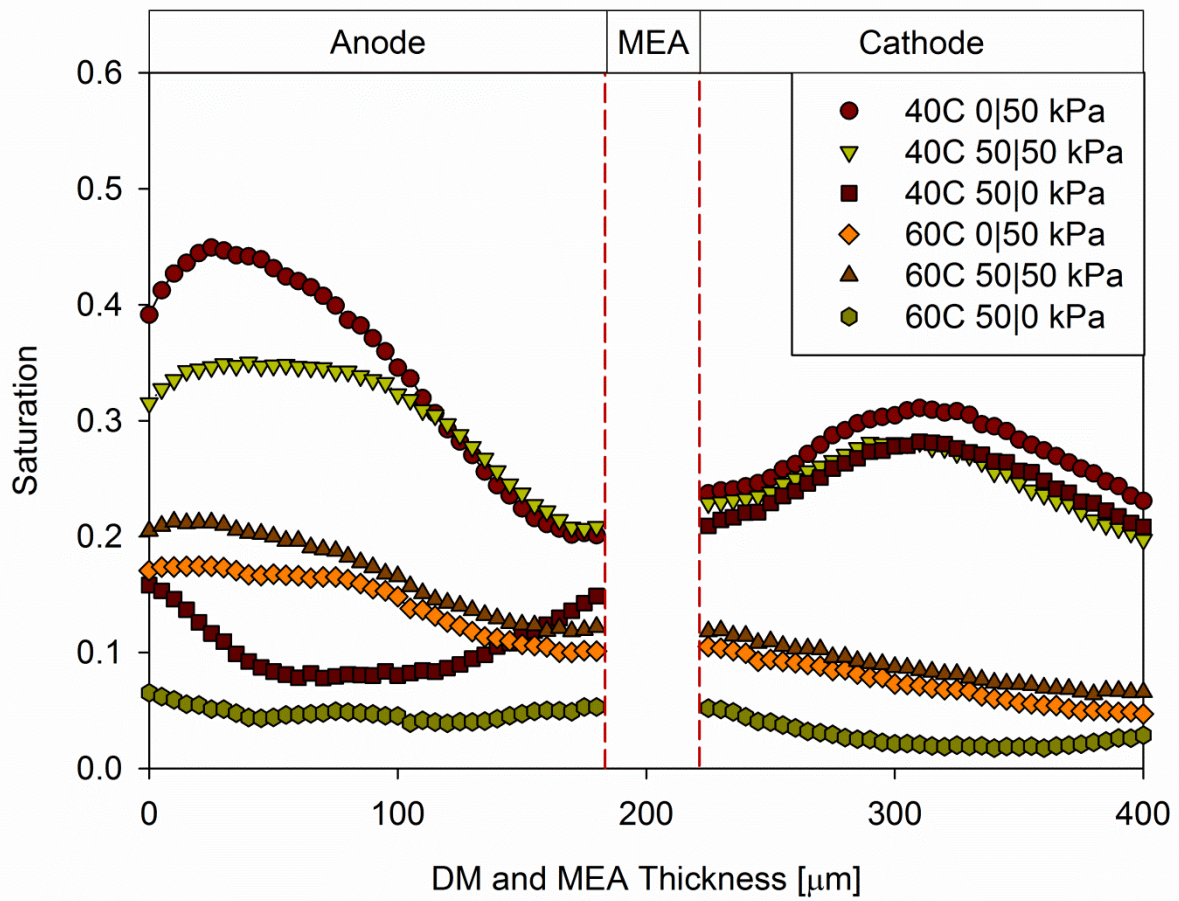
Figure 3-4: Saturation profiles for exhaust pressure variance (anode|cathode) at 40 and 60°C. Conditions: 0.8 A-cm^{-2}, 95% RH, 2:2 stoichiometry at 1.2 A-cm^{-2}.

agrees with Turhan et al. [88]; this is not often included in models of PEFCs.

Increasing the temperature to 80°C significantly reduced the liquid water within the cell at 0.8 A/cm^2. At this temperature all of the saturation profiles collapsed to the same approximate water content, within the error of the detector, as shown by the saturation profiles in Figure 3-5. As a majority of liquid water content was reduced, hydraulically driven flow was mostly eliminated, thus causing minimal differences between the saturation profiles. At the highest tested current density of 1.5 A/cm^2 where water generation is higher, however, saturation profiles exhibited similar trends as seen in the lower temperature cases. Hydraulically driven flow is shown to be primarily important in the lower temperature cases where liquid water is more prevalent. This condition is particularly important during startup and warm-up during early portions of drive cycles.

3.3.2 Diffusion driven flow

Relative humidity of the inlet gases to the fuel cell was varied to induce a water concentration gradient across the cell to drive water transport by diffusion. The anode was found to be very sensitive to this gradient much like the hydraulically driven flow case. Large anode land areas enable retention of liquid water in the diffusion media as shown in the false color neutron radiographs in Figure 3-6.

Anode sensitivity, i.e. fluctuations in saturation from test case to test case, is primarily attributed to the large lands and larger low temperature areas under lands but also due to the large amount of water that drops out of the diminishing anode flow which can be reduced up to 75% at higher current at the conditions tested. As seen in Figure
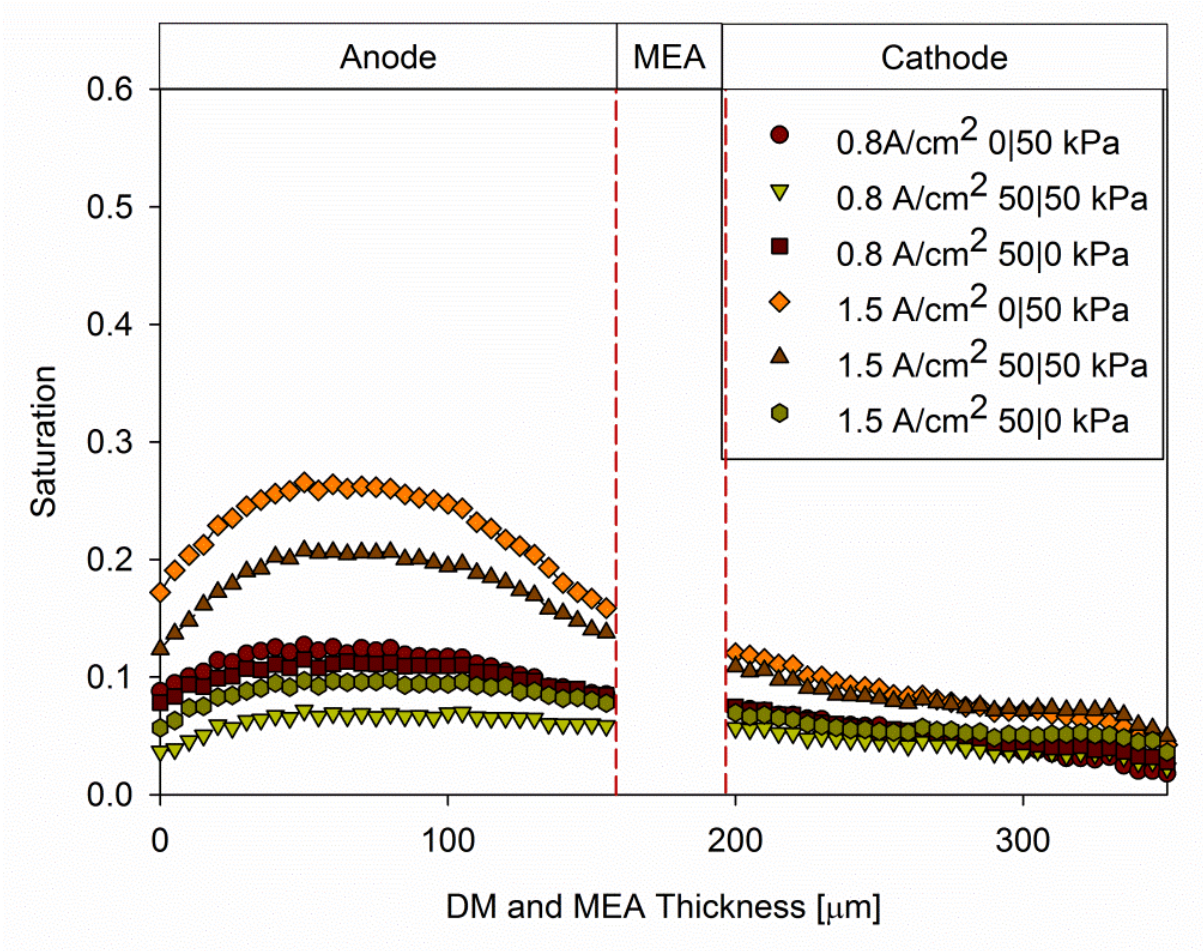
Figure 3-5: Saturation profiles for exhaust pressure variance (anode|cathode) at 80°C. Conditions: 0.8 A-cm^{-2}, 95% RH, 2:2 stoichiometry at 1.2 A-cm^{-2}.

3-6, overall cell water content is dominated by anode water content. The cathode DM reaches maximum saturation values of approximately 25% only when the anode has high water content and high inlet RH. The cathode maintains low saturation values even with 95% RH inlet gases when the anode has low inlet humidity. Clearly, the land area plays a determinant role in maximum water retention not captured in many multiphase models.

Similar trends for profiles of cell water content are seen when the temperature is increased from 60°C (Figure 3-7) to 80°C (Figure 3-8) but with a reduction in overall cell water content and anode concentration gradient sensitivity which indicates that the water capacity of the reactant stream is important, as expected. Anode water content is highest for the 95|95% case for both temperatures with a reduction in water content at 80°C seen for the 95|50% case compared to the same case at 60°C, as expected due to the higher saturation pressure at 80°C. Although performance was reduced at some concentration levels as shown by the polarization curves in Figure 3-10 and voltage data in Table A-1, the cell was able to operate at all selected current densities regardless of gradient direction or magnitude. This reduction in cell performance can be attributed partially to the increase in anode water content from 1.2 A/cm^2 to 1.5 A/cm^2 for the 95|95 %RH and 95|50 %RH cases shown by the liquid water profiles in Figure 3-9. Water content increases from approximately 35% to 50% indicating a point of critical water content that restricts hydrogen flow.

3.3.3 Inlet-to-outlet Water Content Variation

Saturation data from the entire image area of the cell produces large two-dimensional datasets that show channel-to-land variation as a function of gas stream

41
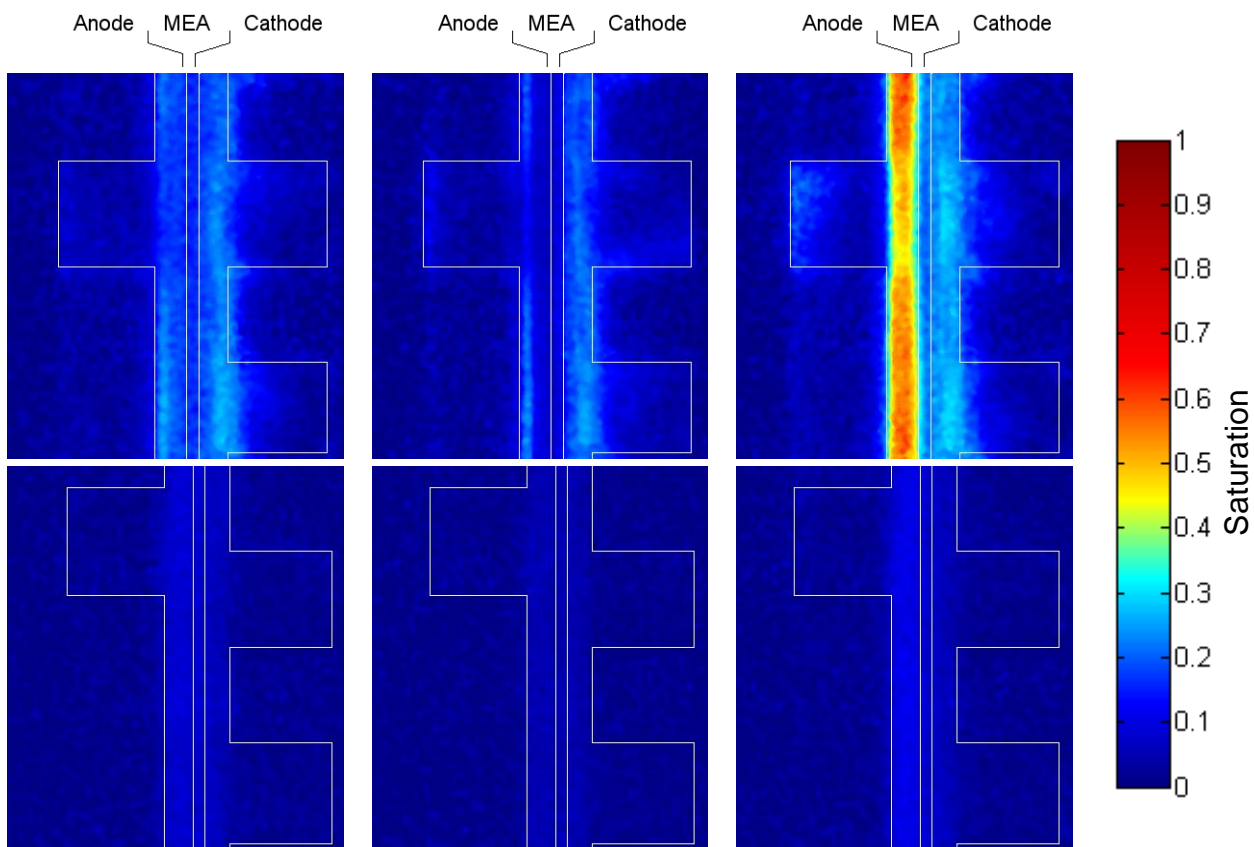
Figure 3-6: Radiographs indicating that the anode is highly influenced by relative humidity gradients at 1.5 A-cm-2, 60°C (top), 80°C (bottom). Anode|cathode inlet relative humidity: 50|95% (left), 50|50% (middle), and 95|50% (right). Conditions: 150|150 kPa, 2:2 stoichiometry at 1.2 A-cm^{-2}.
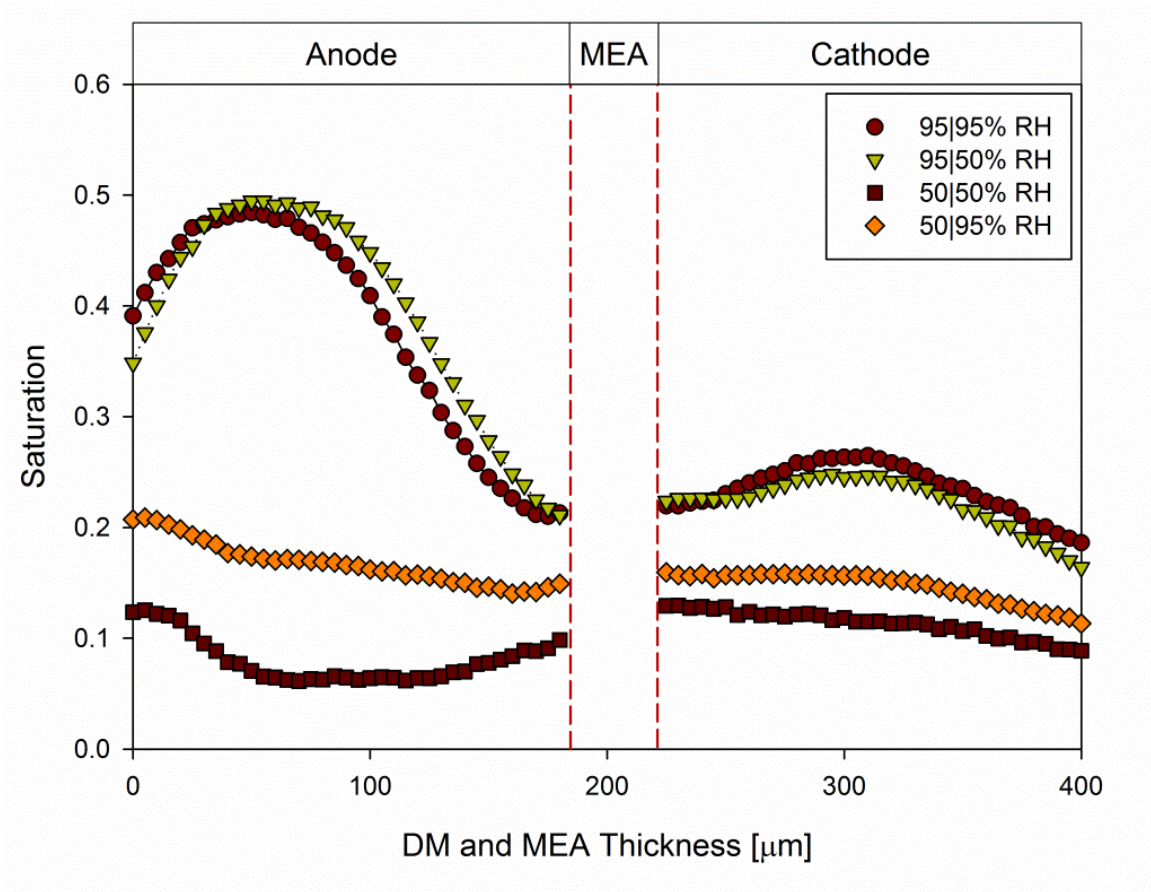
Figure 3-7: Saturation profiles for relative humidity variance (anode|cathode) at 60°C. Conditions: 1.5 A-cm^{-2}, 150|150 kPa, 2:2 stoichiometry at 1.2 A-cm^{-2}.
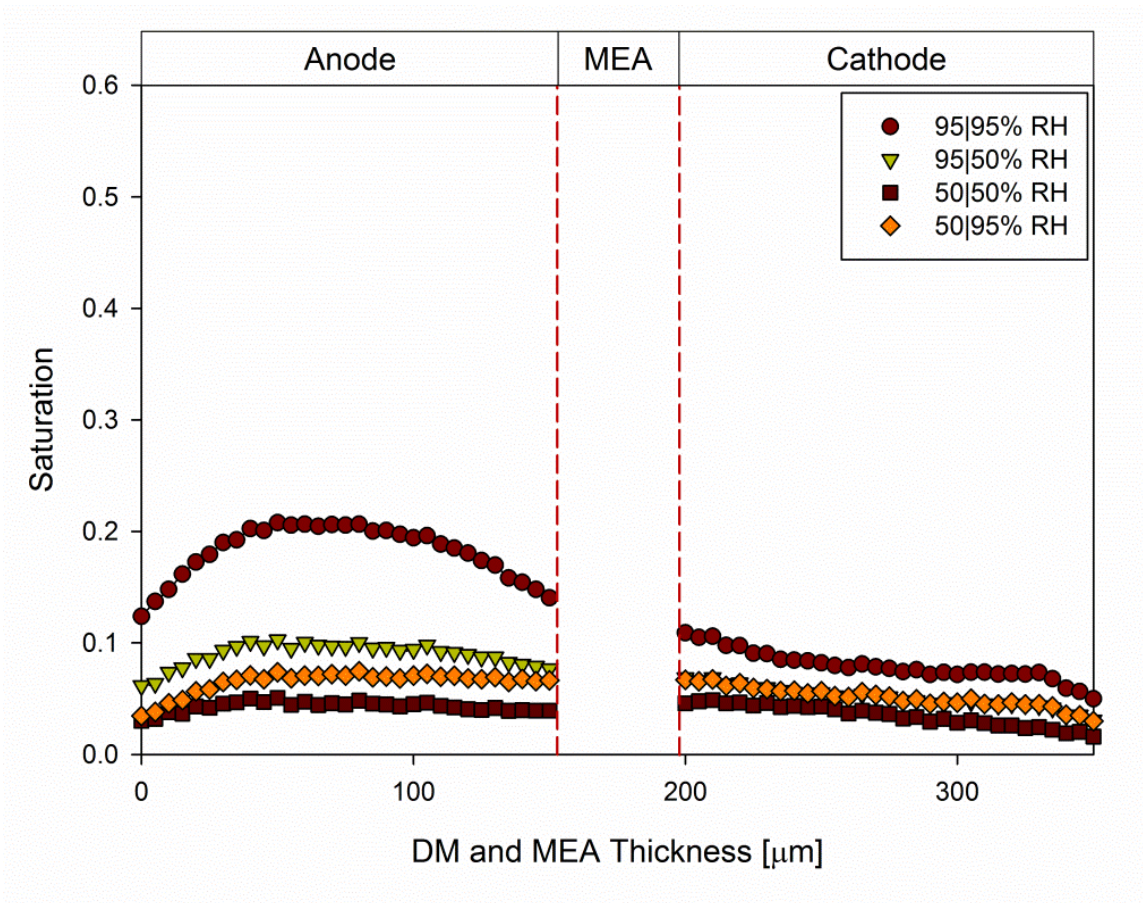
Figure 3-8: Saturation profiles for relative humidity variance (anode|cathode) at 80°C.

Conditions: 1.5 A-cm^{-2}, 150|150 kPa, 2:2 stoichiometry at 1.2 A-cm^{-2}.
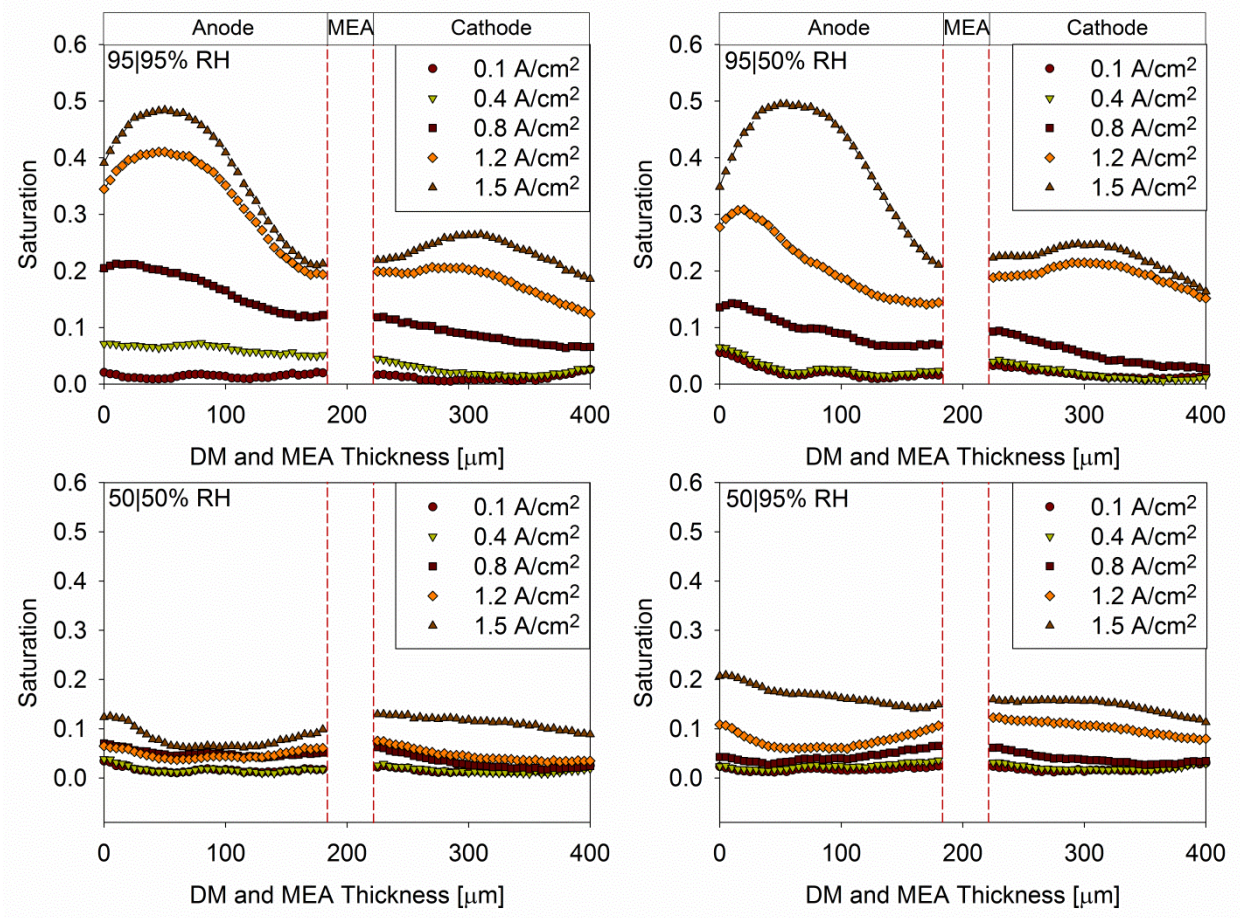
Figure 3-9: Saturation profiles at 60°C as a function of current density and inlet relative humidity (anode|cathode).
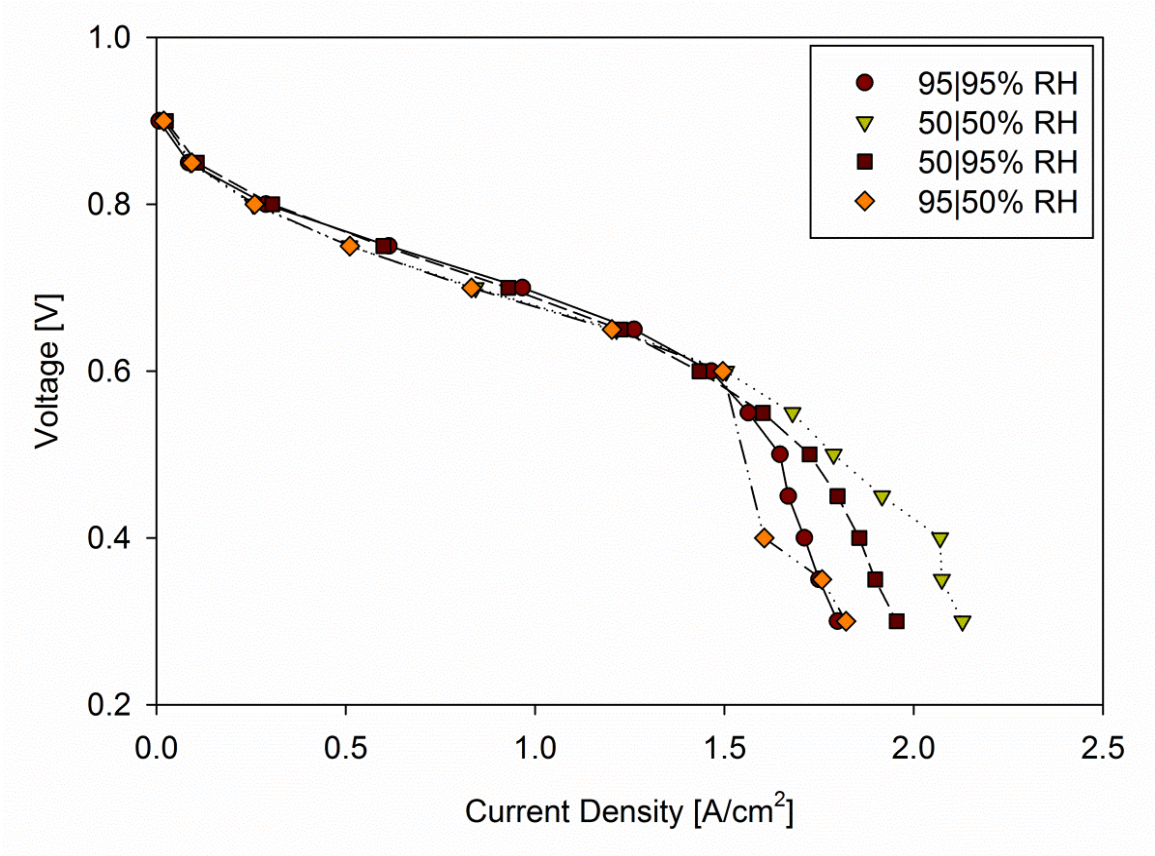
Figure 3-10: Polarization curve at 60°C for relative humidity gradient (anode|cathode) test cases. Effects of high anode water content can be seen with the decreased performance at high current densities.

saturation. Figure 3-11 shows how through-plane saturation varies along the flow path direction. Diffusion media saturation levels show significant channel-to-land variation at the inlet of the image (x=0) where gas streams are not completely saturated. As water accumulates in the gas channels this variation begins to decrease as the driving force to remove water from the DM is reduced. Large datasets of this nature are valuable for the fuel cell modeling community as an extensive source of validation conditions. Many of the conditions presented in this work are very wet and pose challenges for model prediction.

3.4 Conclusions

In this work, high resolution neutron radiography was used to capture the through-plane water content of commercially available fuel cell materials. Test conditions were chosen to produce extremes in water content to provide challenging data for multiphase modeling validation. The large datasets of water saturation and additional portions of this project are publically available via an internet based database at www.pemfcdata.org. This database provides validation datasets for the fuel cell community to use to improve modeling overall, and covers a wider range of data then is presented here.

An asymmetric flow field design where the anode land was three times the size of the cathode land was used in this work. Anode water content was found to be sensitive to changes in RH and pressure gradients. The highest anode water content reached approximately 50% saturation for cases with 95% anode inlet RH and/or low anode exhaust pressure. The cathode water content was found to be primarily
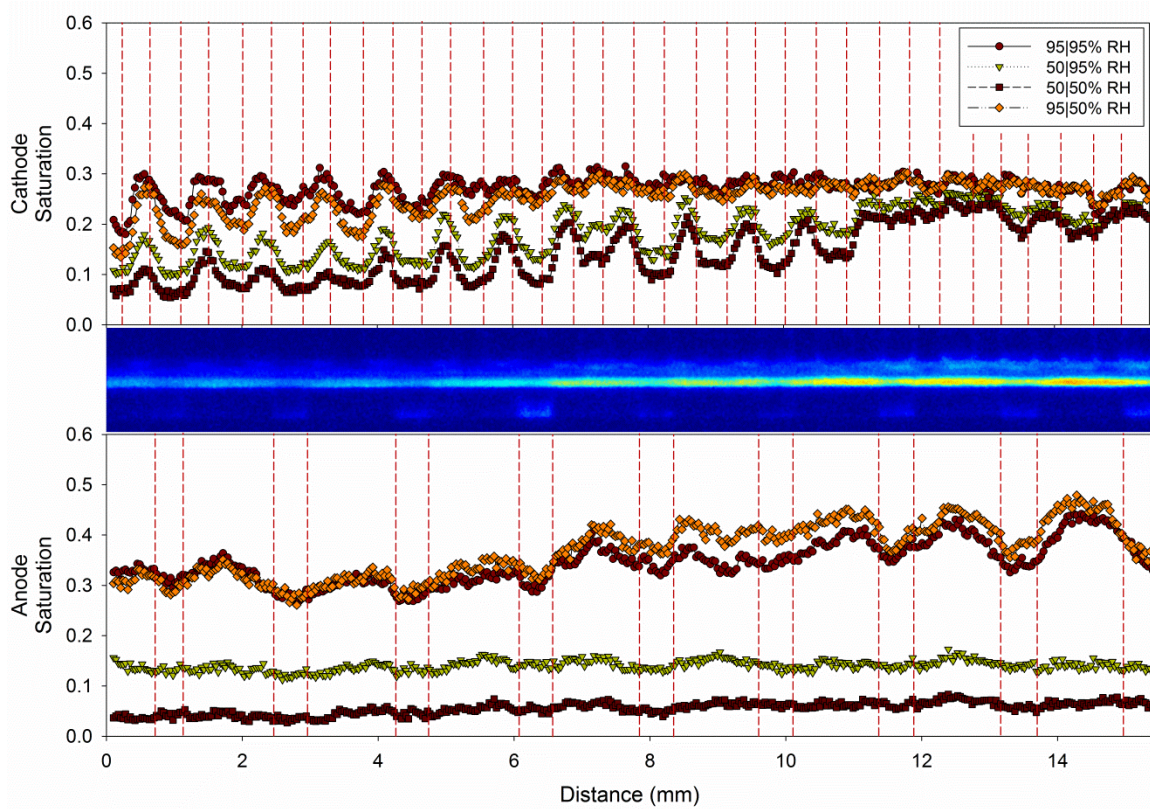
Figure 3-11: Inlet-to-outlet variation of water content with varying inlet relative humidity (anode|cathode) at 60°C, 150|150 kPa, 2:2 stoichiometry at 1.2 A-cm-2, inlet at x = 0 and outlet at x = 14.8. Neutron image corresponds to the 95|50% RH case.

influenced by anode relative humidity and remained relatively consistent when anode RH was fixed at 95%.

The asymmetric flow field design used here results in accumulation of water on the anode. This accumulation can be used to maintain anode side membrane hydration during high current density operation where back diffusion cannot keep up with electro-osmotic drag. Tailoring of the flow field geometry and amount of pressure and/or concentration gradient is necessary to prevent flooding conditions that were seen while providing the maximum amount of storage to prevent anode dry-out. Work is ongoing to determine transport parameters from these datasets and decouple geometric and gradient effects.

CHAPTER 4: Flow Field and Thermally Driven Transport Influences on PEFC Water Balance

This chapter has been accepted for publication in ECS Transactions:

J.M. LaManna, and M.M. Mench, "Engineering Net Water Balance in Polymer Electrolyte Fuel Cells," ECS Transactions, 226th ECS meeting, Cancun, Mexico, October 5-9, 2014.

 I am fully responsible for the work submitted in this publication.

4.1 Introduction

Engineering of water storage and transport in polymer electrolyte fuel cells is an important issue for high power operation, reliability, and durability [105]. The thermal conductivity of the diffusion media (DM) has a strong influence on the temperature gradient within a single cell [6, 106] which can be on the order of several degrees Celsius. This thermal gradient has the potential to drive water vapor diffusion from the high temperature to the low by the phase-change-induced (PCI) flow [66, 67, 107]. It has been shown via neutron imaging that PCI flow may be the dominant driving force for water transport [68] and can be tailored to facilitate improved water removal during shutdown [108].

The work below focuses on determining the thermal influence in anode water build up seen in fuel cells with asymmetric flow field geometries with large anode land widths as discussed in LaManna et al. [97]. Excessive anode water build up has been

linked to fuel starvation and degradation modes [109, 110] and increased purge time and energy [18, 111]. The presentation will also present a compilation of other pathways we have explored computationally and experimentally to engineer water transport in PEFCs. This includes interfacial engineering of the MPL|CL structure, architectural changes described here, and variation of the thermal and mass transport resistance in the microporous layers.

4.2 Method of Approach

4.2.1 Neutron Imaging

Neutron imaging was conducted at the Neutron Imaging Facility at the NIST Center for Neutron Research in Gaithersburg, MD. A specialized 4.8 cm^2 cell with liquid temperature control was developed to facilitate high resolution imaging. An in-depth discussion of the cell design and operation is available in [97]. Testing was conducted with two styles of flow fields, symmetric and asymmetric. The symmetric flow field has 0.5 mm square channels with 0.5 mm lands for both the anode and cathode whereas the asymmetric case has large, 1.5 mm wide anode lands as shown in Figure 4-1.

4.2.2 Model Development

A two-part model has been developed to determine the influence of thermal conductivity and temperature gradient on vapor phase transport. The first part of the model consists of a 2-D steady-state thermal study in COMSOL 4.3a. This model solves for the two-dimensional steady state temperature distribution in a representative section of the fuel cell shown in Figure 4-2. The diffusion media has been sectioned into 15
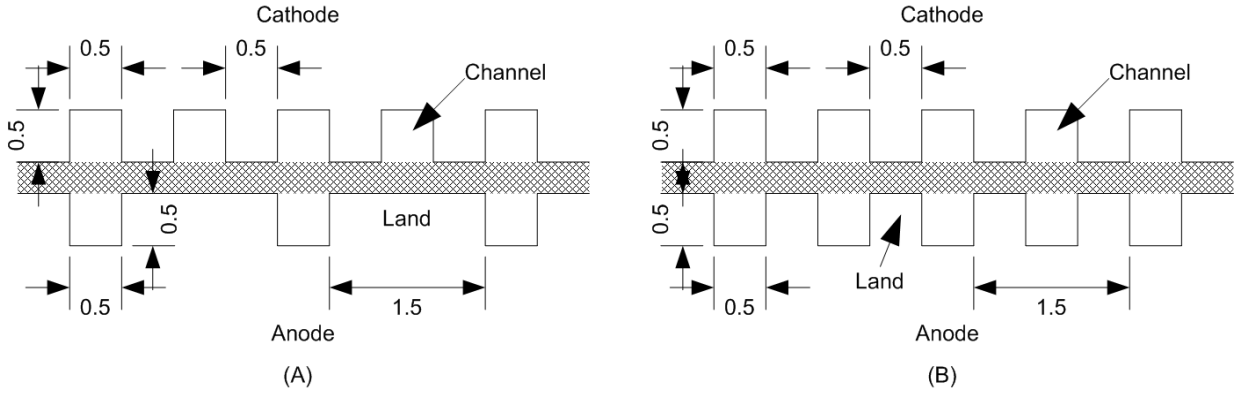
Figure 4-1: Channel dimensions for (A) asymmetric and (B) symmetric flow configurations.

regions for each half of the cell to allow for variable thermal conductivity inputs.

Diffusion media thermal conductivity as a function of saturation was measured, and used to determine influence of actual operational conditions compared to standard dry thermal conductivity. The correlation for thermal conductivity as a function of saturation was developed by Xu et al. [106] and is given in Equation (4.1).

$$k_{wet} = 0.1872 + 0.52403(1 - e^{-s/0.6967}) + 0.11151(1 - e^{-s/0.03477}) \tag{4.1}$$

The neutron images collected were used to determine the saturation for actual operating conditions for the asymmetric and symmetric cases. MATLAB was used to convert the saturation values for the entire imaged area of the neutron images to saturation using Equation (4.1). A region of interest was then selected that matched the computational domain of the model as highlighted near the exit region in the center image of Figure 4-3. The region of interest was then split into subsections that match

Figure 4-2: Computational domain that represents the asymmetric case. Green boundaries represent prescribed temperature boundary conditions. Grey areas represent the DM, orange areas represent the catalyst layers, and the blue area the membrane.

the sectioned regions of the DM to determine average wet thermal conductivity for that region.

The heat generation is determined for a single cell operating at 0.6 V, 1.0 A/cm², 333 K, and 150 kPa exhaust pressure using Equation (4.2) [6].

$$ q''' = \frac{i}{t_{cl}} \left[\left(\frac{T\Delta S}{nF} \right) + \eta \right] \tag{4.2} $$

Where i is the current density, t_{cl} is the catalyst layer thickness, ΔS the half-cell entropy change, η is the over-potential, n is the number of electrons per mole of reactant, and F is the Faraday Constant. The ΔS value for generation in the cathode catalyst layer is -326.36 J/mol-K.
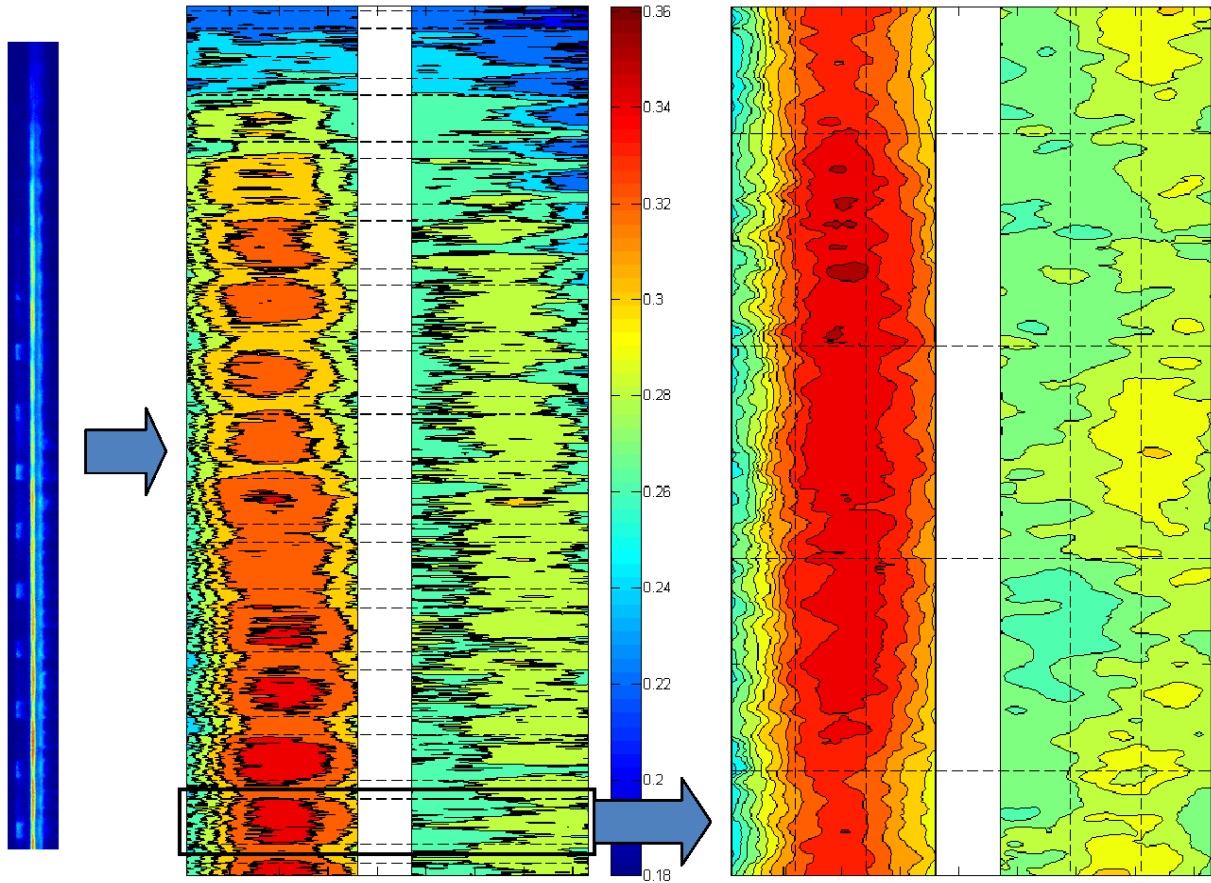
Figure 4-3: Process to convert saturation values to thermal conductivity. Saturation from neutron images are converted to thermal conductivity via correllation [106], regions are selected for COMSOL domain, hashed lines in the right image represent areas that are averaged for input into COMSOL.

The second portion of the model calculates the PCI flow across the anode and cathode diffusion media. PCI flow is induced by by the presence of a temperature gradient that drives changes in concentration. The PCI molar flux can be approximated using Fick's law for diffusion

$$J = D_v^{eff} \frac{\partial C}{\partial x}$$
(4.3)

Concentration, C, and the effective diffusion coefficient, D_v^{eff}, can be estimated:

$$C = \frac{P_{sat}}{RT}$$
(4.4)

$$D_v^{eff} = D_{v_0} \left[\phi(1-s) \right]^{1.5} \left(\frac{T}{T_0} \right)^n \left(\frac{p_0}{p} \right)$$
(4.5)

Where P_{sat} is the local saturation pressure, R is the ideal gas constant, T is the local temperature, ϕ is the porosity, s is saturation, T_0 is standard temperature of 273.15 K, P_0 is standard pressure of 101 kPa, the constant n is 1.81, and the diffusivity D_{v0} is $0.226*10^{-4}$ m^2/s [112].

4.3   Results and Discussion

4.3.1 Temperature Variation

The temperature maps obtained from COMSOL are plotted in Figure 4-4. The vertical black lines represent the boundaries between the layers. As can be seen in the

55

contour maps, the large anode lands of the asymmetric case reduce the temperature peak near the center of the plot by approximately 2°C. Adding saturation to both cases results in a reduction in temperature as the net conductivity is increased with saturation. Thus, as the diffusion medium becomes more saturated, the PCI mode of transport is reduced, and the PCI flux is not constant.

4.3.2 Temperature Driven Mass Transport

To estimate the PCI flux across each diffusion media, temperature profiles are taken along the boundaries of the DM with the channel and catalyst layers. The channel profile is subtracted from the catalyst profile for both the anode and cathode to determine the differential temperature across the layer, as plotted in the left image of Figure 4-5. It can be seen that the cathode DM has a higher temperature difference along the majority of the domain except for the location in the center of the large anode land. The cathode channel that is located across from the center of the anode land causes a localized temperature increase due to the lack of heat removal, as seen in Figure 4-4. This increase in temperature reduces the differential while the anode's large land provides a relatively uniform differential along the entire land length.

The temperature differential for asymmetric dry case shown in the left side of Figure 4-5 was used to determine the PCI molar flux across the anode and cathode diffusion media. To normalize this flux, it is plotted as a ratio with the water generation flux in the right image of Figure 4-5. The flux ratio follows the temperature trends as the concentration is dependent on temperature. The differential temperature profiles and flux ratios were then calculated for all four cases.
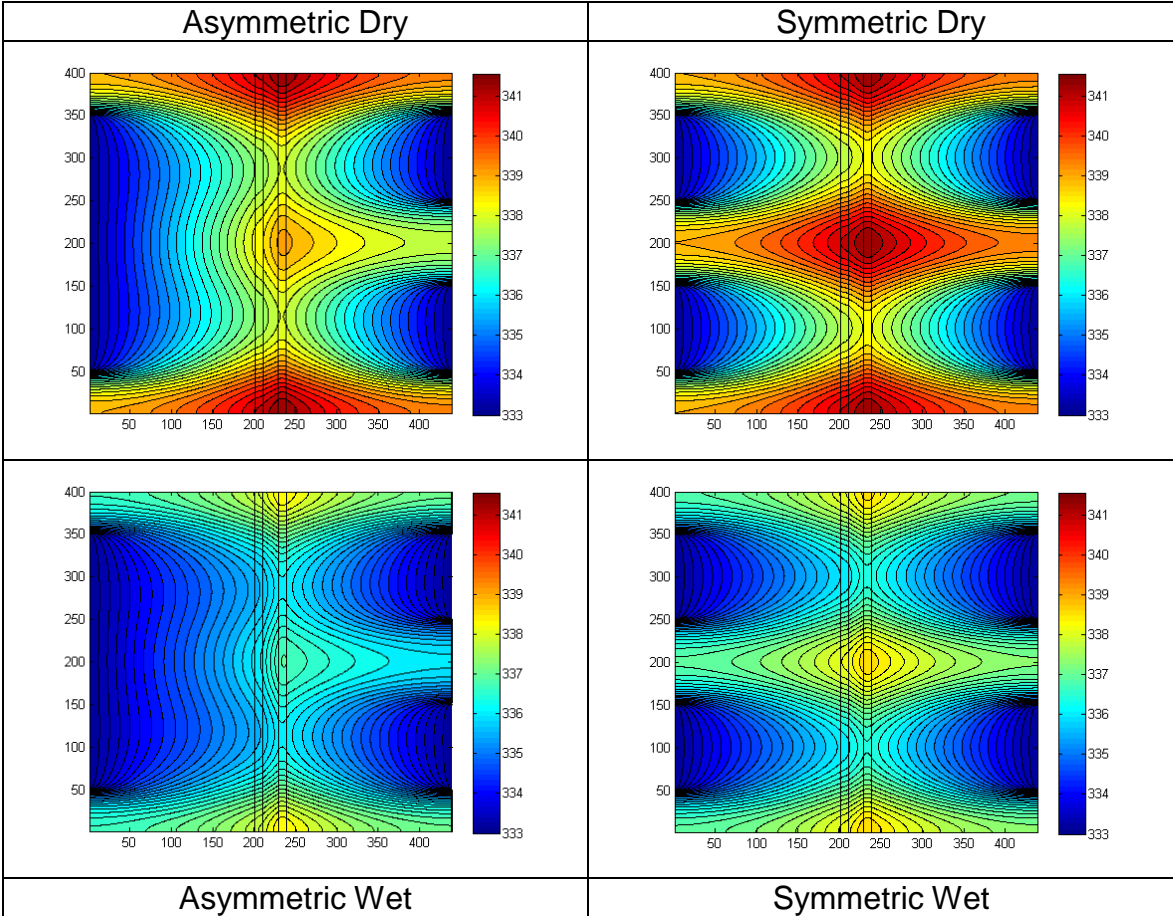
Figure 4-4: Calculated internal temperature distributions for the four cases tested
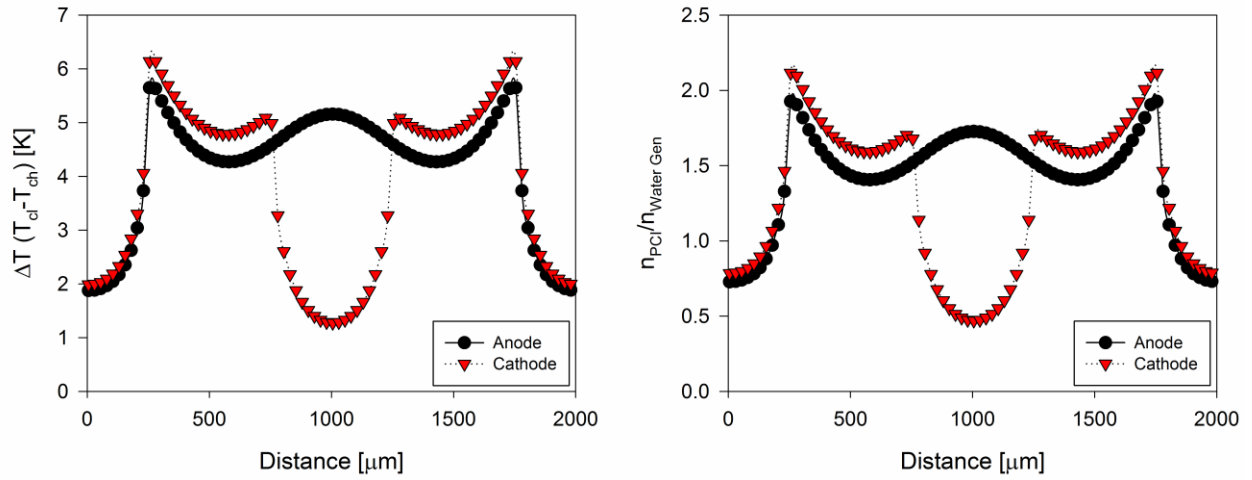
Figure 4-5: Differential temperature across anode and cathode DM for asymmetric dry test case (left) and ratio of PCI molar flux to water generation flux for asymmetric dry case (right).

The cathode flux ratio was subtracted from the anode flux ratio for each test case to determine the preferential direction and magnitude of water transport. A positive value indicates a stronger PCI flux towards the anode while a negative value indicates a stronger cathode PCI flux. This difference is shown in Figure 4-6. The difference for all four cases is preferential towards the cathode in the areas above the outer cathode channels and lands. In the region over the center of the large asymmetric anode land the difference turns very positive compared to the rest of the trend. This anode preference is due to the inversion in temperature differences seen in Figure 4-5. The water build up that was seen in the asymmetric neutron images is partially due to this localized area of thermal pumping and the increase in water storage volume under the land.

The effects of saturation are also evident in Figure 4-6. Both wet cases see a shift towards zero from their respective dry cases. This is due to the reduction in temperature from the higher apparent thermal conductivities of the diffusion media.

4.4   Conclusions

In the presentation accompanying this transaction, various methods for engineering the water transport in PEFCs will be discussed. This includes interfacial engineering of the MPL|CL structure, architectural changes, and variation of the thermal and mass transport resistance in the microporous layers. As discussed in detail in this transaction, experimental and computational examination of neutron imaging data was combined with a water transport model with two-dimensional thermal effects to determine the cause of water accumulation in a fuel cell with asymmetric flow field layouts. The model

59
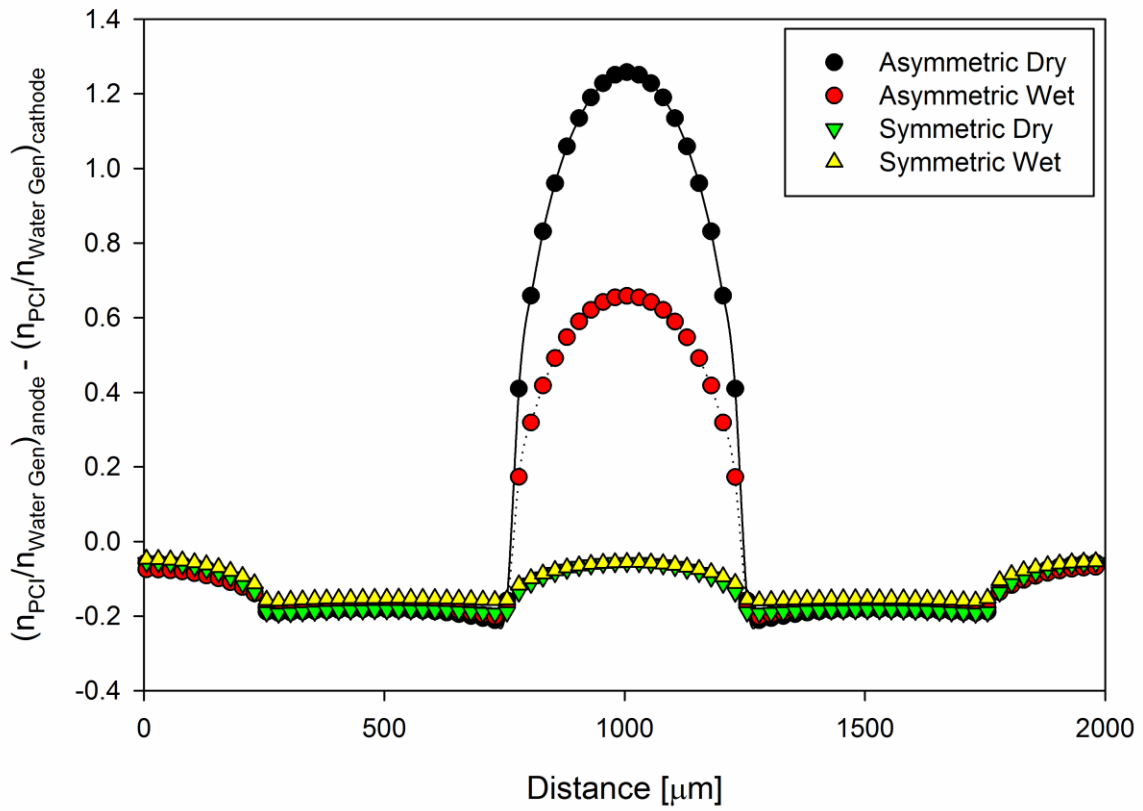
Figure 4-6: Anode PCI/Water gen flux ratio minus cathode PCI/Water gen flux ratio. Negative number indicates a stronger cathode PCI flux and a positive number indicates a stronger anode PCI flux.

accounts for changes in apparent diffusion media thermal conductivity due to liquid water saturation. It was found that saturation has a significant effect on temperature profile and must be accounted for in transport models. Water accumulation and high saturation values seen in asymmetric flow pattern anodes is primarily due to the large thermal pumping action of PCI flow due to a temperature differential inversion in the center area of the large anode land. This can be used as a design guideline to direct thermal management design of a fuel cell to either reduce anode water build up to decrease degradation or increase anode water to prevent anode membrane dry out at very high current densities.

CHAPTER 5:   Fuel Cell Channel-Land Configuration Control of Temperature Driven Water Transport

This chapter will be submitted for publication in The Journal of the Electrochemical Society with the following authors and title:

J.M. LaManna, and M.M. Mench, "Channel-land configuration control of temperature driven water transport in polymer electrolyte fuel cells"

My primary contribution is the entirety of this work.

5.1   Introduction

Due to the small length scales and high power of fuel cells, strong temperature gradients can exist. These gradients can be on the order of 10-20°C across a 200 μm layer [6, 106]. The temperature difference across the diffusion media (DM) has a strong influence on water transport via thermally driven diffusion. This process is known as Phase-change-induced (PCI) flow or the heat-pipe effect and has been shown to have a strong influence on water transport [66-68] and is similar to the membrane process, thermo-osmosis [113]. PCI flow works due to concentration changes as a result of temperature changes within the cell. This drives water vapor from the hot locations near the catalyst layers to the cool regions near the channels.

    This chapter will focus on determining the influence that channel-land configuration and asymmetric anode|cathode channel patterns have on PCI flow and cell water balance. High resolution neutron imaging will be used to investigate the

internal through-plane liquid water profiles through the anode and cathode DM for two fuel cell configurations. A non-dimensional Thermal Transport Number is proposed to explain the influence of channel-land configuration on cell water balance.

5.2   Method of Approach

5.2.1   Cell Design

A 4.8 cm^2 cell was used for this work that was developed to facilitate high resolution neutron imaging with precise thermal boundary conditions. The cell has a narrow 9 x 53 mm active area to reduce geometric unsharpness and beam hardening effects. Coolant channels are place directly behind the current collectors to provide precise thermal boundary conditions on the cell. Temperature of the coolant was controlled with a circulator bath with ±0.2°C accuracy. Additional details on the cell along with information on reduction of the neutron images can be found in Chapters 2 and 3 along with Ref. [97].

To better understand the driving force behind the large water accumulation in the anode seen in Chapter 3, two flow field configurations were tested in this work, the baseline asymmetric configuration from Chapter 3 and a new symmetric flow configuration. This symmetric configuration uses the 1 mm cathode pitch from the asymmetric case for both the anode and cathode as shown in Figure 5-1. The symmetric and asymmetric flow fields consist of a triple serpentine flow pattern with 0.5 mm square channels. The symmetric pattern has 0.5 mm lands on both the anode and cathode whereas the asymmetric pattern has 1.5 mm anode lands and 0.5 mm cathode lands.
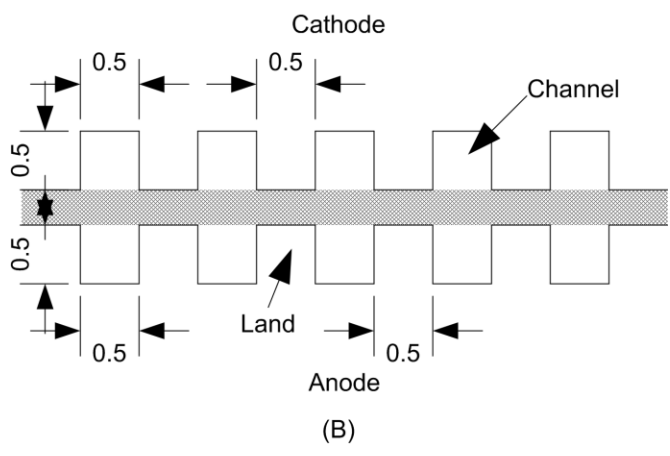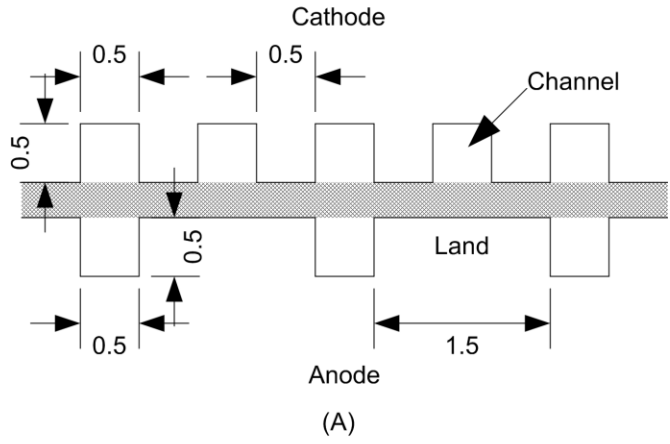
Figure 5-1: Channel and land dimensions for asymmetric (A) and symmetric (B) configurations.

The materials tested were the same as in Chapter 3. The DM used was Mitsubishi Rayon Corporation U105 that has a 230 µm thickness with 6% wt. PTFE and 30 µm MPL coating. A W.L. Gore & Associates, Inc. Select Series 5720 18 µm membrane with 0.3 mg/cm^2 cathode loading and 0.05 mg/cm^2 anode loading were used.

5.2.2 Test Facility

Neutron imaging was conducted at the BT-2 Neutron Imaging Facility at the NIST Center for Neutron Research located in Gaithersburg, MD. Imaging was achieved with the 15 µm effective resolution microchannel plate detector. The Neutron Imaging Facility has standard fuel cell testing equipment that allows precise control of gas flow rates, gas composition, gas and cell temperature, gas humidification, inlet and outlet pressure, current, and voltage.

Each test condition was run for 5 minutes to stabilize and then imaged for 20 minutes at steady state. The long image length was required to achieve high enough neutron counts for each image. Detailed information regarding reduction of the neutron images to water thickness and conversion to saturation can be found in Chapter 3. Porosity data for the MRC diffusion media was obtained from Ref. [114].

5.2.3 Test Conditions

Test conditions were the same as described in Chapter 3 to allow for direct comparison of the symmetric and asymmetric cell configurations. Variables that were tested include current density, cell temperature, inlet relative humidity, and exhaust pressure. Flow

Table 5-1: Operating Parameters

Operating Parameters	Values [units]
Current Density	0.1, 0.4, 0.8, 1.2, 1.5 [A/cm^2]
Temperature	40, 60, 80 [°C]
Pressure Gradient anode|cathode	100|150, 150|150, 150|100 [kPa(a)]
Concentration Gradient anode|cathode	50|50, 95|50, 50|95, 95|95 [inlet %RH]

rate was held constant across all test conditions regardless of current density with an equivalent stoichiometric ratio of 2\|2 at 1.2 A/cm^2. Inlet relative humidity was held at a constant 95\|95%RH (anode\|cathode) during exhaust pressure testing while exhaust pressure was held at a constant 150\|150 kPa(a) (anode\|cathode) during relative humidity testing. An overview of conditions tested is given in Table 5-1.

5.2.4 Thermally Driven Flow Model

Two-dimensional temperature distributions were calculated for the symmetric and asymmetric configurations for dry and wet cases using COMSOL 4.3a. A detailed description of how thermal conductivity is adjusted for saturation is given in Chapter 4. Heat generation was determined using Equation (5.1) [6].

$$q''' = \frac{i}{t_{cl}} \left[\left(\frac{T\Delta S}{nF} \right) + \eta \right]$$

(5.1)

Where i is current density, t is the catalyst layer thickness, T is temperature, ΔS is the half-cell entropy change, n is the number of electrons per mole of reactant, F is the

Table 5-2: Model Parameters

Variable	Value
current density 1	0.1 A/cm^2
current density 2	0.4 A/cm^2
current density 3	0.8 A/cm^2
current density 4	1.2 A/cm^2
current density 5	1.5 A/cm^2
voltage 1	0.8 V
voltage 2	0.7 V
voltage 3	0.625 V
voltage 4	0.55 V
voltage 5	0.5 V
DM dry thermal conductivity	0.18 W/m-K
CL thermal conductivity	0.3 W/m-K
Membrane thermal conductivity	0.16 W/m-K
DM thickness	200 µm
CL thickness	10 µm
Membrane thickness	18 µm

Faraday constant, and η is the over-potential. The entropy change for the cathode reaction is -326.36 J/mol-K and 0.104 J/mol-K for the anode. Joule heating is considered for the membrane. The values for the variables in Equation (5.1) and used in COMSOL are given in Table 5-2.

The 2-D temperature profiles are then used to calculate the PCI flux across the anode and cathode diffusion media. Temperature profiles are taken along the DM|CL and DM|channel interfaces for both DM and are used to calculate water vapor concentration gradients across each DM via Equation (5.2).

$$C = \frac{P_{sat}}{RT} \qquad (5.2)$$

With concentration as a function of temperature, Fick's Law of Diffusion (Equation (5.3)) is used to calculate the maximum flux across each DM for each node along the interface.

$$J_{PCI} = D_{eff}\frac{\partial C}{\partial x} \qquad (5.3)$$

To determine which half of the cell had the dominant PCI flux, a new parameter was developed. This parameter is called the Thermal Transport Number (TTN) and represents the normalized cathode PCI flux with respect to generated water subtracted from the normalized anode PCI flux as seen in Equation (5.4).

$$TTN = \left(\frac{J_{PCI}}{J_{gen}}\right)_{anode} - \left(\frac{J_{PCI}}{J_{gen}}\right)_{cathode} \qquad (5.4)$$

This equation represents the maximum thermal transport driving force for water transport. A positive TTN value represents a preference for anode transport while a negative number implies a preference for cathode transport. Assuming the anode and cathode sides of the membrane have the same water content and the membrane has zero resistance for water transport than a positive TTN would draw water to the anode from the cathode catalyst layer.

5.3   Results and Discussion

5.3.1 Neutron Imaging

Water thickness data measured with neutron imaging was converted to saturation values for each condition. Beginning with the exhaust pressure testing at 40°C plotted in Figure 5-2 it can be seen that significant variation occurs between the two configurations. The asymmetric case has large sensitivity to the imposed gradient with large fluctuations in anode water content. Maximum saturation varies from approximately 15% for the 150|100 kPa case to 60% for the 100|150% case. This fluctuation is not seen in the symmetric case. Maximum anode water content does not scale with land width as the asymmetric case has 3 times the land width but only double the water content. The cathode saturation profiles for both cases follow similar trends with matching boundary saturation values at the MPL and the flow field. The increase in peak water content from 30% for asymmetric to 35% for the symmetric case indicates
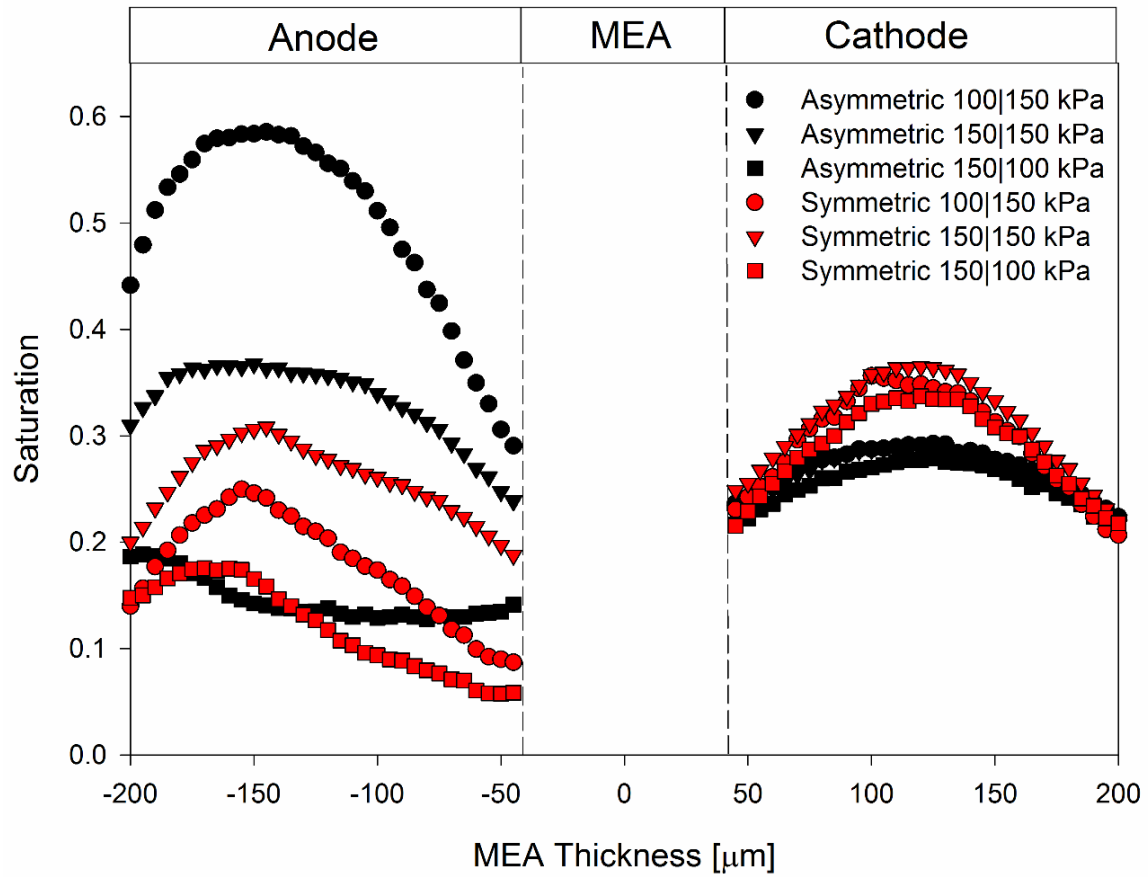
Figure 5-2: Exhaust pressure condition saturation profiles for 0.8 A/cm^2 at 40°C test conditions for asymmetric and symmetric configurations. Test conditions: 95|95% inlet RH, constant gas flow rates with equivalent 2|2 stoichiometry at 1.2 A/cm^2.

an increase in water removed from the cathode. This would agree well with the reduction in anode water content.

Increasing the temperature to 60°C, exhaust pressure saturation profiles are compared for both configurations at 1.2 A/cm^2. Similar trends are seen at 60°C (Figure 5-3) as is seen at 40°C with small variation between symmetric cases and large water accumulations in the asymmetric cases. Large variation in the asymmetric water content between cases is not seen at 60°C due to the critical maximum saturation level being reached. This is evident by the fact that the 100|150 kPa and 150|150 kPa [anode|cathode] profiles overlay with each other. At this point the water becomes connected enough across the land to facilitate drainage thus limiting the increase in saturation beyond this point. Cathode peak saturation increases for the symmetric case from approximately 30% to 35% due to the increased water removal on the cathode side. The boundaries for the cathode remain consistent between cases even with increased peak saturation for the symmetric condition. This is expected as the boundaries, MPL and flow field, are identical between configurations and this behavior should follow between the two.

The reduction in anode water content in the symmetric configuration indicates both a reduction in back diffusion of water from the cathode and reduced storage due to a change in critical saturation level. Net water drag coefficients were measured for all pressure conditions for both configurations at 60°C to determine the reduction in back diffusion from the cathode to anode. It can be seen for all cases in Figure 5-4 that the symmetric case has net water drag coefficients more positive than the asymmetric
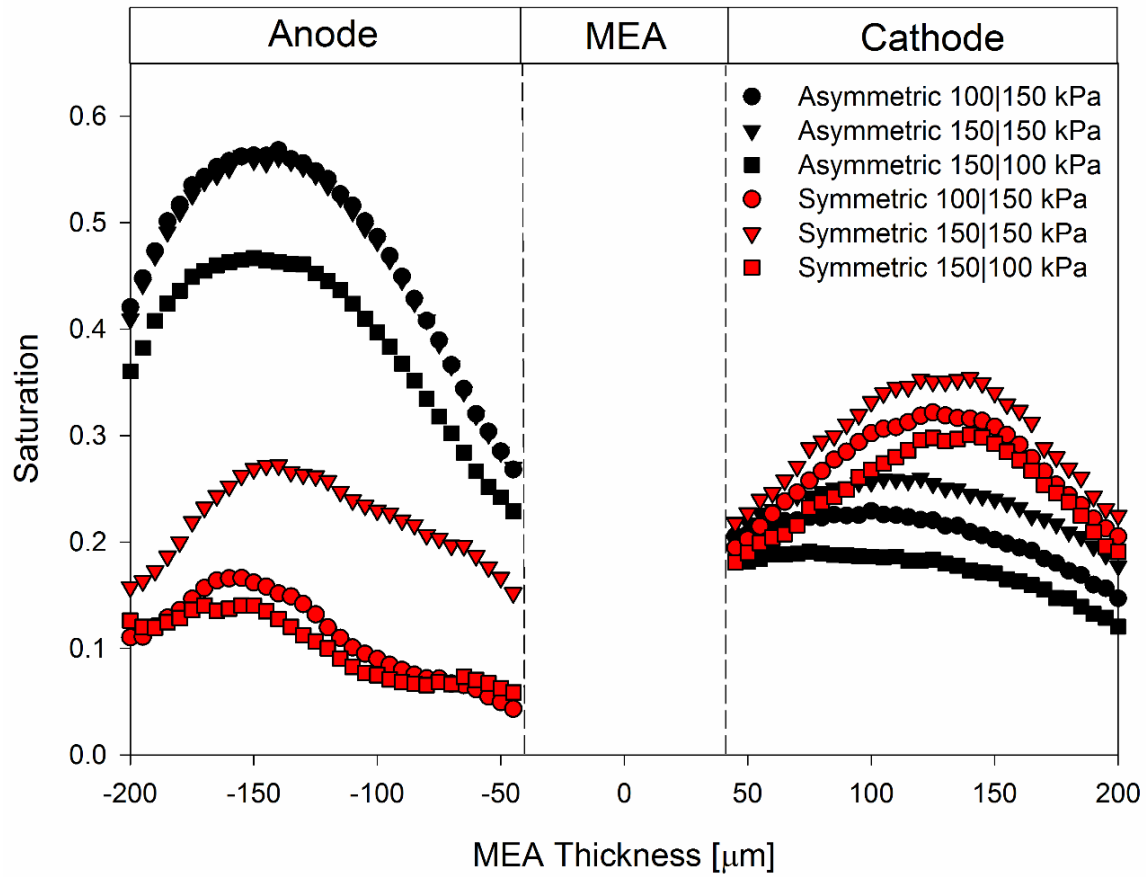
Figure 5-3: Saturation profiles for exhaust pressure conditions at 60°C operating at 1.2 A/cm². Test conditions: 95|95% inlet RH, constant gas flow rates with equivalent 2|2 stoichiometry at 1.2 A/cm².
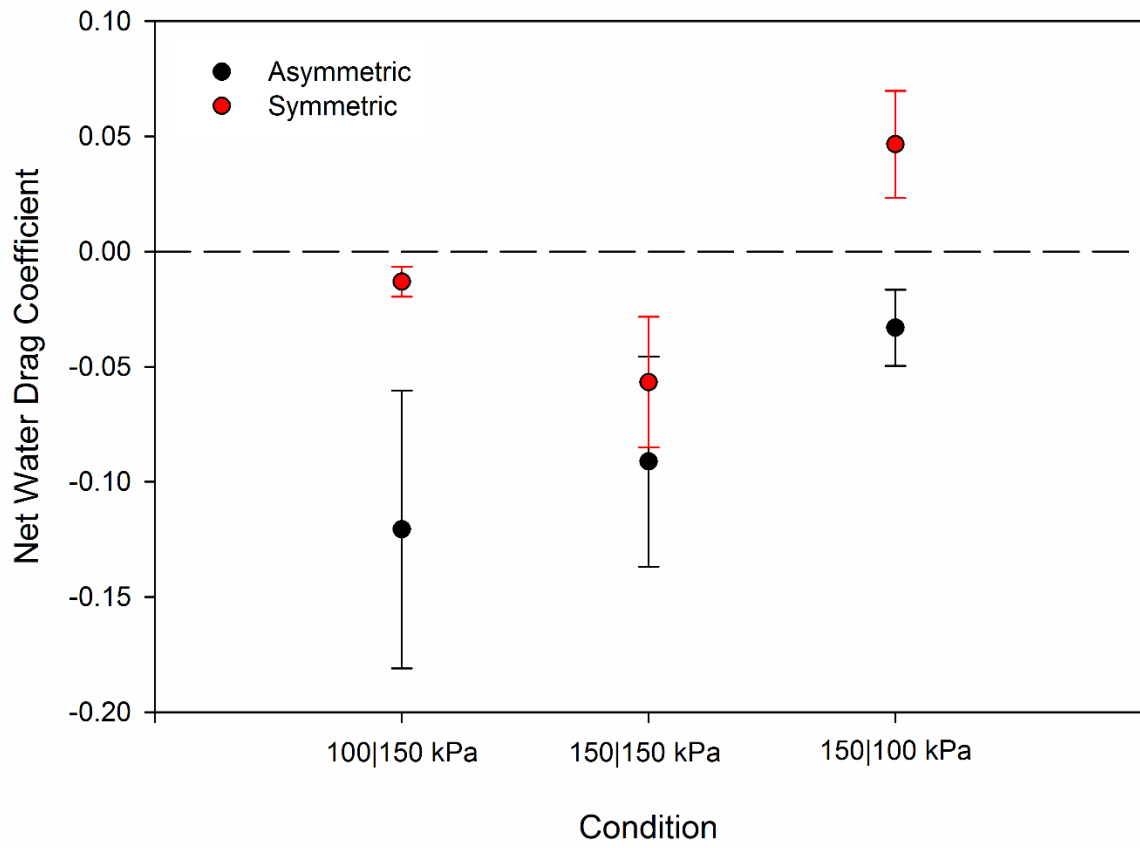
Figure 5-4: Net water drag coefficients for 60°C exhaust pressure test conditions.

configuration. The large anode lands of the asymmetric configuration provide large cool regions that drive thermal transport from the cathode to the anode.

At 60°C, inlet gas stream relative humidity was varied for both the anode and cathode to determine the influence of concentration driven flow across the cell. Figure 5-5 shows that the symmetric configuration is invariant with inlet relative humidity while the asymmetric configuration exhibits large fluctuations in saturation depending on humidity levels. As with the pressure conditions, cathode boundary points are similar between configurations indicating no change in boundary interaction due to increased or decreased levels of water transport. The symmetric configuration has a decreased level of anode water content while the cathode has a higher peak saturation that shows a larger flux of water is transported out via the cathode than in the asymmetric configuration. Cathode variability in the asymmetric configuration follows anode saturation levels with lower cathode saturation for the two dryer anode cases.

Water content is significantly reduced for both configurations when the temperature is raised to 80°C as shown in Figures 5-6 and 5-7. The higher temperature facilitates higher levels of vapor transport and reduced levels of condensation within the diffusion media. As seen at the lower temperatures, the asymmetric configuration has higher levels of anode saturation than the symmetric configuration for both the exhaust pressure conditions and inlet relative humidity conditions. A slight increase in cathode saturation levels are seen for the symmetric conditions showing an increases level of water removal through the cathode. The decrease in water content for both configurations allowed all test conditions to run through the entire test duration.
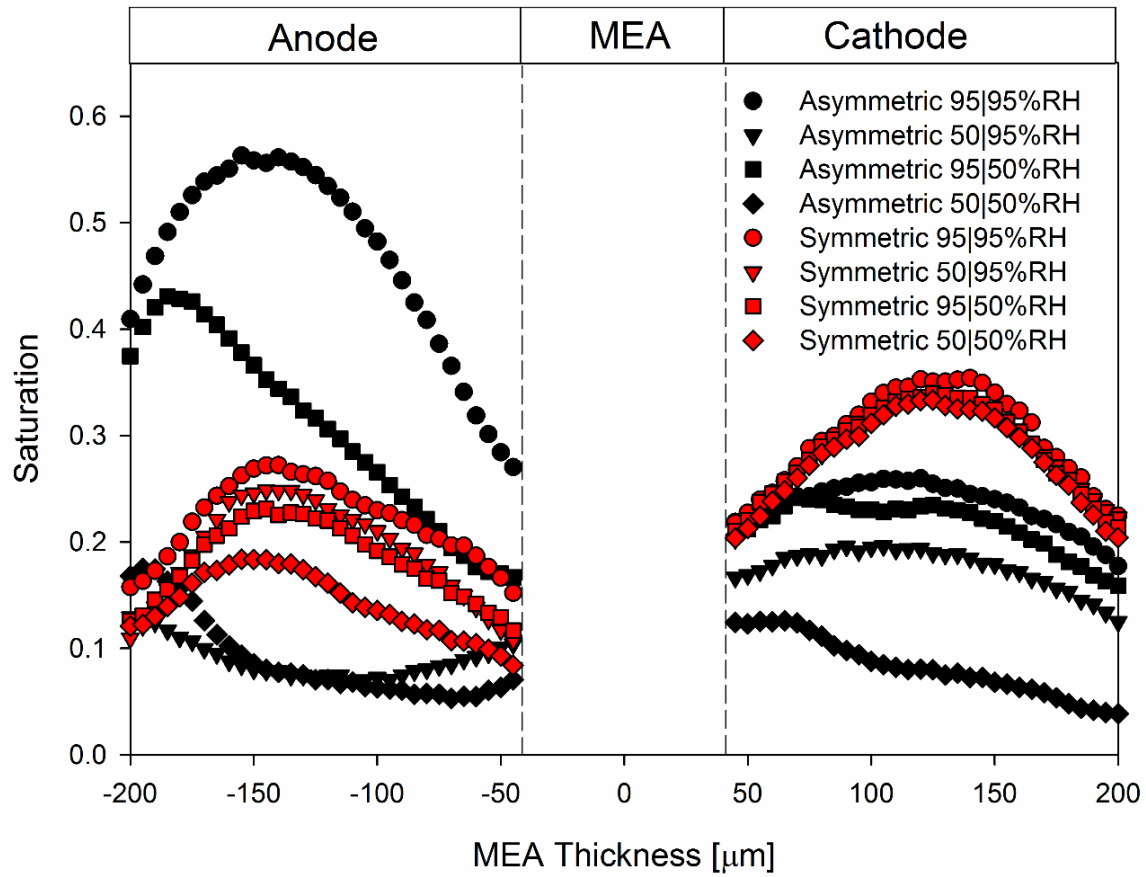
Figure 5-5: Saturation profiles for relative humidity conditions at 60°C operating at 1.2 A/cm^2. Test conditions: 95|95% inlet RH, constant gas flow rates with equivalent 2|2 stoichiometry at 1.2 A/cm^2.
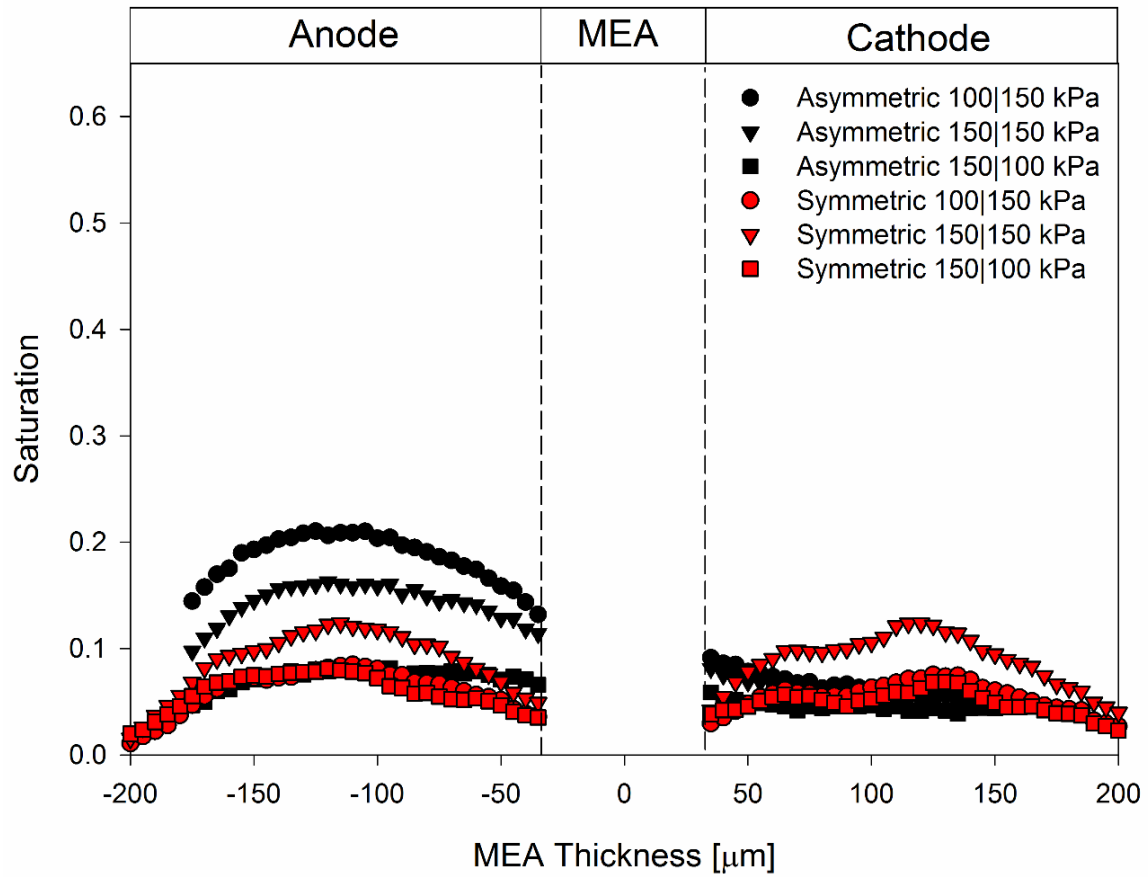
Figure 5-6: Saturation Profiles for exhaust pressure conditions at 80°C operating at 1.5 A/cm². Test conditions: 95|95% inlet RH, constant gas flow rates with equivalent 2|2 stoichiometry at 1.2 A/cm².
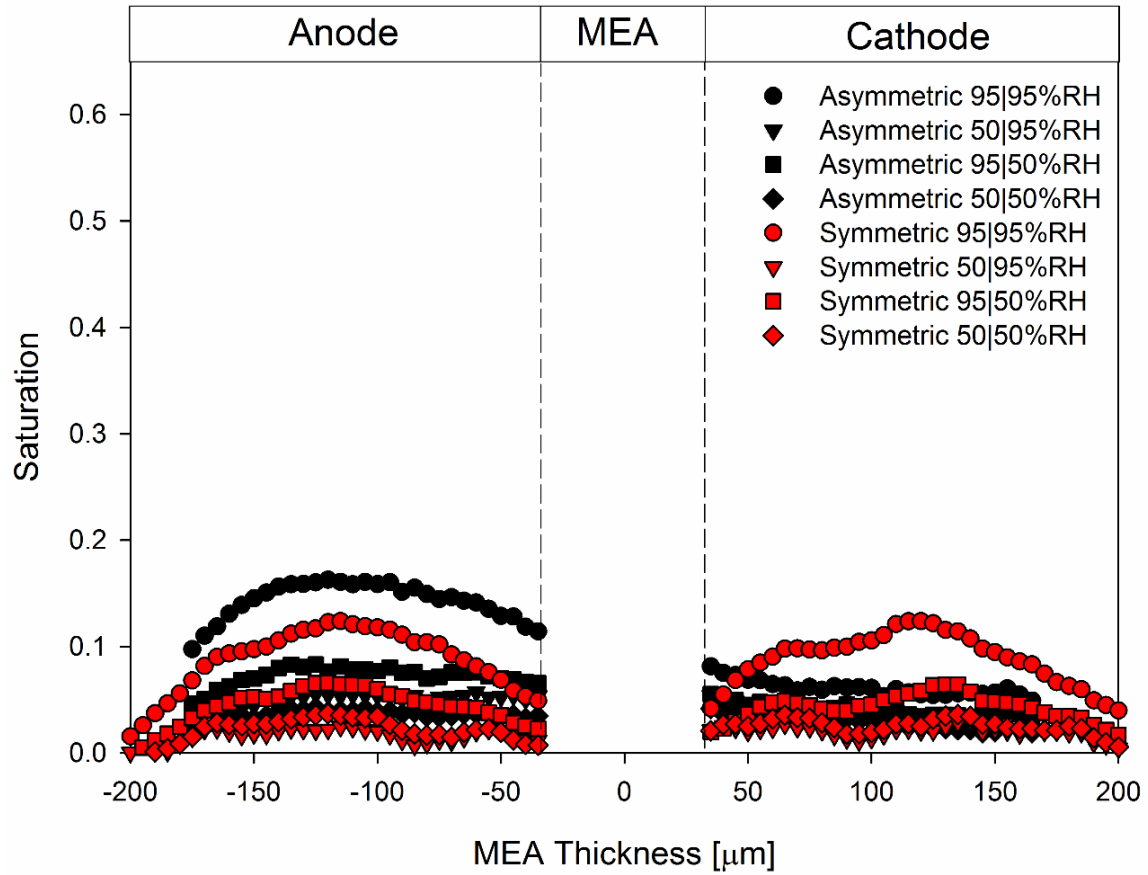
Figure 5-7: Saturation profiles for relative humidity conditions at 80°C operating at 1.5 A/cm^2. Test conditions: 95|95% inlet RH, constant gas flow rates with equivalent 2|2 stoichiometry at 1.2 A/cm^2.

Operating voltages for all test conditions presented in this section are given for both configurations in Table 5-3 below.

5.3.2 Thermal Transport Influence on Water Balance

To better understand the driving force behind the large water accumulation in the asymmetric configuration, it will be necessary to look at the influence of the large anode lands on the 2-D temperature profile. Heat transfer models in COMSOL are used to solve for the 2-D temperature distribution for a 2 mm long representative segment for both configurations. This domain represents the distance required for symmetric boundary conditions for the asymmetric configuration. The TTN is determined along every node along the 2 mm domain which is plotted in Figure 5-8. This figure shows the TTN profiles for the 150|150 kPa cases for each configuration. A positive TTN indicates a preference towards anode driven water balance while a negative number is a cathode driven water balance. Anode and cathode lands for both configurations are overlaid with the plot to show how they influence the TTN.

As evident by Figure 5-8, the symmetric configuration has a preference towards cathode transport while the asymmetric configuration has a large positive spike in the center of the domain that aligns with the center of the large anode land. This spike is due to the insulating effect the cathode channel has in the center of the domain which results in a low CL-to-channel temperature gradient on the cathode side. The large thermal driving force towards the anode in the asymmetric configuration allows a pumping action to draw water to the anode where it collects over the large lands. Transport to the anode is facilitated by the fact that Gore membranes preferentially

78

Table 5-3: Operating voltages for NR profiles

| Condition | Voltage [V] | |
	Asymmetric	Symmetric
40°C		
100|150 kPa, 95|95 %RH, 0.8 A cm^{-2}	0.608	0.651
150|150 kPa, 95|95 %RH, 0.8 A cm^{-2}	0.690	0.608
150|100 kPa, 95|95 %RH, 0.8 A cm^{-2}	0.701	0.634
60°C		
100|150 kPa, 95|95 %RH, 1.2 A cm^{-2}	0.661	0.594
150|150 kPa, 95|95 %RH, 0.1 A cm^{-2}	0.826	0.845
150|150 kPa, 95|95 %RH, 0.4 A cm^{-2}	0.753	0.761
150|150 kPa, 95|95 %RH, 0.8 A cm^{-2}	0.695	0.701
150|150 kPa, 95|95 %RH, 1.2 A cm^{-2}	0.618	0.558
150|150 kPa, 95|95 %RH, 1.5 A cm^{-2}	0.580	0.560
150|100 kPa, 95|95 %RH, 1.2 A cm^{-2}	0.652	N/A
50|95 %RH, 150|150 kPa, 1.2 A cm^{-2}	0.667	0.597
95|50 %RH, 150|150 kPa, 1.2 A cm^{-2}	0.576	0.592
50|50 %RH, 150|150 kPa, 1.2 A cm^{-2}	0.650	0.598
80°C		
100|150 kPa, 95|95 %RH, 1.5 A cm^{-2}	0.496	0.577
150|150 kPa, 95|95 %RH, 1.5 A cm^{-2}	0.508	0.608
150|100 kPa, 95|95 %RH, 1.5 A cm^{-2}	0.383	0.569
50|95 %RH, 150|150 kPa, 1.5 A cm^{-2}	0.670	0.637
95|50 %RH, 150|150 kPa, 1.5 A cm^{-2}	0.665	0.594
50|50 %RH, 150|150 kPa, 1.5 A cm^{-2}	0.619	0.594
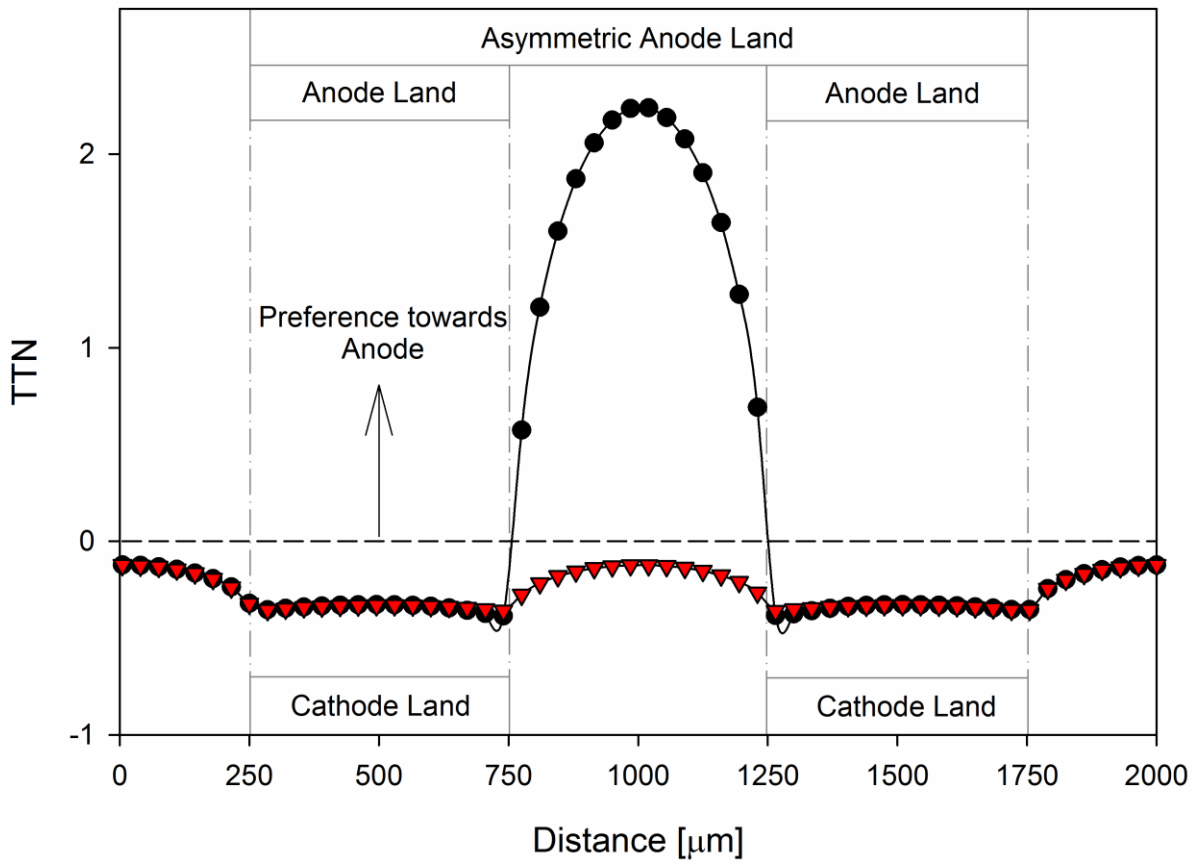
Figure 5-8: TTN plot for 150|150 kPa(a) case at 60°C and 1.2 A/cm^2 showing how channels and lands align with profile. Asymmetric (black) and Symmetric (red).

pump water from hot to cold side [113, 115, 116]. Variation in the TTN for the symmetric configuration is very small compared to the asymmetric configuration. This would indicate that water accumulation should be lower for the symmetric case which agrees well with the neutron imaging data.

The TTN plot can be used to describe the variation in the asymmetric configuration for the exhaust pressure tests as shown in Figure 5-9. It can be seen for both configurations that the 100|150 kPa exhaust pressure condition has the strongest preference towards the anode. The integrated value of the 100|150 kPa case for the symmetric configuration is only 65% of the integrated TTN value for the asymmetric condition. The lower saturation seen in the symmetric 100|150 kPa case when compared to the 150|150 kPa asymmetric case indicates that the land width has a strong influence on water storage. The lag seen in water accumulation for the asymmetric configuration in the 150|100 kPa case is due to the larger preference towards the cathode compared to the other two conditions. Water flux across the membrane is reduced in this condition requiring additional time to buildup water in the anode DM.

As has been shown in previous work, Ref [106], saturation has a strong influence on thermal conductivity and therefore, the temperature gradient based driving force for thermally driven transport. Liquid water increases apparent thermal conductivity as it reduces the low thermal conductivity air volume and improves contact between fibers. This increase in thermal conductivity can reduce peak temperature in the symmetric configuration by 8.1°C and the asymmetric by 8.4°C at 1.2 A/cm^2. Temperature profiles were calculated to determine wet TTN values using the saturation values from the
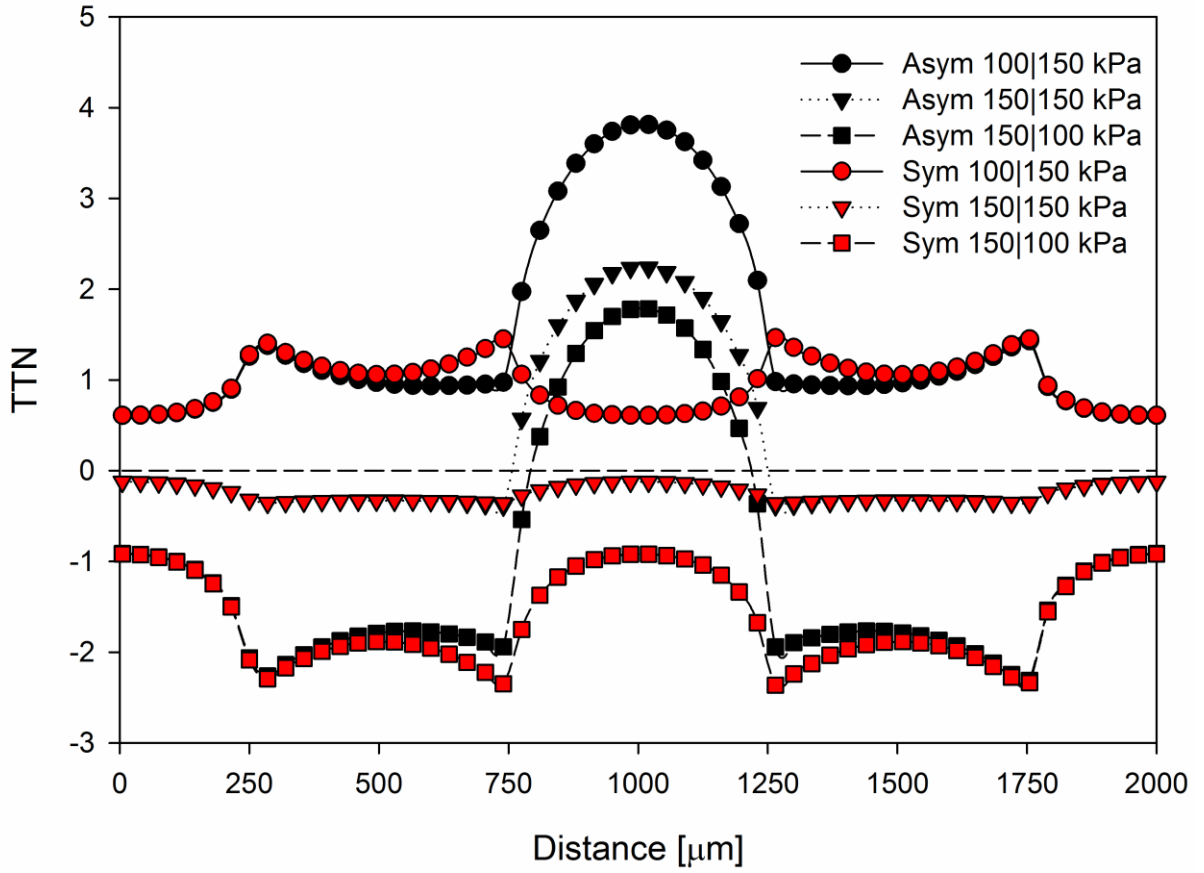
Figure 5-9: TTN plots as a function of pressure gradients at 60°C and 1.2 A/cm^2 along model domain length.

neutron images to determine wet thermal conductivity for both configurations. The TTN values for both configurations for wet conditions at 150|150 kPa is given in Figure 5-10. Large attenuation can be seen for maximum TTN due to the reduction in driving force and increased diffusion resistance due to liquid water accumulation. This shows that thermally driven water transport continuously changes during fuel cell operation with the highest driving force available when operating with no liquid water in the cell. The value of TTN will slowly decay as water builds up in the cell by reducing peak temperature and increasing diffusion resistance until a balance occurs in the cell. If a large transient draining event occurs during steady current density operation, the water balance can swing back towards the anode resulting in a rapid refilling of the anode DM. For full scale fuel cells operating in counter-flow, rapid anode water accumulation can occur close to the anode inlet as water buildup near the cathode exit would reduce water transport through the cathode and force it over to the anode.

Vapor carrying capacity of the gases increases significantly with increasing temperature so it is expected that the maximum TTN value would increase with operational temperature. A fourfold increase in TTN is seen in Figure 5-11 as temperature increases from 40°C to 80°C for the asymmetric configuration operating at the 150|150 kPa test case. The increase for the symmetric configuration towards cathode preference is more subdued due to the more identical anode and cathode temperature gradients. This shows that during cold startup, thermally driven transport would be a smaller percentage of the entire transport makeup but would become the dominant driving force at normal operational temperatures.

83
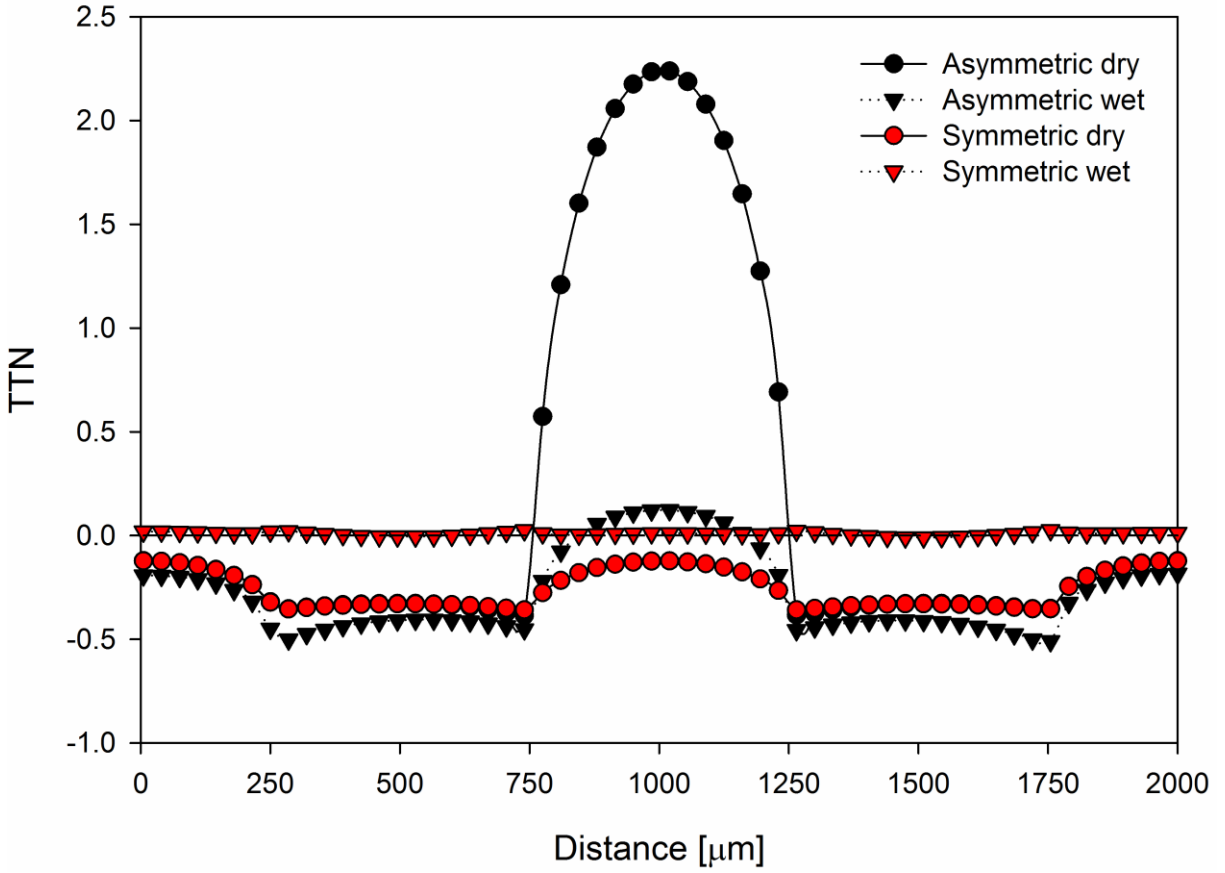
Figure 5-10: TTN plot for wet conditions at 60°C and 1.2 A/cm^2 for 150|150 kPa case showing a nearly 66% attenuation in maximum TTN influence.
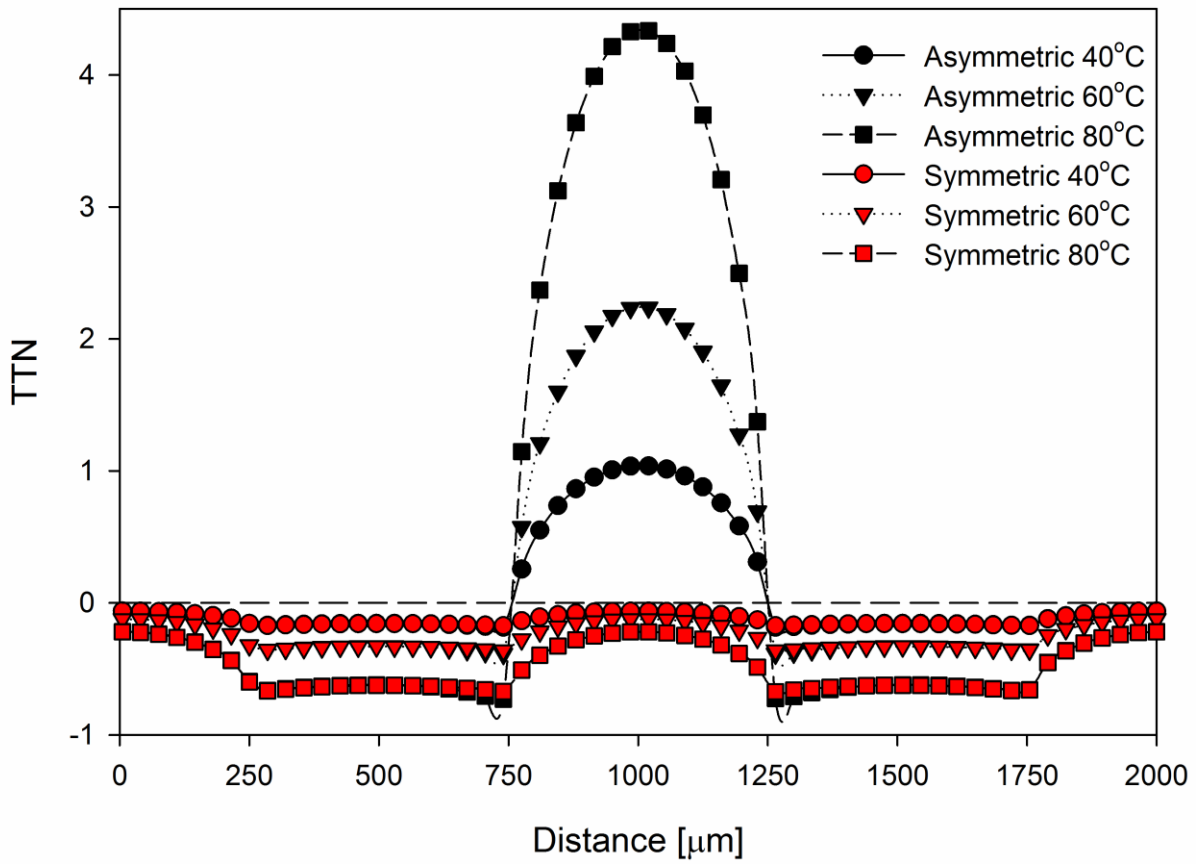
Figure 5-11: TTN as a function of operating temperature along the computational domain for 150|150 kPa test condition at 1.2 A/cm^2.

It is important to understand how current density affects thermally driven transport as this has an effect on operational voltage and heat generation within the cell. For the conditions in this work, saturation increases with increasing current density as shown in Figure 5-12. Little water buildup is seen at the lowest current densities due to the constant flow rates used causing stoichiometric ratios in the range of 20 for 0.1 A/cm^2. Figure 5-13 shows the TTN plots for both symmetric and asymmetric configurations for five current densities increasing from 0.1 A/cm^2 to 1.5 A/cm^2 at 60°C. It can be seen the operational current density has only a minor influence on the TTN value as the PCI flux is normalized with the water generation for the given current density. Due to the saturation remaining low at the 0.1 and 0.4 A/cm^2 current densities, the thermally driven flow remains constant for the duration of the test whereas the higher current densities would see a decrease in value with increasing saturation. Thermally driven flow can be the dominant transport mode across all current densities for the asymmetric configuration. This makes thermal design an important consideration even for fuel cells that operate only at low current densities.

5.4   Conclusions

In this work, the role of anode land width on cell water content has been investigated. By designing a cell with asymmetric flow field geometry with 1.5 mm anode lands and 0.5 mm cathode lands, large quantities of generated water can be driven to the anode. The large anode lands provide a large cooling area that pumps water to the anode from the cathode. In conjunction with the large flux of water to the anode, the large lands allow high levels of saturation (60%) to accumulate above the
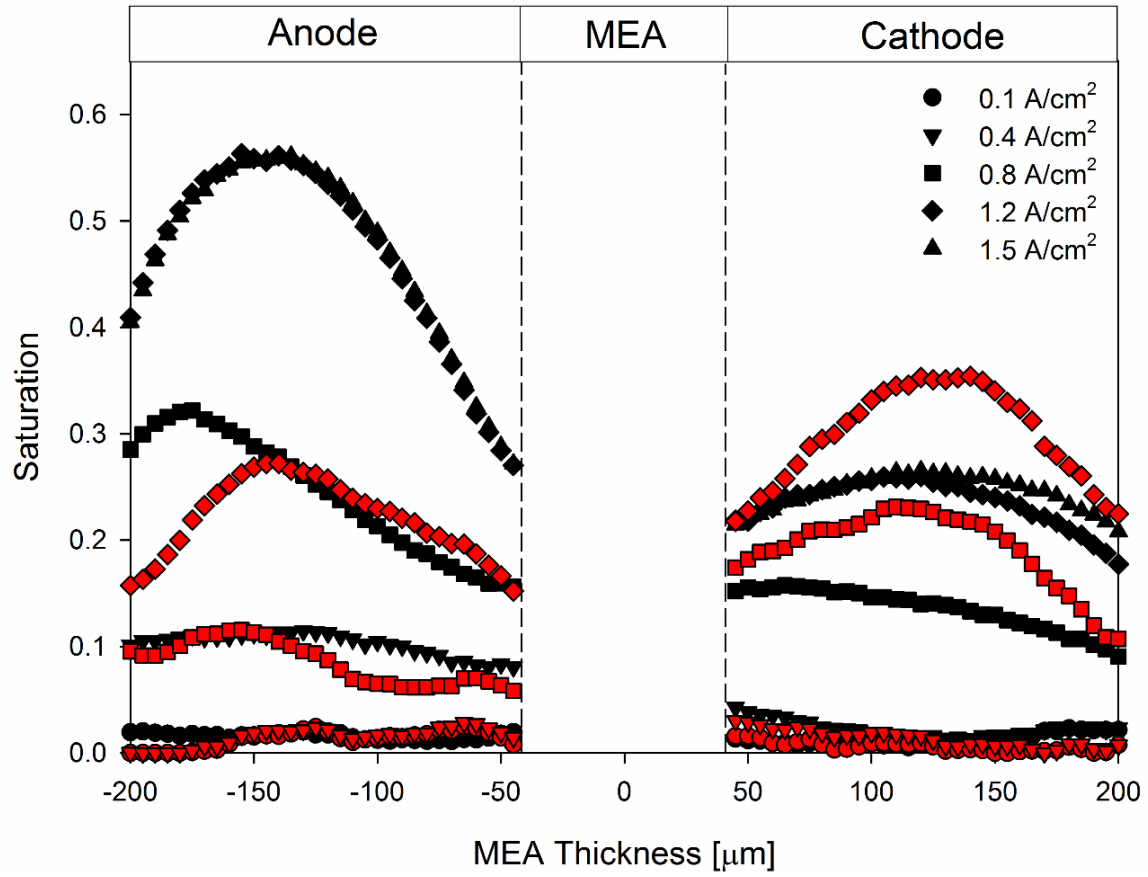
Figure 5-12: Saturation profiles as a function of current density at 60°C for the 150|150 kPa(a) test condition. Asymmetric configuration shown in black and the Symmetric configuration is shown in red.
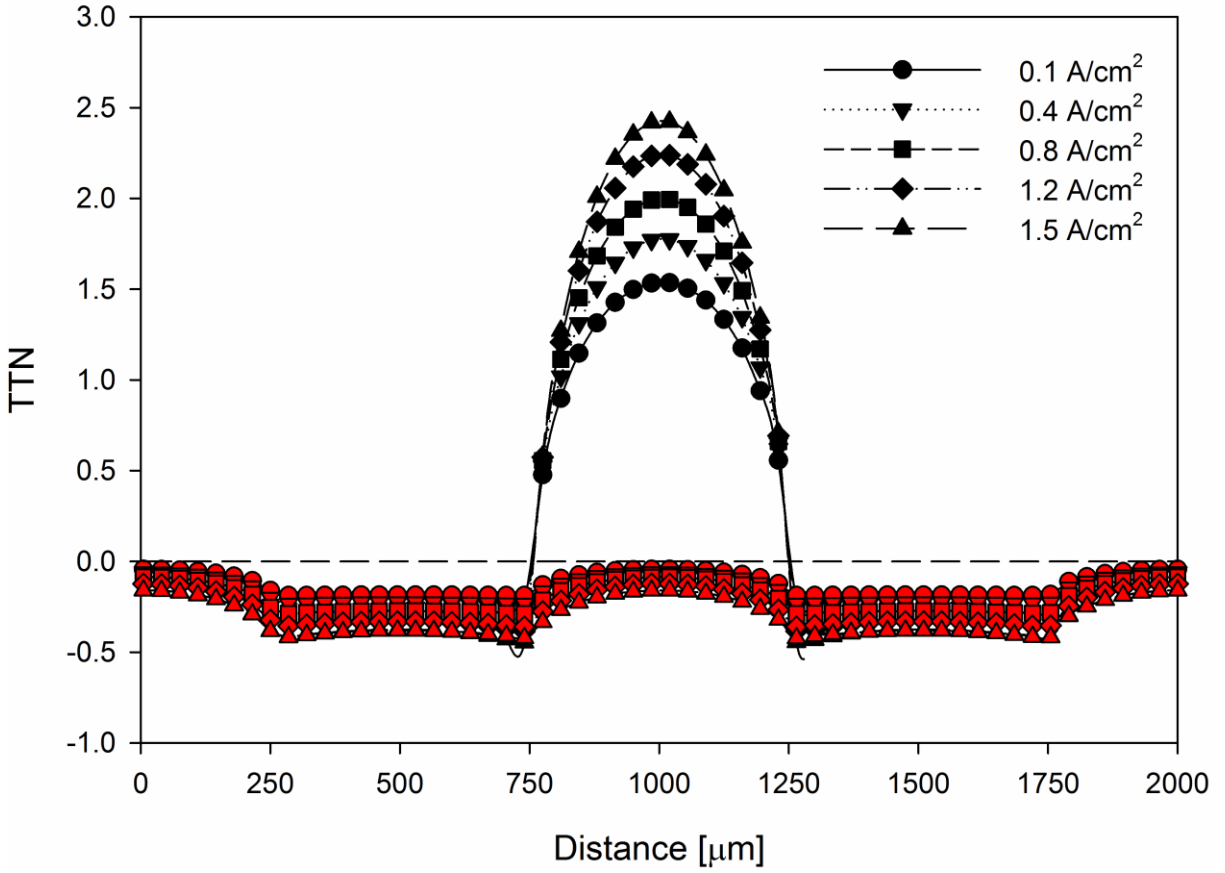
Figure 5-13: TTN plot as a function of current density at 60°C for the 150|150 kPa(a) test condition. Asymmetric configuration shown in black and the Symmetric configuration is shown in red.

lands compared to the maximum of 30% seen for the symmetric configuration with 0.5 mm anode and cathode lands.

Thermal transport is highly dependent on the saturation quantities in the diffusion media as liquid water has a strong influence on the apparent thermal conductivity of the DM. Liquid water increases the thermal conductivity of the DM allowing larger quantities of heat to be rejected from the cell which lowers the maximum driving force for thermally driven flow. In addition to the reduction in driving force, liquid water saturation also increases the diffusion resistance of the DM which also reduces the maximum thermally driven flux of water vapor.

Thermal design of fuel cell is critical to achieve the highest performance as temperature gradients have strong influence on water transport. With proper design of flow fields, coolant channels, and selection of materials, water transport can be optimized to drive water to desirable locations of the cell. This could be implemented to reduce the large anode water accumulation as seen in this work to improve shutdown purge performance and durability or used to increase water transport to prevent anode side membrane dry out at ultra-high current densities in high performance fuel cells.

CHAPTER 6: Anode Water Content Control Using High Tortuosity Diffusion Media

This chapter will be submitted for publication in The Journal of the Electrochemical Society with the following authors and title:

J.M. LaManna, J.P. Owejan, and M.M. Mench, "Development and validation of high tortuosity anode diffusion media for the reduction of anode water content in polymer electrolyte fuel cells"

My primary contribution is the work included in this chapter. Contributions from coauthors will be added prior to submission for publication.

6.1 Introduction

Accumulation of water in the anode has been linked to fuel starvation and current reversals that result in carbon corrosion of the DM and catalyst layers [117, 118]. Therefore, it is critical to develop methods to reduce anode water content to avoid flooding conditions that result in degradation. Development of novel diffusion media is an area of interest as materials typically used allow for multiple properties to be adjusted to tailor the transport characteristics of the layer. A seen in the previous chapters, significant water is transported across the membrane from the cathode to the anode. Increasing the diffusion resistance of the anode DM would restrict the transport of water to the anode. Several properties can be altered such as layer thickness, porosity, tortuosity, and wet proofing content. Increasing the layer thickness is

undesirable as this would increase overall stack thickness and reduce system volumetric efficiency. Reducing porosity would restrict water removal and increase sensitivity to flooding due to decreased available volume in the layer. This also occurs with increased PTFE content. So the ideal property to adjust is increasing tortuosity as added path length would increase diffusion resistance.

This chapter will focus on reducing anode water accumulation at high current densities using a newly developed high tortuosity diffusion medium. As shown in Chapter 5, large amounts of water can be pumped from the cathode to the anode resulting in anode flooding and transport limitations. The aim of the new DM is to increase diffusion resistance so as to limit the water transport to the anode. High resolution neutron imaging and a computational thermal transport model are used to determine the effectiveness of the new material. Results for the new material will be directly compared to the results from Chapter 3 and LaManna et al. [97].

6.2   Method of Approach

6.2.1 Cell Design

The fuel cell hardware used in this study was the same hardware previously used for neutron imaging in Chapter 3 and 5. For this work, two flow fields will be investigated, the asymmetric square flow field discussed in Chapters 3 and 5 and a new asymmetric triangular flow field. The new flow field was selected to help improve water removal with the triangular channels and the land width was reduced to push performance towards that of open foam flow fields. Dimensions for the two flow fields are given in Figure 6-1. Flow pattern for the new triangular flow field remain the triple serpentine pattern used in the baseline flow field.
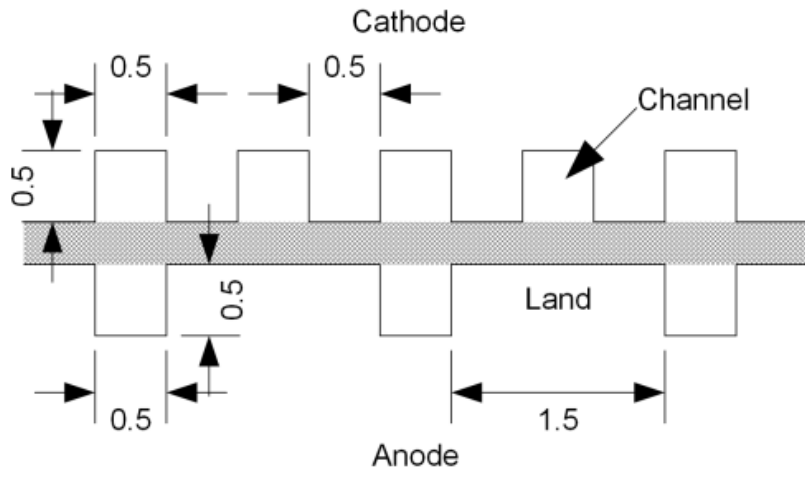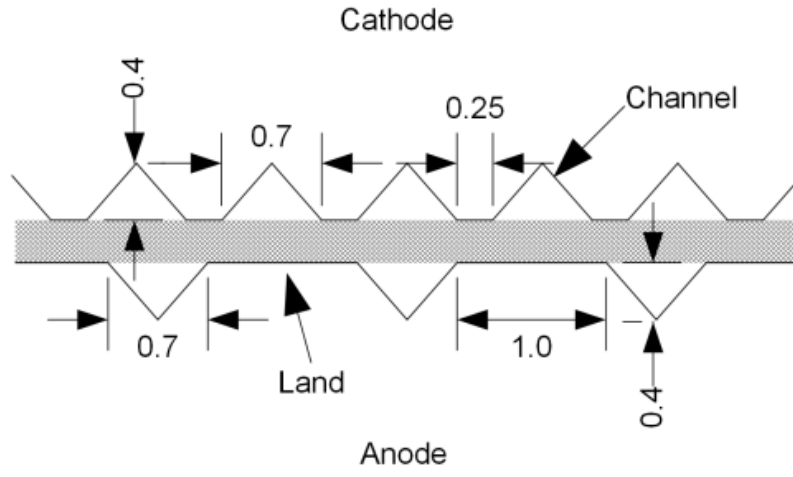
Figure 6-1: Channel dimensions for the baseline configuration (A) and the new autocompetitive configuration (B).

6.2.2 Materials

6.2.2.1 Baseline Configuration

The baseline configuration for this work represents the materials used in Chapter 3 and the asymmetric pitch, square channel flow field. Diffusion media used was the Mitsubishi Rayon Corporation (MRC) 105U with 5% wt. PTFE wet proofing. A W.L. Gore & Associates, Inc. Select Series 5720 18 μm membrane with 0.3 mg/cm^2 cathode loading and 0.05 mg/cm^2 anode loading were used.

6.2.2.2 Autocompetitive Configuration

The autocompetitive configuration is an advancement in design from the baseline configuration with the goals of reducing anode water accumulation, improving wet condition performance, and reducing manufacturing costs to facilitate fuel cell competitiveness with automotive internal combustion engines. The configuration consists of the asymmetric triangular channel flow pattern discussed above, MRC U105 cathode diffusion media, baseline configuration membrane and catalyst loadings, and a new experimental low cost anode diffusion media.

General Motors Fuel Cell Research Group has developed a new low cost, high tortuosity anode diffusion media with the aim to reduce anode water accumulation. This new layer is constructed with a mix of two fiber materials to reduce cost, graphite powder, and graphite platelets oriented in the in-plane direction. It is these platelets that increase the diffusion length through the layer. A SEM cross-sectional image of the new material is given in Figure 6-2 showing the in-plane orientation and stacking of the

graphite platelets. The figure also has a schematic representation of the increase in path length from standard materials to the new experimental material.

A comparison of relevant properties for the baseline and autocompetitive DM is given in Table 6-1. Values for the table were obtained from Refs. [119, 120] for thickness, PTFE content, and diffusion resistance, Ref. [106] for thermal conductivity, and Ref. [121] for porosimetry data.

6.2.3 Test Facility

Neutron imaging was conducted at the Neutron Imaging Facility at the NIST Center for Neutron Research in Gaithersburg, MD. The high resolution microchannel plate detector was used to acquire the images of the cell and has an effective resolution
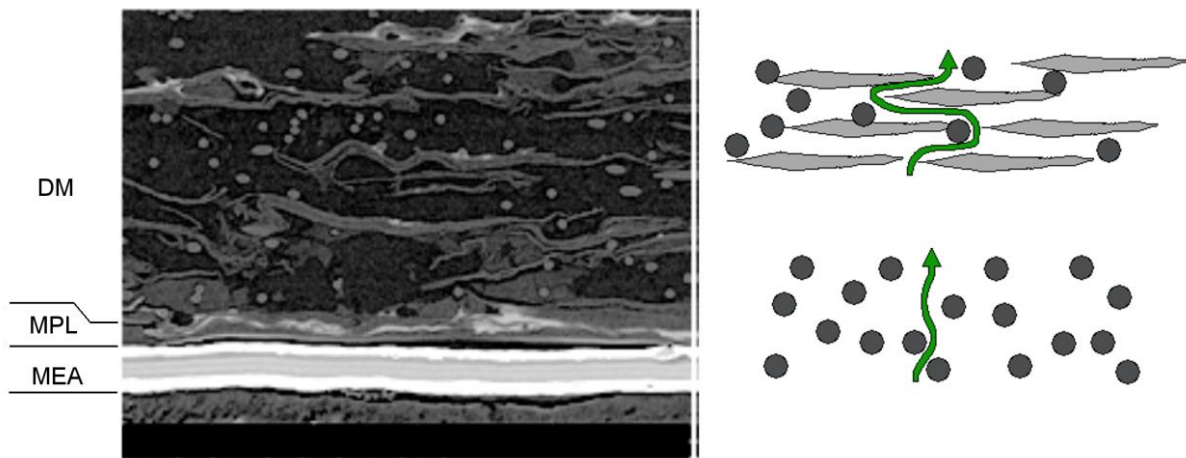
Figure 6-2: SEM cross-section of new high tortuosity anode material (left) and schematic representation of diffusion length of new material (top right) compared to standard diffusion media (bottom right).

Table 6-1: Baseline and Autocompetitive Diffusion Media Property Comparison

	MRC U105	High Tortuosity
Thickness [µm]	230	210
PTFE content [% wt.]	5	5
Uncompressed Porosity	0.77	0.81
Dry Thermal conductivity at 2 MPa compression [W/m-K]	0.18	0.9
D/Deff	4	20

of 15 µm. Additional details of the facility and the methodology for reduction of the images is available in Chapter 3 and ref [97].

6.2.4 Test Conditions

Test conditions chosen for this work are the same conditions used for baseline testing in Chapter 3 for direct comparison purposes. This test matrix was chosen to produce very wet conditions to provide rich data for model validation that would push the bounds of model predictive abilities. Testing was conducted at 40, 60, and 80℃ with constant flow rate at all conditions with an equivalent stoichiometric ratio of 2|2 at 1.2 A/cm^2. Current densities tested were 0.1, 0.4, 0.8, 1.2, and 1.5 A/cm^2 but only 1.5 A/cm^2 will be the focus of this work as high current densities represent the highest water generation and mass transport limitations. Exhaust pressure was varied to provide hydraulically driven flow across the membrane with pressure combinations of 100|150 kPa, 150|150 kPa, and 150|100 kPa [anode|cathode]. Inlet relative humidity was varied

to produce concentration gradients across the membrane with inlet relative humidities of 95|95, 95|50, 50|95, and 50|50 %RH [anode|cathode]. During pressure testing humidity was held constant at 95|95 %RH and during humidity testing pressure was held constant at 150|150 kPa.

6.2.5 Modeling

The thermal transport model used in the chapter has been developed previously in Chapter 5 which uses COMSOL and MATLAB to determine the thermal influence on water transport and balance in a cell. Temperature gradients are determined across anode and cathode DM along the entire computational domain and are used to calculate the Phase-Change-Induced (PCI) flow across each half of the cell. The Thermal Transport Number (TTN) is used to determine the maximum thermal driving force across the cell and is given in Equation 6.1 below.

$$TTN = \left(\frac{J_{PCI}}{J_{gen}}\right)_{anode} - \left(\frac{J_{PCI}}{J_{gen}}\right)_{cathode}$$ (6.1)

The full details of the Thermal Transport Number are given in Chapter 5.

6.3   Results and Discussion

6.3.1 Neutron Imaging

Through-plane saturation was determined with neutron imaging for both the baseline and autocompetitive configurations. Testing begun with the exhaust pressure

96

tests at 40°C. The highest current density that would run for all conditions for the baseline configuration was 0.8 A/cm^2 due to poor performance with the 100|150 kPa condition. All current densities were achievable for the autocompetitive configuration. Since little variation in water saturation was seen at the higher current densities from the 0.8 A/cm^2 case, it was chosen for the comparison at this temperature. As has been shown in Chapter 3, the baseline material shows significant variation and accumulation of anode water content depending on the operating condition as shown in Figure 6-3. The 100|150 kPa condition that exhibited poor performance at higher current densities shows the highest saturation for the anode at ~60%. Anode water accumulation and variability is greatly reduced with the use of the high tortuosity diffusion media in the AC configuration as seen in Figure 6-3. The introduction of the diffusion resistance limits the amount of water that can transport across the membrane from the cathode to the anode. Cathode saturation profiles follow similar trends as expected for both configurations since the same material is used for both. Small variation in the profiles can be attributed to the reduction in land width and increase in channel width from baseline to autocompetitive configurations.

Similar trends are seen with improved anode water content in the autocompetitive configuration in Figure 6-4 when the temperature was increased from 40 to 60°C. At this temperature, a current density of 1.5 A/cm^2 was chosen despite the fact that the baseline 100|150 kPa did not run due to poor performance because significant variation in water content occurred when changing from the lower current densities to the highest. The variation in anode water content was reduced as the two cases that could run approached the maximum critical saturation level of 60% due to
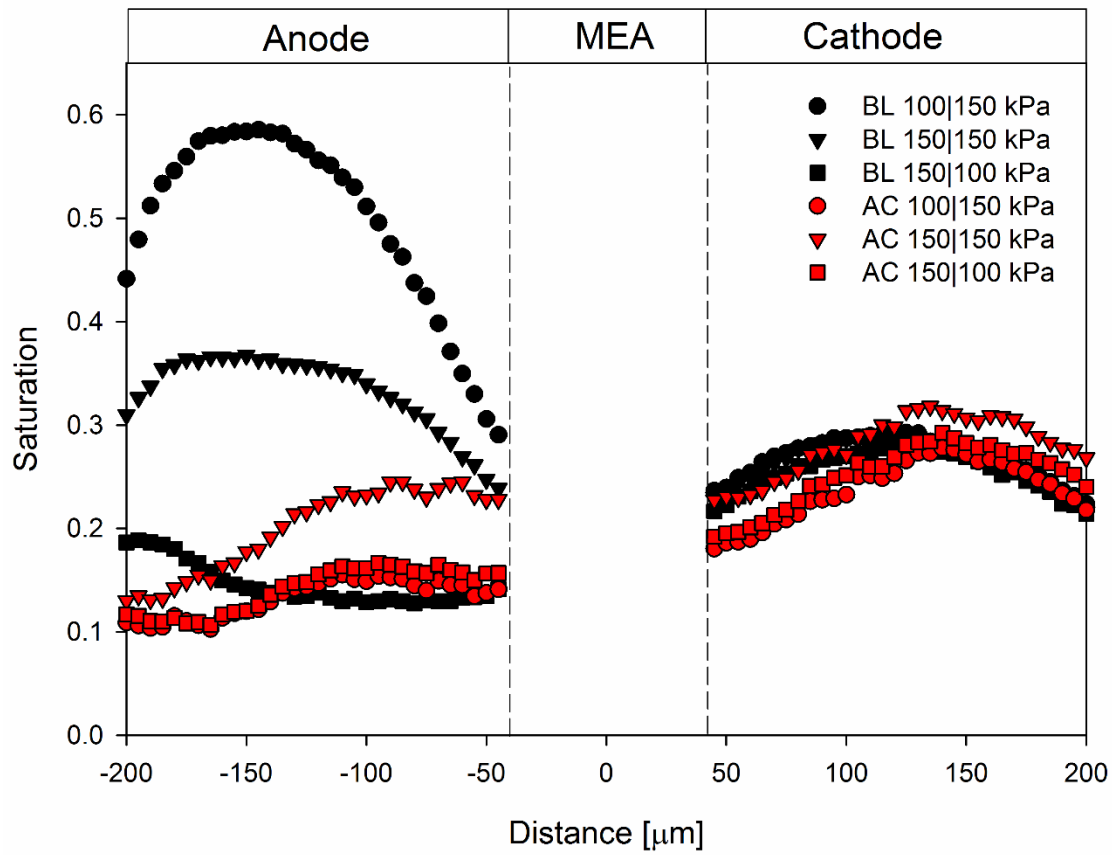
Figure 6-3: Saturation profiles for 0.8 A/cm^2 at 40°C test conditions for baseline and autocompetitive configurations. Test conditions: 95|95% inlet RH, constant gas flow rates with equivalent 2|2 stoichiometry at 1.2 A/cm^2.

the nearly double water generation at 1.5 A/cm^2 and larger heat generation for thermal transport. Cathode saturation profiles follow similar trends for both configurations with variation primarily due to the reduction in land width in the autocompetitive configuration.

In addition to the exhaust pressure gradients for hydraulically driven flow, relative humidity was adjusted at 60°C to influence concentration driven flow. The baseline configuration exhibits large anode water accumulation for the two cases with anode inlet relative humidity of 95% as shown in Figure 6-5. Maximum saturation for the baseline approaches 60% as seen for the two previous pressure conditions while the cathode maximum is around 30%. The autocompetitive configuration displays effective reduction in anode water content with maximum saturation levels of ~20% for all cases which is comparable to the low anode humidity cases in the baseline configuration. Cathode saturation is invariant for both configurations with all test conditions falling in close proximity to each other. The small offset in cathode saturation for the high and low anode inlet relative humidity cases indicate that cathode transport load increases when back diffusion is limited due to anode flooding. This agrees well with what is seen in Chapter 5 with the reduction in thermal transport with lower temperatures from saturation driven thermal conductivity increases.

Increasing temperature to 80°C greatly reduces the amount of liquid water for both configurations due to the increase in the vapor carrying capacities of the gas streams. Baseline shows minor water accumulation in the anode with maximum saturation approaching 20% for exhaust pressure cases and relative humidity cases, Figure 6-6 and Figure 6-7 respectively. The autocompetitive configuration had little to no

99
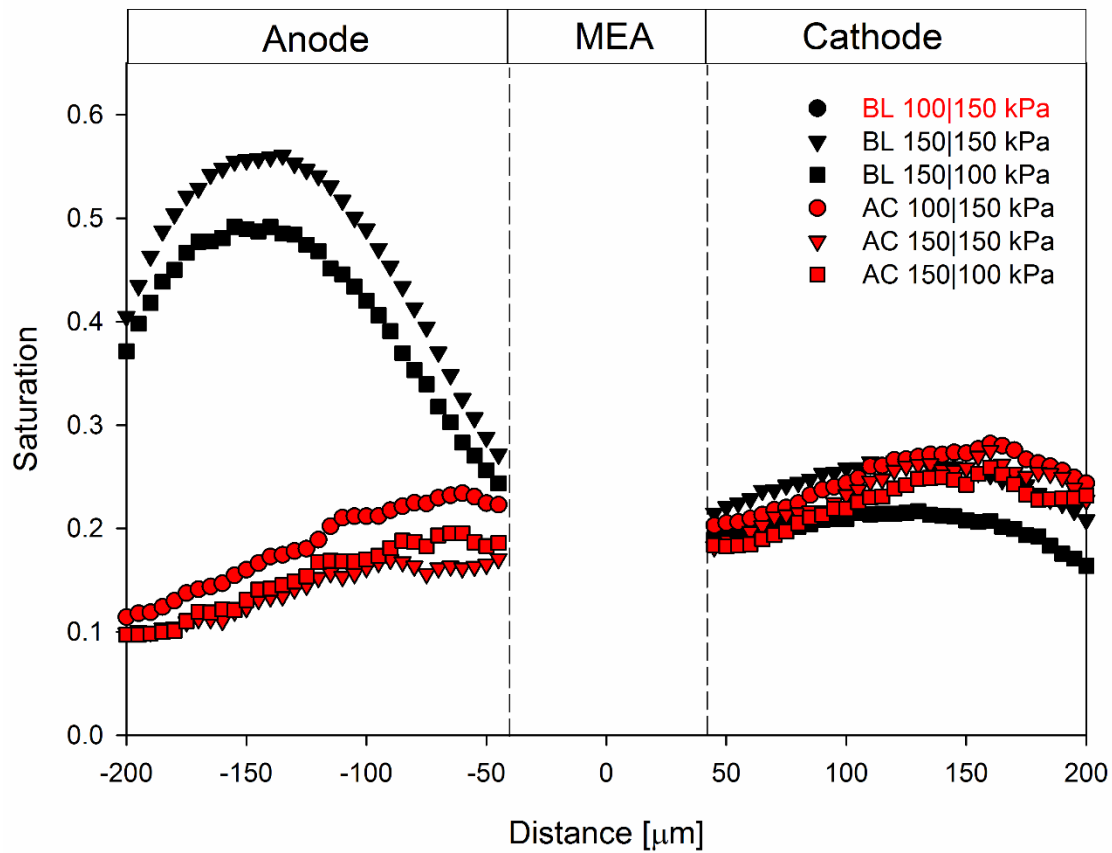
Figure 6-4: Saturation profiles for exhaust pressure conditions at 60°C operating at 1.5 A/cm^2. Baseline 100|150 kPa condition is not shown due to failure to run condition. Test conditions: 95|95% inlet RH, constant gas flow rates with equivalent 2|2 stoichiometry at 1.2 A/cm^2.
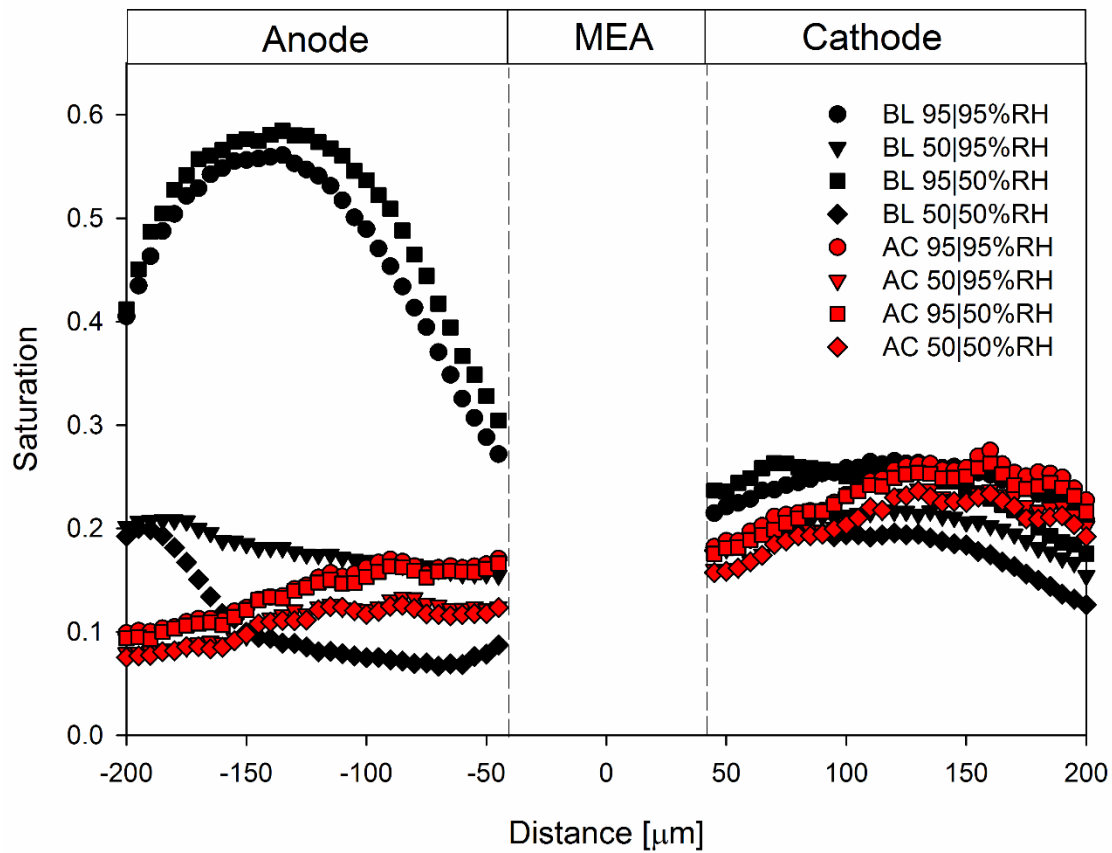
Figure 6-5: Saturation profiles for relative humidity conditions at 60°C operating at 1.5 A/cm^2. Test conditions: 95|95% inlet RH, constant gas flow rates with equivalent 2|2 stoichiometry at 1.2 A/cm^2.

buildup of liquid water in the cell. Average test voltages for all conditions shown are given in Table 6-2.

6.3.2 Water Balance Measurements

Water balance measurements were performed to determine if the reduction in water content for the autocompetitive configuration was due to a reduction in water storage or a restriction in transport from the cathode to the anode. Figure 6-8 shows that a larger percentage of generated water is removed via the cathode for the autocompetitive compared to the baseline configuration. This shows that the reduction in water content is due to a shift in water balance with the increased transport restrictions on the anode. The higher porosity of the autocompetitive DM would indicate that a higher storage quantity should be possible compared to baseline but due to the low flux of water to the anode less water is accumulated.

6.3.3 Thermal Transport Influence on Water Balance

The Autocompetitive configuration consists of three primary changes from the Baseline configuration which includes flow field geometry, anode diffusion media thermal conductivity, and anode diffusion media transport resistance. Therefore, each change will be independently investigated with TTN to understand how these changes influence the overall cell water balance. Beginning with flow field effects, the temperature profiles for the two flow field configurations were modeled with constant baseline material properties, 0.18|0.18 W/m-K [anode|cathode] thermal conductivity and
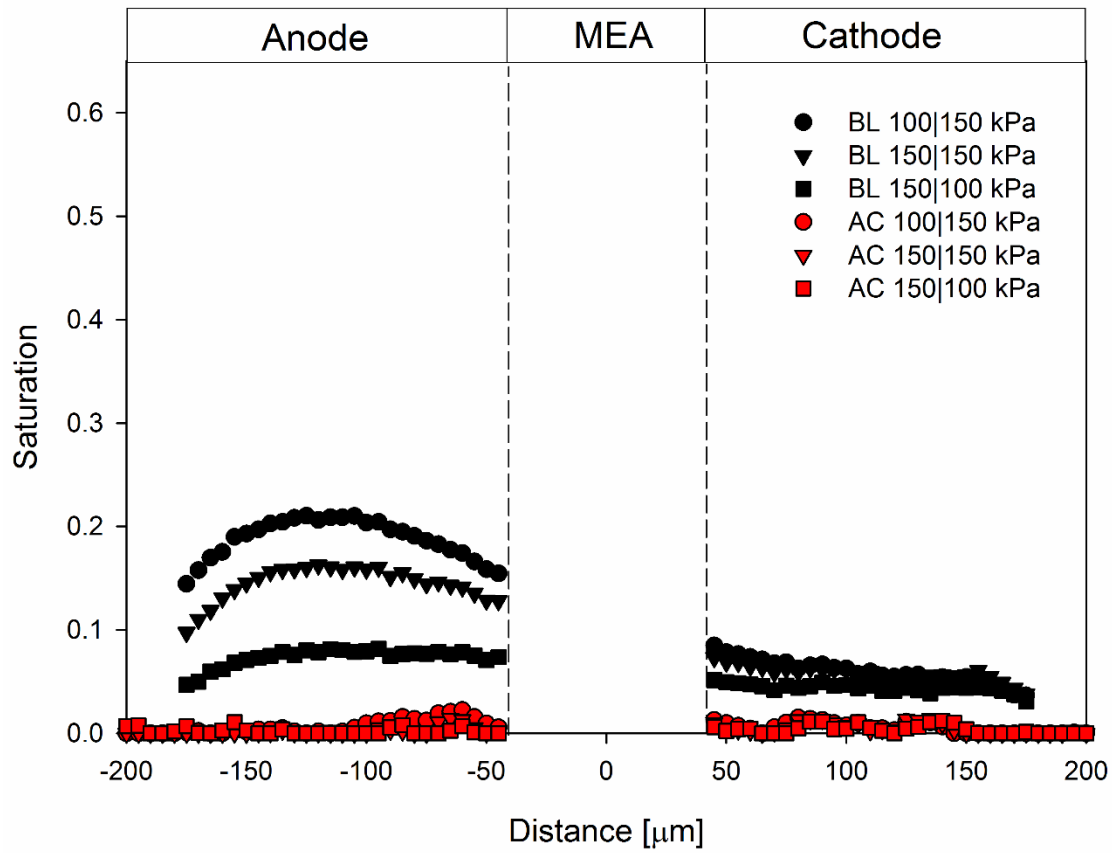
Figure 6-6: Saturation Profiles for exhaust pressure conditions at 80°C operating at 1.5 A/cm^2. Test conditions: 95|95% inlet RH, constant gas flow rates with equivalent 2|2 stoichiometry at 1.2 A/cm^2.
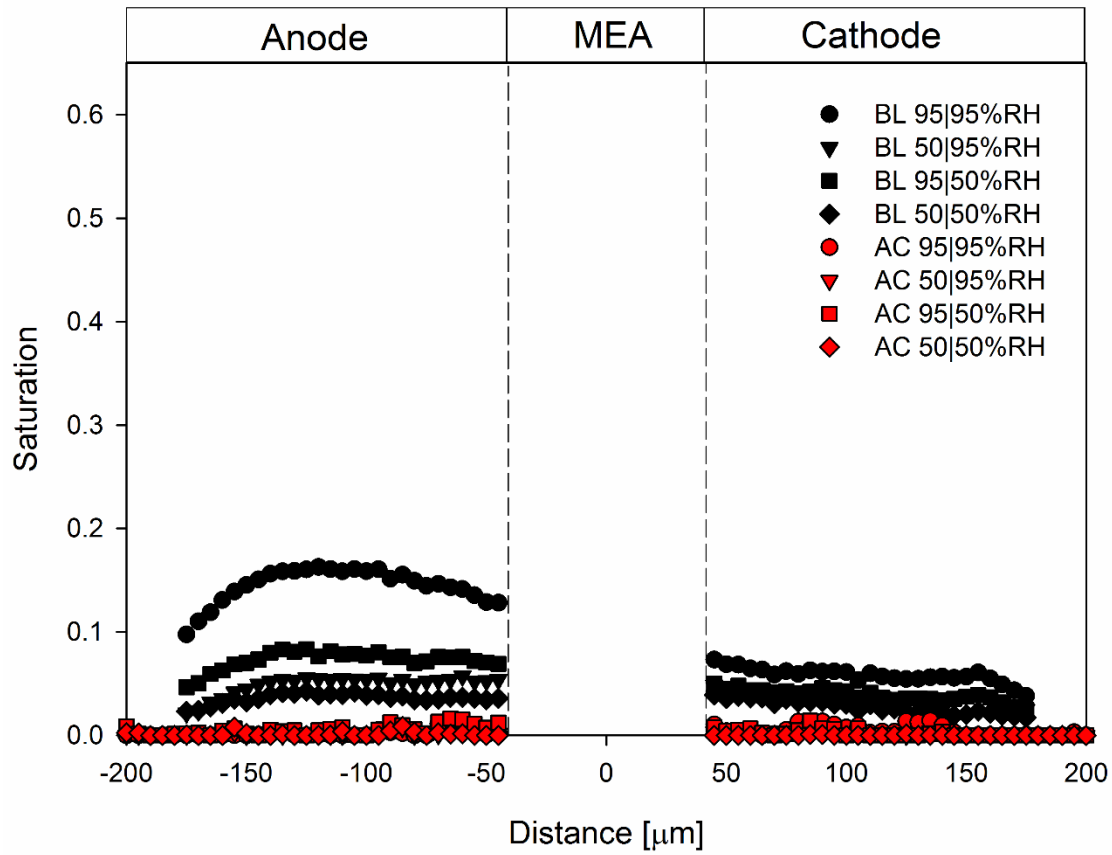
Figure 6-7: Saturation profiles for relative humidity conditions at 80°C operating at 1.5 A/cm^2. Test conditions: 95|95% inlet RH, constant gas flow rates with equivalent 2|2 stoichiometry at 1.2 A/cm^2.

Table 6-2: Operational voltages for saturation profiles.

Condition		Voltage [V]	
		Baseline	Autocompetitive
40°C	100|150 kPa, 95|95 %RH, 0.8 A cm^{-2}	0.608	0.646
	150|150 kPa, 95|95 %RH, 0.8 A cm^{-2}	0.690	0.637
	150|100 kPa, 95|95 %RH, 0.8 A cm^{-2}	0.701	0.657
60°C	100|150 kPa, 95|95 %RH, 1.5 A cm^{-2}	N/A	0.440
	150|150 kPa, 95|95 %RH, 1.5 A cm^{-2}	0.580	0.498
	150|100 kPa, 95|95 %RH, 1.5 A cm^{-2}	0.530	0.443
	50|95 %RH, 150|150 kPa, 1.5 A cm^{-2}	0.595	0.494
	95|50 %RH, 150|150 kPa, 1.5 A cm^{-2}	0.583	0.490
	50|50 %RH, 150|150 kPa, 1.5 A cm^{-2}	0.598	0.487
80°C	100|150 kPa, 95|95 %RH, 1.5 A cm^{-2}	0.496	0.521
	150|150 kPa, 95|95 %RH, 1.5 A cm^{-2}	0.508	0.517
	150|100 kPa, 95|95 %RH, 1.5 A cm^{-2}	0.383	0.468
	50|95 %RH, 150|150 kPa, 1.5 A cm^{-2}	0.670	0.500
	95|50 %RH, 150|150 kPa, 1.5 A cm^{-2}	0.665	0.480
	50|50 %RH, 150|150 kPa, 1.5 A cm^{-2}	0.619	0.475
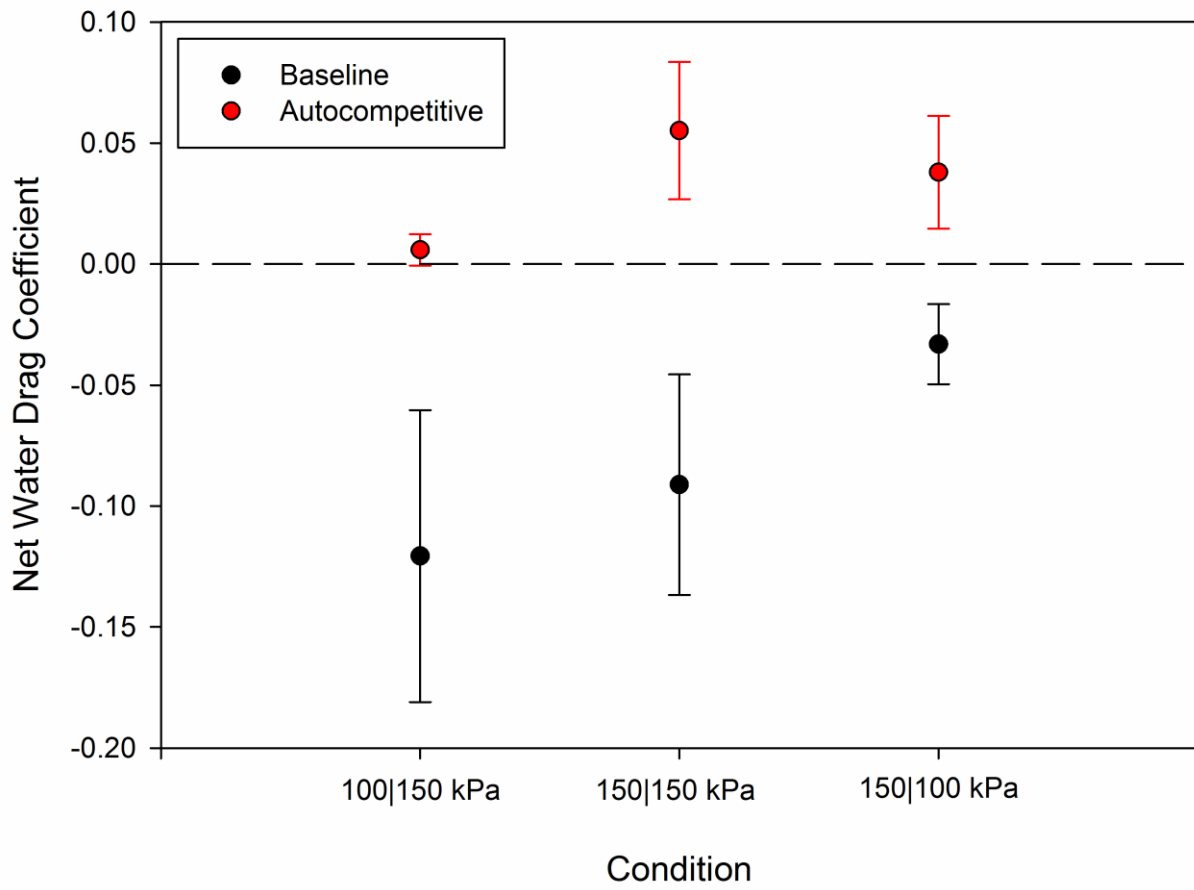
Figure 6-8: Net water drag coefficients for exhaust pressure test conditions at 60°C.

1.5|1.5 tortuosity. The temperature profiles were then used to calculate the TTN for both cases along the length of the computational domain. In Figure 6-9, it can be seen that the triangular 1.7|0.95 mm pitch channels used in the autocompetitive configuration results in a stronger maximum driving force towards the anode compared to the channels in the baseline configuration. With the standard baseline MRC DM on the anode with the autocompetitive flow field it would be expected to see more water buildup and sensitivity than what is seen with the full baseline case.

Next, the influence of thermal conductivity will be investigated since the high tortuosity DM is nearly 5 times more conductive than the baseline DM. In this case, simulations were conducted using the baseline 2|1 mm pitch flow field and 1.5|1.5 tortuosity. The low 0.18|0.18 W/m-K thermal conductivity represents the values for the standard baseline case while the high 0.9|0.18 W/m-k thermal conductivity represents the values for the autocompetitive configuration. In Figure 6-10 it can be seen that thermal conductivity does not have as strong of an influence on the transport as channel layout. The high conductivity of the high tortuosity anode DM reduces the peak temperature from 74.2°C to 65.9°C which has a significant effect on concentration change across the DM. This reduces the maximum PCI flux which is evident by the quartering of the peak TTN from low conductivity to high conductivity configuration. With the reduction in PCI flux due to lower temperature the thermal based water balance tends to a zero or balance value. This implies that higher conductivity DM would see a reduction in peak anode water content seen in the neutron images due to the lower temperature gradients inducing less flux across the DM.
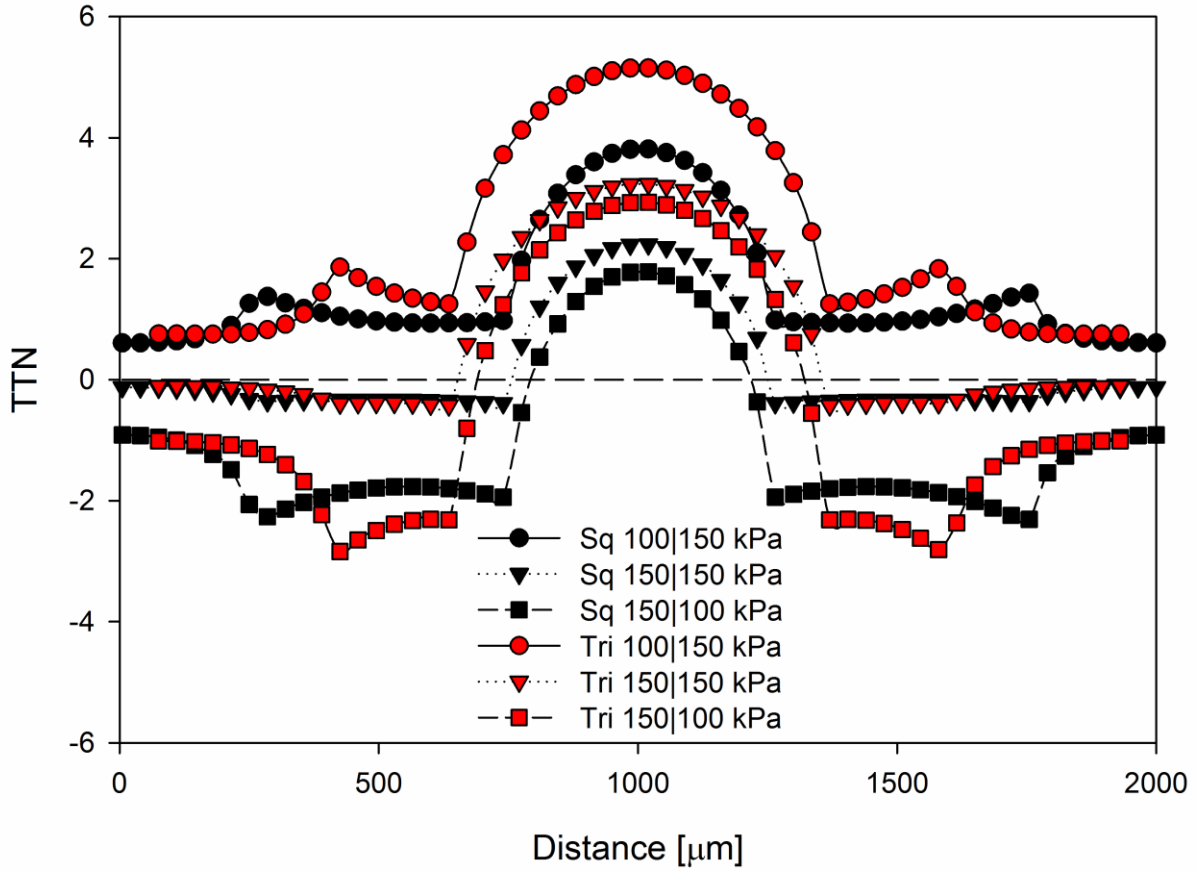
Figure 6-9: Flow field influence, baseline square channel 2|1 mm [anode|cathode] pitch flow field versus autocompetitive triangular channel 1.7|0.95 mm pitch flow field. All DM thermal conductivity is set at 0.18 W/m-K and all DM tortuosity set to 1.5.
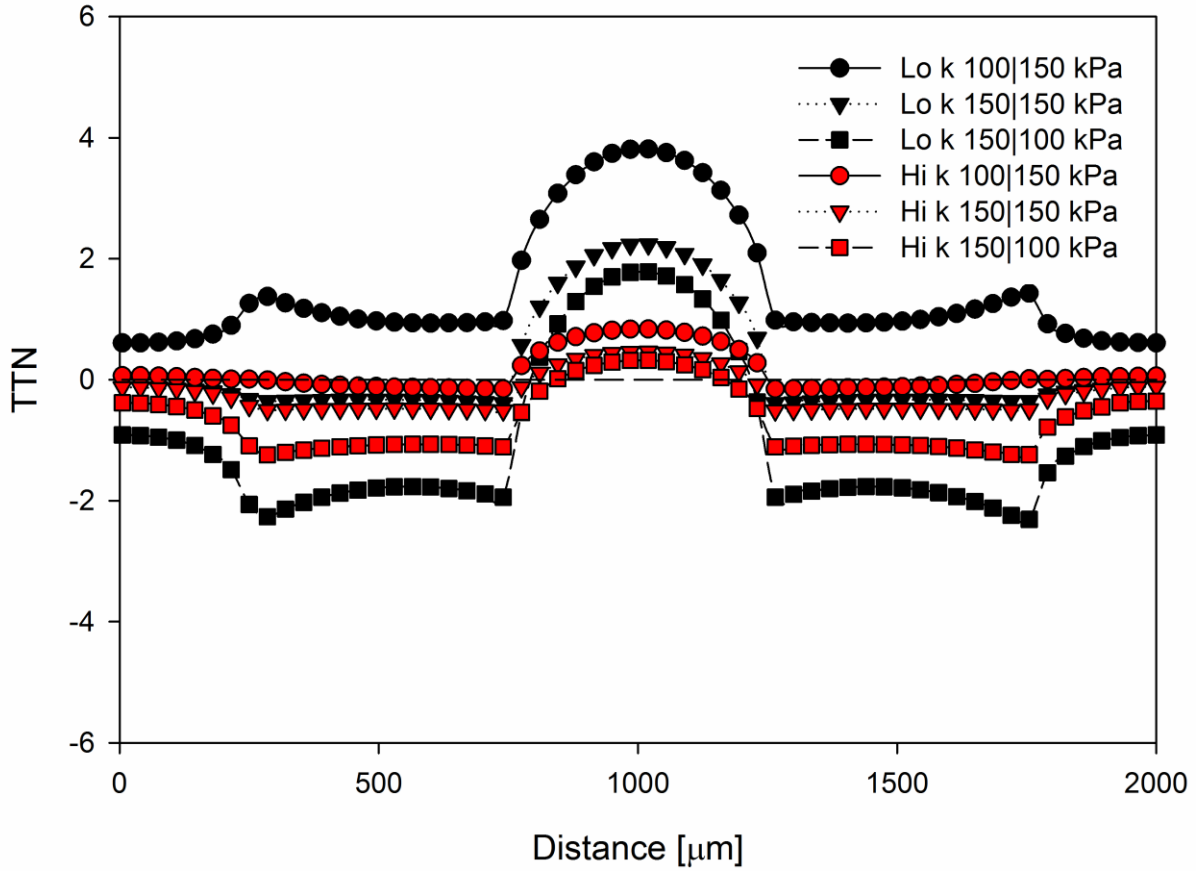
Figure 6-10: Thermal conductivity influence, baseline 0.18|0.18 W/m-k [anode|cathode] DM thermal conductivity versus autocompetitive 0.9|0.18 W/m-K DM thermal conductivity. Flow field held constant to baseline 2|1 mm pitch square channels and tortuosity held constant at baseline 1.5.

The last property adjusted in the new experimental material is tortuosity. The baseline MRC has an assumed tortuosity of 1.5 while the high tortuosity DM has a value of 7.75 based on Bruggeman correction. The simulations were run with the baseline asymmetric square channels and MRC 0.18|0.18 W/m-K thermal conductivity for both cases with 1.5|1.5 [anode|cathode] tortuosity for the baseline case and 7.75|1.5 tortuosity for the autocompetitive case. Thermal transport is significantly affected by the increased anode diffusion resistance as shown in Figure 6-11. All three pressure conditions for the high tortuosity case are less than zero for all nodes along the domain. Due to the resistance of the anode, the cathode DM must remove the majority of product water whereas in the baseline case 50% or more of the product water can be removed through the anode.

Combining all three changes from baseline together gives the total expected thermal transport for the autocompetitive configuration. All nodes for the autocompetitive configuration are below zero in Figure 6-12 specifying a preference for cathode removal of generated water. This agrees well with the reduction in water content seen in the saturation profiles from neutron imaging. Comparing the total case to the three individual cases, it can be seen that the changes in flow field and the thermal gradients within the cell drive water to the anode. It is the increase in diffusion resistance that is responsible for zero preference towards the anode. The interaction of the flow field design and thermal conductivity attenuate the strong cathode preference of the diffusion resistance. This will produce a more even flux of water from the cathode catalyst layer to the flow field and reduce the possibility of anode dry out. The reduction in maximum cathode preference by over 50% between just diffusion resistance and total

110
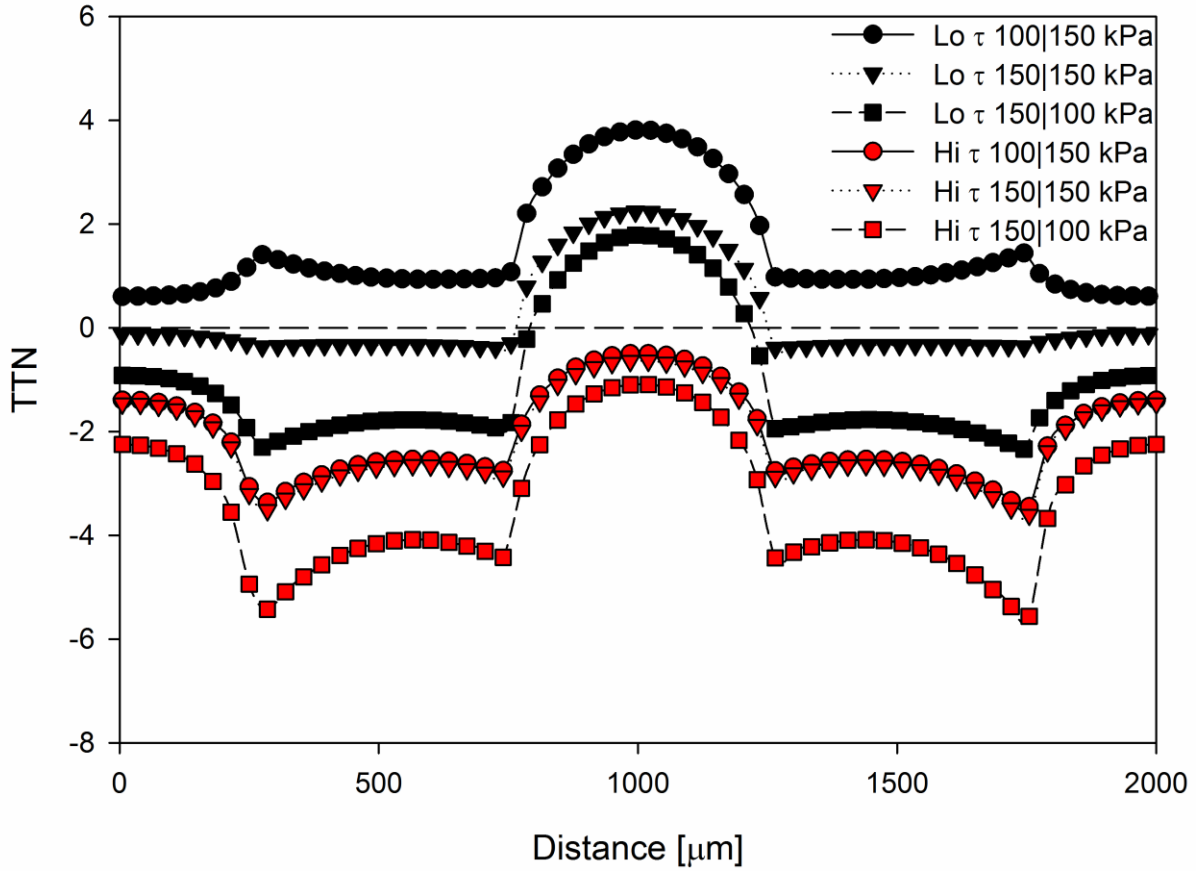
Figure 6-11: Tortuosity influence, baseline 1.5|1.5 [anode|cathode] tortuosity versus autocompetitive 7.75|1.5 tortuosity. Flow field held constant to baseline 2|1 mm pitch square channels and thermal conductivity held constant to baseline 0.18|0.18 W/m-k.
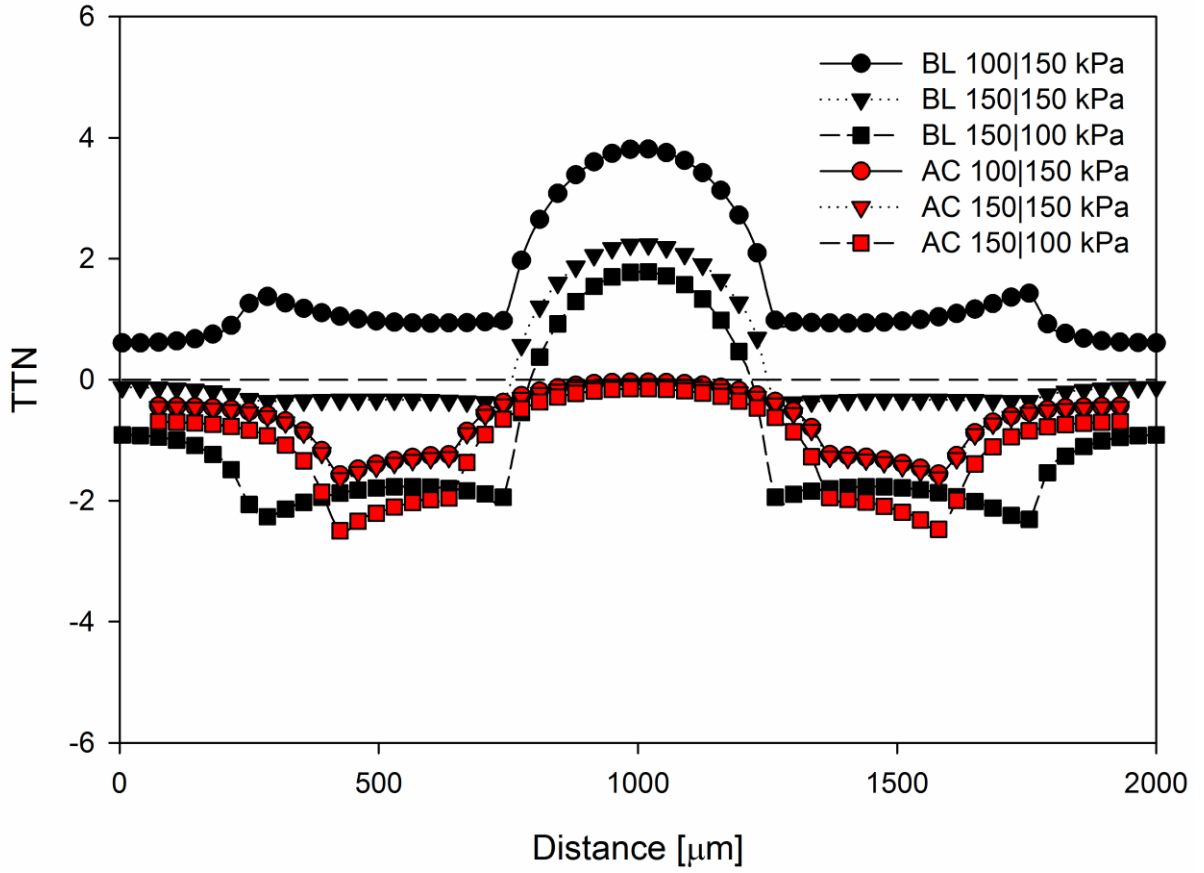
Figure 6-12: Baseline versus autocompetitive TTN plot with combined flow field, thermal conductivity, and tortuosity influences.

combined influence reduces the strong flux regions that could pull over 5 times the water generation lowers the risk of anode side membrane dry out. Increased membrane hydration for the autocompetitive configuration over the baseline configuration from high frequency resistance data from Ref. [120] strengthens the reduction in anode dry out risk.

6.3.4 *Influence of Saturation on Thermal Transport*

In Chapter 4 and Ref. [106] it was shown that saturation has a strong influence on thermal conductivity and baseline temperature distribution with a drop in peak temperature from 74.2 to 66.1°C, a change of 8.1°C. It is important to determine how saturation affects the new autocompetitive configuration. Neutron images are used to determine saturated thermal conductivity using the method described in Chapter 4. Simulations were run with dry and the calculated wet thermal conductivity for both configurations yielding the temperature distributions in Figure 6-13. The reduction in peak temperature for the autocompetitive configuration was significantly less than the baseline configuration with a reduction from 68.1 to 65.2°C, a change of 2.9°C. This is primarily due to the lower increase in thermal conductivity with saturation for the high tortuosity diffusion media and the reduced peak temperature from the higher dry thermal conductivity.

Thermal Transport Number values for each case was calculated to compare the effects of saturation on thermal transport. Figure 6-14 shows that the TTN for autocompetitive configuration is minimally sensitive to saturation while baseline configuration has a large dampening of thermal transport with increasing saturation.

113
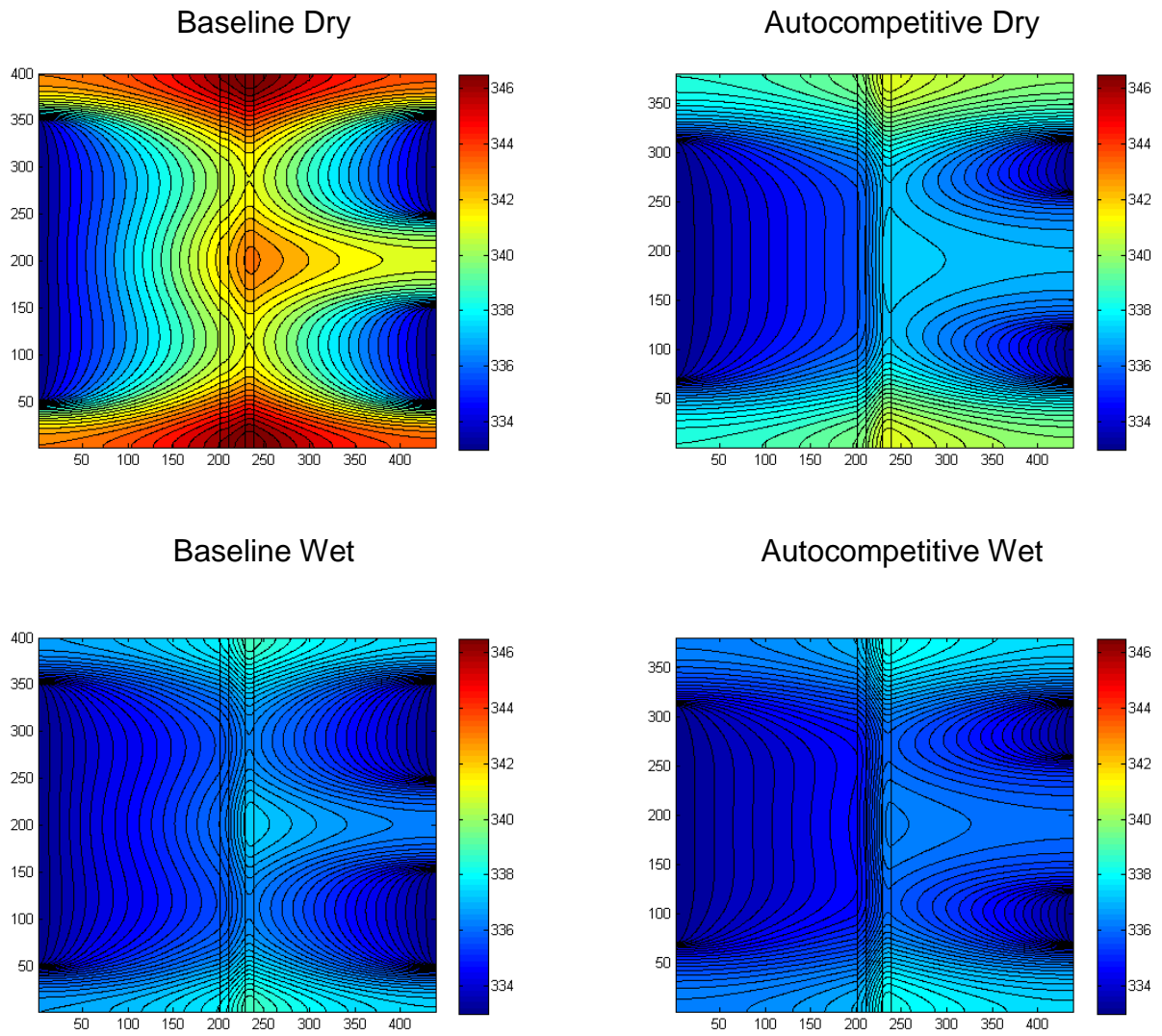
Figure 6-13: Temperature distributions for baseline and autocompetitive configurations in dry and wet conditions.
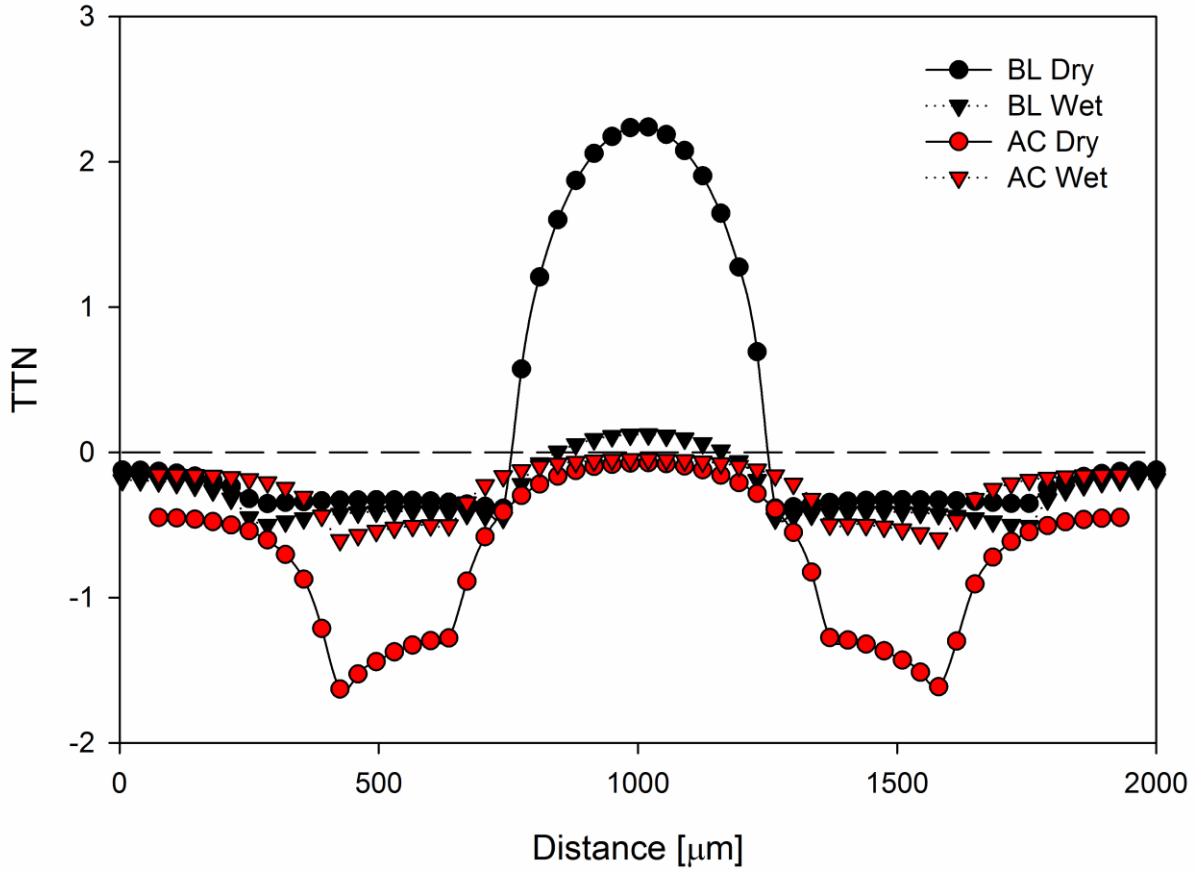
Figure 6-14: Dry and wet comparison of TTN plots for baseline and autocompetitive configurations.

This shows that the autocompetitive configuration would produce a more consistent and steady state thermal transport force during operation whereas the baseline configuration would constantly change with changing saturation levels. A more stable transport mode could result in improved performance with less voltage oscillations.

6.4 Conclusions

In this chapter, a new channel and diffusion media configuration has been proposed to increase the efficiency, operational life, and cost competitiveness with automotive internal combustion engines. A low cost, high tortuosity anode diffusion media was developed to decrease anode water and improve wet condition performance. The new autocompetitive configuration significantly reduced anode water accumulation seen in the baseline configuration. Peak anode saturation was reduced from 60% to less than 25%.

A thermal transport analysis was performed to determine how the change in properties from baseline to autocompetitive configurations influenced the change in water balance. The new autocompetitive configuration had three primary changes from the baseline configuration, flow field, anode DM thermal conductivity, and anode DM diffusion resistance. It was found that the flow field modifications would increase water content while the reduction in thermal conductivity and increase in diffusion would each reduce water transport to the anode. The increase in diffusion resistance was found to be the primary factor in restricting back diffusion and water transport and accumulation in the anode.

Altering properties of diffusion media has been found to have strong influences on water management. Although the material that is presented here has shown promise in increasing the performance of a fuel cell, it still requires optimization in all properties such as mechanical strength and electrical and thermal conductivity to better match the cathode material.

CHAPTER 7: Operational Age Changes to Water Balance and Material Properties in Polymer Electrolyte Fuel Cells

This chapter will be submitted for publication in The Journal of the Electrochemical Society with the following authors and title:

J. M. LaManna, A. M. Pezeshki, G. M. Veith, and M. M. Mench, "Changes to water balance and material properties with operational age in polymer electrolyte fuel cells"

My primary contribution to this work is the neutron imaging, thermal conductivity measurements, thermal transport modeling, and interpretation of XPS data to fuel cell environment. Pezeshki and Veith were responsible for the collection and reduction of the XPS data.

7.1   Introduction

Degradation and changes with performance are important issues for automotive fuel cells as current DOE targets expect operational lifetimes of 5,000 hours [122]. Multiple modes of degradation occur within a fuel cell which affect each layer and component within the cell. These modes include catalyst agglomeration, migration, and dissolution [123-125], carbon corrosion of catalyst support and diffusion media [109, 110, 126, 127], membrane chemical and mechanical breakdown [128, 129], thermal cycling stress on carbon supports [130], and oxidation of flow fields [131, 132]. Thermal conductivity of aged materials has not been investigated extensively in the literature

with a paper by Burheim et al. [133] investigating the effects of artificial aging on thermal conductivity.

This chapter will focus on the effects of operational age on thermal conductivity, water storage, and thermally driven flow with materials that have operating in full scale stacks from fuel cell vehicles. Neutron imaging will be used to determine the water stored in the cell for the standard test matrix. Thermal conductivity will be measured for aged samples and compared to virgin material to ascertain the influence on thermally driven transport and its role on cell water balance.

7.2   Method of Approach

7.2.1 Cell Design and Materials

This work uses the 4.8 cm^2 cell developed for high resolution neutron imaging that was discussed in Chapter 3. Liquid cooling is used for precise control of thermal boundary conditions control with a water circulator with accuracy of ±0.2°C. The flow field used for this analysis was the triple serpentine asymmetric pitch flow field with 0.5 mm square channels, 0.5 mm cathode lands, and 1.5 mm anode lands.

The materials used in this work consist of Mitsubishi Rayon Corporation (MRC) 220 μm thick U105 diffusion media with 5% wt. wet proofing and 30 μm MPL, W. L. Gore 18 μm Select Series membrane with 0.05 mg Pt/cm^2 anode catalyst loading and 0.3 mg Pt/cm^2 cathode catalyst loading. The virgin material set used all fresh materials. General Motors Electrochemical Energy Research Laboratory provided two 400 cm^2 5 layer membrane electrode assemblies (MEA) that had been aged in stacks in fuel cell vehicles for 174 and 2666 hours. The aged material sets consist of the same materials as the virgin case. Aged Samples for the neutron imaging experiments and x-ray

119

photoelectron spectroscopy (XPS) were cut from the center of the active area of the aged MEAs while samples for the thermal conductivity testing were cut from the entrance, center, and exit regions of the MEA. The fuel cell stacks operate in counter-flow so the anode entrance region matches up with the cathode exit region.

7.2.2 Neutron Test Facility and Conditions

Neutron imaging experiments were conducted at the NIST Center for Neutron Research in Gaithersburg, MD with the BT-2 Neutron Imaging Facility. The high resolution microchannel plate detector was used to achieve the highest possible spatial resolution of 15 μm. Five minute images were taken to achieve high neutron counts. For the analysis, the images were summed together in groups of 4 to achieve 20 minute images for each analysis point.

Conditions tested in this work follow the same conditions from Chapter 3 to match the results of the aged materials to the virgin material case. These conditions impose pressure, concentration, and temperature driven gradients across the membrane to determine how these can impact cell water balance. Flow rates for all conditions was set to a constant flow rate equivalent to a 2|2 stoichiometry at 1.2 A/cm^2. Table 7-1 provides an overview of all conditions tested.

7.2.3 Ex Situ Characterization

Thermal conductivity measurements of the virgin and aged materials was performed with the Hot Disk AB Transient Plane Source TPS 2500 S thermal constants

Table 7-1: Operating parameters.

Operating Parameters	Values [units]
Current Density	0.1, 0.4, 0.8, 1.2, 1.5 [A/cm^2]
Temperature	40, 60, 80 [°C]
Pressure Gradient anode|cathode	100|150, 150|150, 150|100 [kPa(a)]
Concentration Gradient anode|cathode	50|50, 95|50, 50|95, 95|95 [inlet %RH]

analyzer. This system can make rapid thermal conductivity measurements of thin samples using a transient analysis method. The thin film sensor acts as the heat source and the temperature sensor for the system. A prescribed amount of power is applied to the nickel foil sensor coil for a specified duration while a multimeter measures the change in resistance of the foil with increasing temperature. The thermal conductivity of the samples is determined by a numerical solver in the system software based on the temperature response of the sensor with time.

Carbon fiber based fuel cell diffusion media thermal conductivity shows a strong correlation with compression force. A clamp was used to compress the samples between the stainless steel backing plates and a load cell was used to accurately measure the compression force. The load cell was placed underneath the lower backing plate as shown in Figure 7-1. Stress-strain relationships were determined for the virgin materials over a range of compression pressures while compressed thickness for the aged materials was measure only at 2 MPa of compression pressure via the process outlined by Xu et al. [106]. All samples were corrected for compressed thickness in the thermal conductivity measurements.
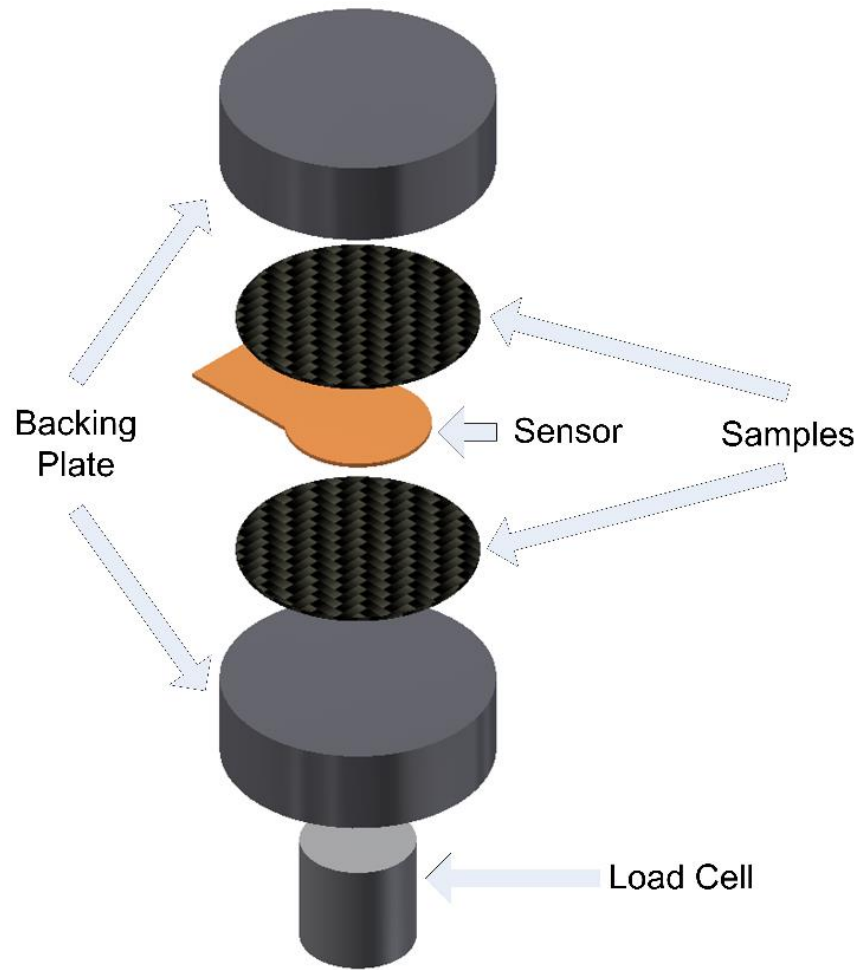
Figure 7-1: Exploded schematic representation of sample fixturing for the TPS 2500 S. Samples are placed between two stainless steel backing plates with well know thermal conductivity values with the heater/sensor placed between the samples.

7.3 Results and Discussion

7.3.1 Neutron Imaging Results

Neutron imaging was used to ascertain the differences in water accumulation for virgin and stack aged materials that operated for 2666 hours before removal. Testing began at 40°C with the exhaust pressure conditions. As has been previously shown in Chapter 3, the virgin (baseline) material set had large variation in anode water content strongly dependent on operating condition. The water content of the aged material shows a significant decrease in maximum anode water accumulation and variability along with an increase in peak cathode saturation as shown in Figure 7-2. This trend follows what was seen in Chapter 5 and indicates a reduction in water transport to the anode from the cathode. The increase in cathode peak saturation indicates that the cathode is removing a larger percentage of product water than in the virgin case as a high flux would be required to maintain the high saturation levels. Average voltage values for the three conditions is given in Table 7-2.

Exhaust pressure conditions were next tested at 60°C. As at 40°C, large anode water accumulation is seen in virgin material configuration with peak saturation values between 45 and 55%. A sharp decrease in in anode water content is seen for the 2666 hour aged materials in Figure 7-3. The trend in the saturation profiles changes between the two configurations with the virgin material set seeing a peak in saturation near the center of the DM whereas the aged material has its peak saturation occur at the DM|flow field boundary. This could indicate that water can more freely move via capillary action towards the anode flow field in the aged material compared to the virgin case. Some decrease in the anode saturation is attributable to decreased back diffusion
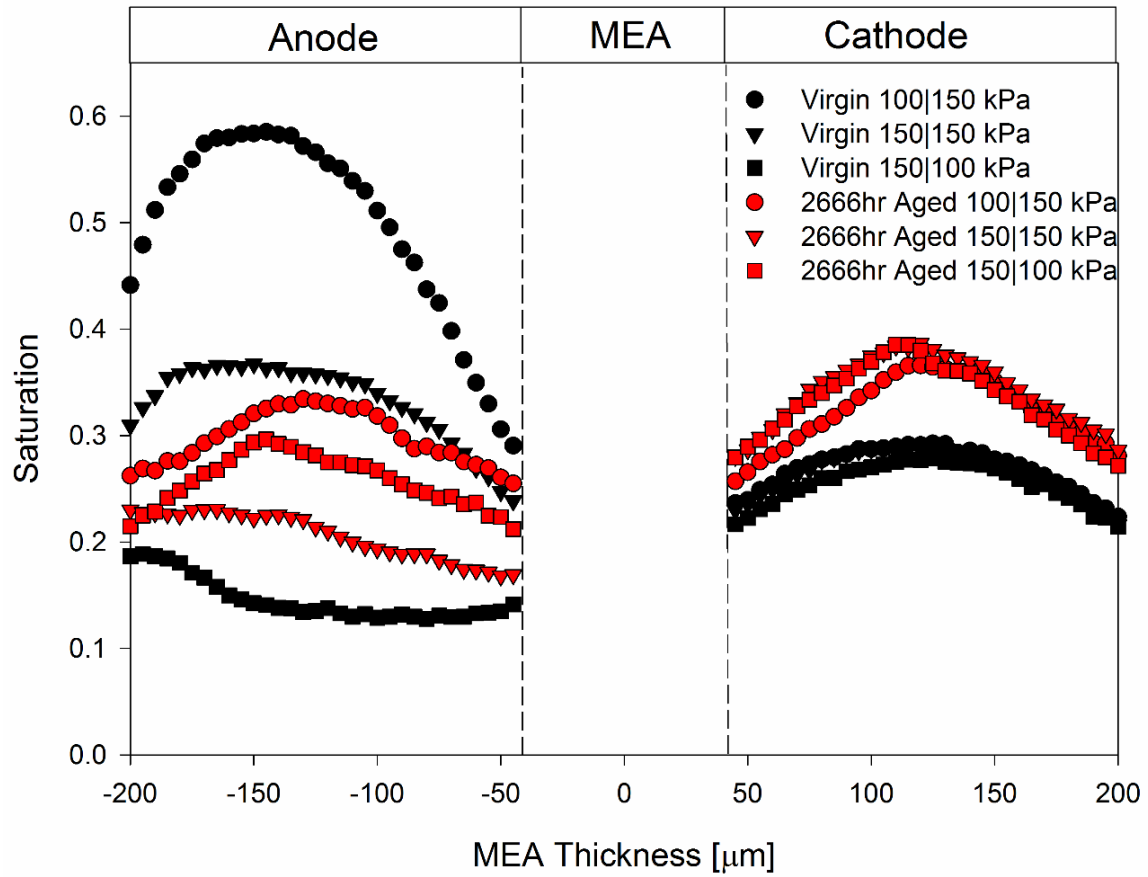
Figure 7-2: Exhaust pressure condition saturation profiles for 0.8 A/cm^2 at 40°C test conditions for virgin and 2666hr aged materials. Test conditions: 95|95% inlet RH, constant gas flow rates with equivalent 2|2 stoichiometry at 1.2 A/cm^2.

Table 7-2: Operating voltages for test conditions shown in saturation profiles

Condition		Voltage [V]	
		Virgin	2666hr
40°C	100|150 kPa, 95|95 %RH, 0.8 A cm^{-2}	0.651	0.557
	150|150 kPa, 95|95 %RH, 0.8 A cm^{-2}	0.608	0.665
	150|100 kPa, 95|95 %RH, 0.8 A cm^{-2}	0.634	0.687
60°C	100|150 kPa, 95|95 %RH, 1.2 A cm^{-2}	0.594	0.582
	150|150 kPa, 95|95 %RH, 0.1 A cm^{-2}	0.845	0.823
	150|150 kPa, 95|95 %RH, 0.4 A cm^{-2}	0.761	0.758
	150|150 kPa, 95|95 %RH, 0.8 A cm^{-2}	0.701	0.705
	150|150 kPa, 95|95 %RH, 1.2 A cm^{-2}	0.558	0.620
	150|150 kPa, 95|95 %RH, 1.5 A cm^{-2}	0.560	N/A
	150|100 kPa, 95|95 %RH, 1.2 A cm^{-2}	N/A	0.585
	50|95 %RH, 150|150 kPa, 1.2 A cm^{-2}	0.597	0.591
	95|50 %RH, 150|150 kPa, 1.2 A cm^{-2}	0.592	0.612
	50|50 %RH, 150|150 kPa, 1.2 A cm^{-2}	0.598	0.622
80°C	100|150 kPa, 95|95 %RH, 1.5 A cm^{-2}	0.577	0.421
	150|150 kPa, 95|95 %RH, 1.5 A cm^{-2}	0.608	0.484
	150|100 kPa, 95|95 %RH, 1.5 A cm^{-2}	0.569	0.383
	50|95 %RH, 150|150 kPa, 1.5 A cm^{-2}	0.637	0.519
	95|50 %RH, 150|150 kPa, 1.5 A cm^{-2}	0.594	0.484
	50|50 %RH, 150|150 kPa, 1.5 A cm^{-2}	0.594	0.488
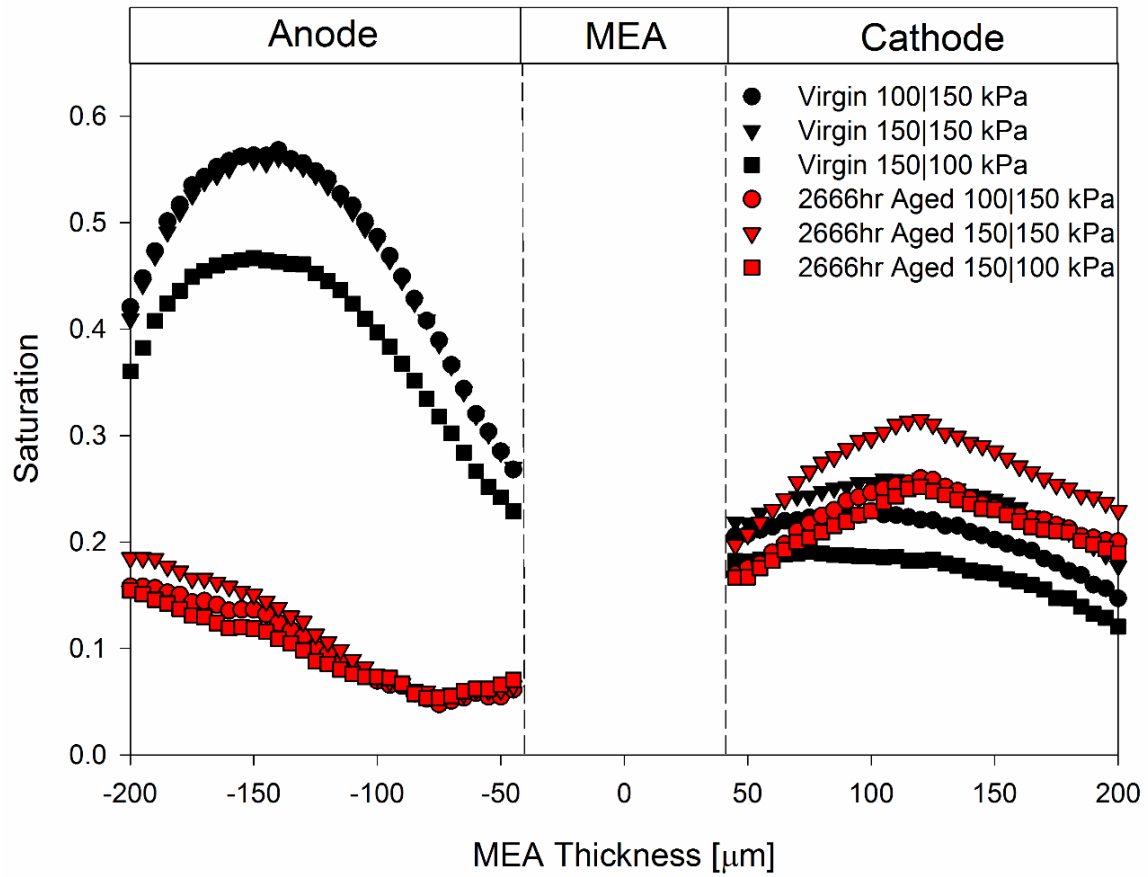
Figure 7-3: Saturation profiles for exhaust pressure conditions at 60°C operating at 1.2 A/cm². Test conditions: 95|95% inlet RH, constant gas flow rates with equivalent 2|2 stoichiometry at 1.2 A/cm².

from the cathode as the increase in peak cathode saturation shows more water is transported out through the cathode. The improved drainage to the gas channels is evident in the neutron radiographs in Figure 7-4. Exhaust pressure conditions at 60°C for the virgin material set shows little to no water accumulation in the gas channels while the aged material set has water accumulation in the anode gas channels and regions of wicking water in the corners of the cathode channels at the DM interface.

Inlet relative humidity was first tested at 60°C as proper control of the humidifier temperature at lower testing temperatures would be difficult. The virgin material set showed large anode water accumulation with changing inlet relative humidity gradients. Highest anode saturation occurred when anode inlet relative humidity was set to 95%. As seen in the exhaust pressure testing conditions, peak anode saturation approached 55%. Water accumulation was again reduced for the aged material compared to the virgin configuration as shown in Figure 7-5. The saturation trends for the aged material follows what was seen in the exhaust pressure testing conditions with peak anode saturation primarily occurring at the flow field interface and an upward shift in cathode peak saturation. The reduction in anode water content again indicates an improved drainage to the gas channels that prevents large water storage and a reduction in back diffusion from the cathode supplying less water to the anode.

At 80°C, the virgin material had significantly smaller quantities of liquid water present in the cell with peak anode water content approaching 20%. Water content for the aged material only approached 5% as shown in Figure 7-7 for exhaust pressure testing and Figure 7-8 for inlet relative humidity testing. The reduction in water content can be attributed to lower back diffusion to the anode but also follows trends seen in

127
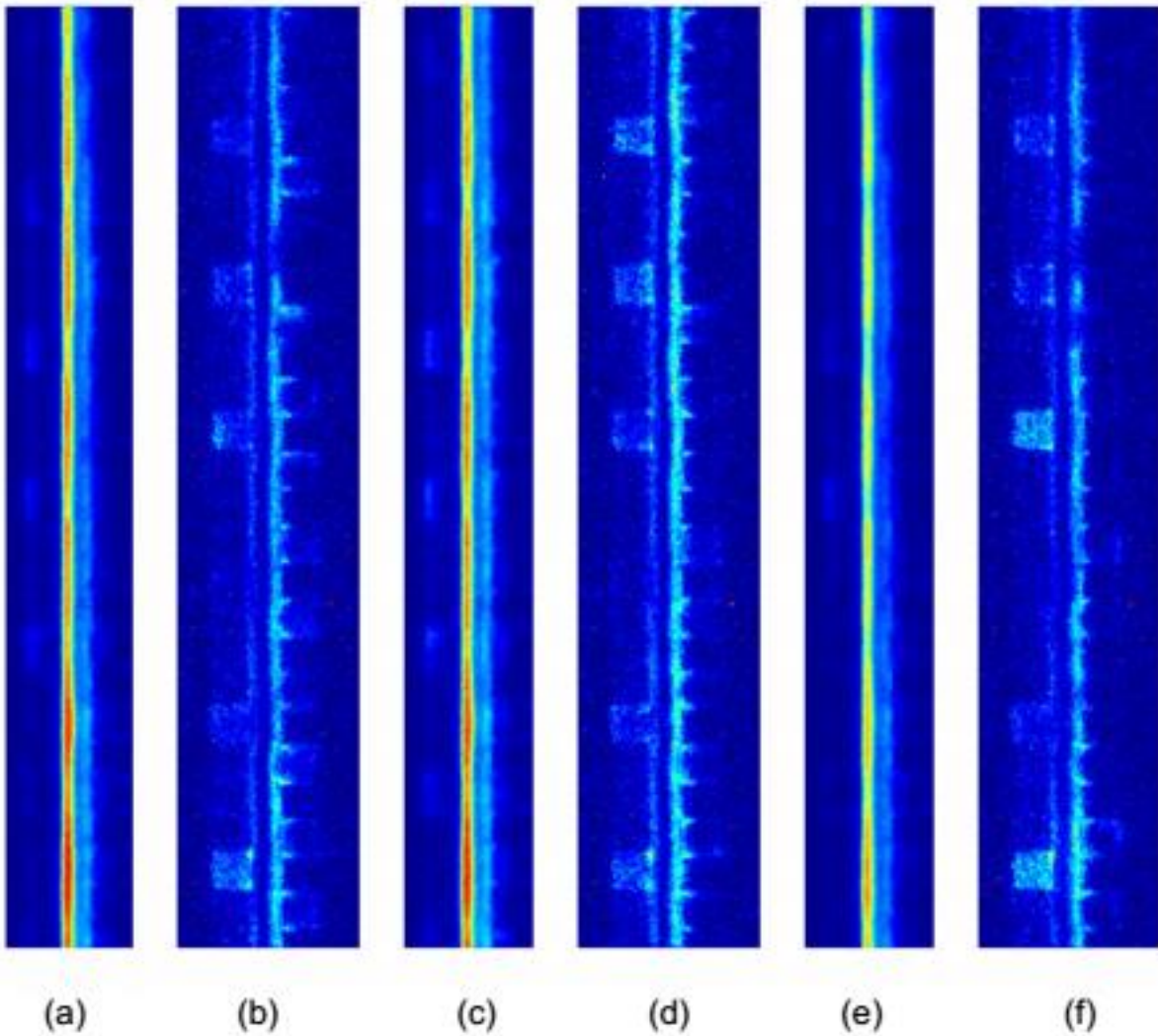
Figure 7-4: Neutron radiographs for (a) asymmetric 100|150 kPa, (b) symmetric 100|150 kPa, (c) asymmetric 150|150 kPa, (d) symmetric 150|150 kPa, (e) asymmetric 150|100 kPa, (f) symmetric 150|100 kPa at 60°C comparing channel and DM water content between cases.
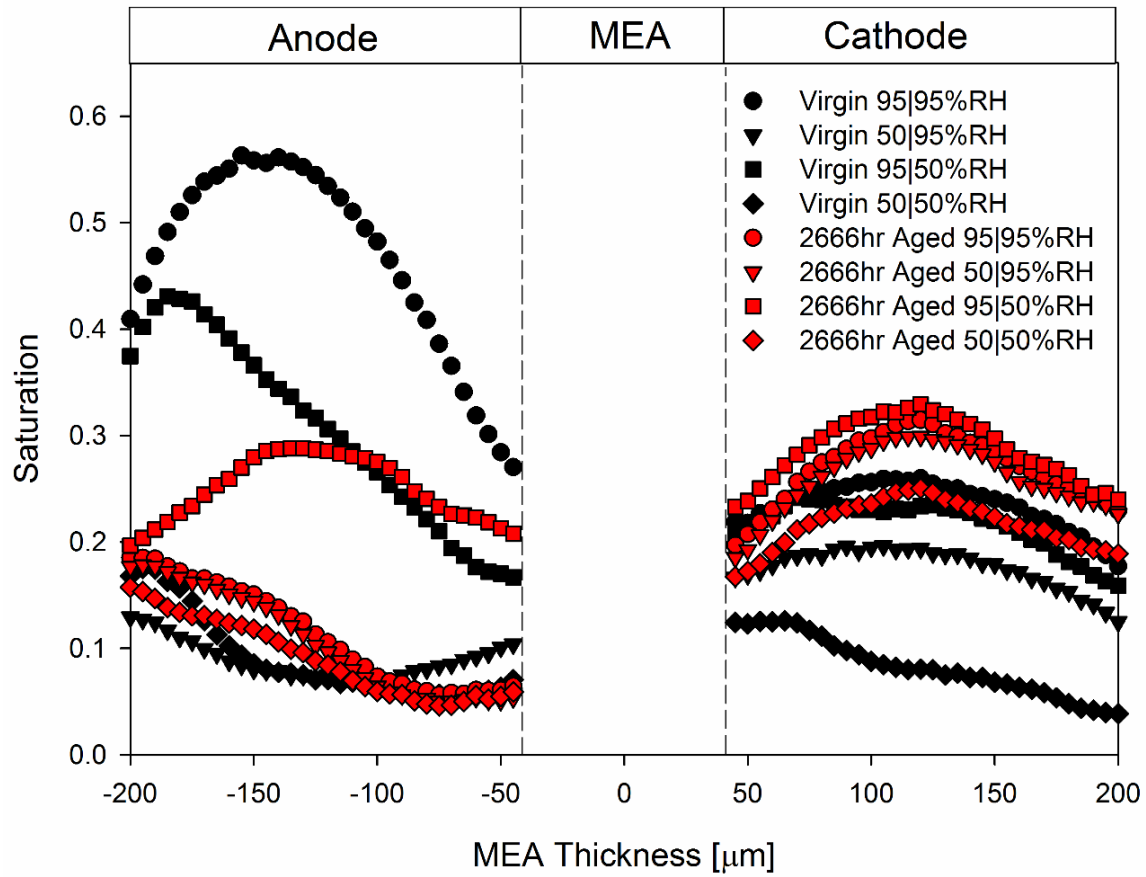
Figure 7-5: Saturation profiles for relative humidity conditions at 60°C operating at 1.2 A/cm^2. Test conditions: 95|95% inlet RH, constant gas flow rates with equivalent 2|2 stoichiometry at 1.2 A/cm^2.
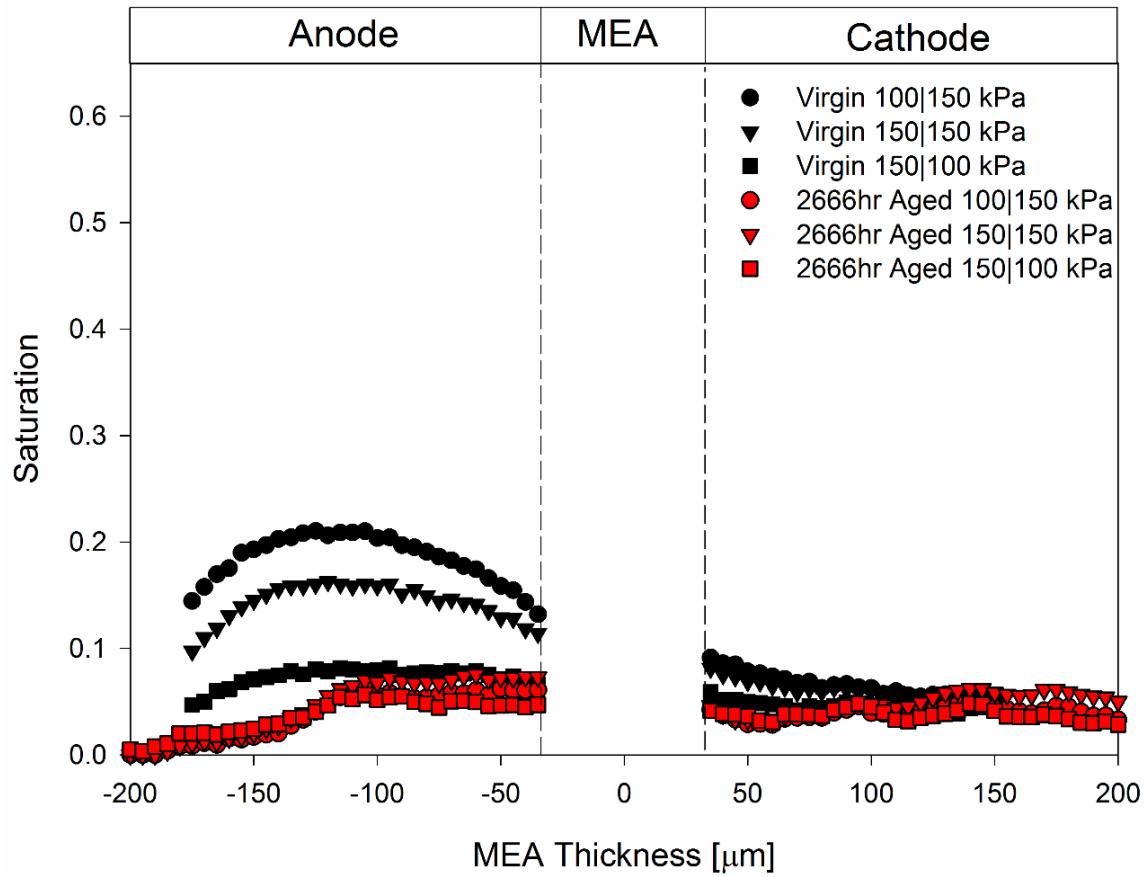
Figure 7-6: Saturation Profiles for exhaust pressure conditions at 80°C operating at 1.5 A/cm^2. Test conditions: 95|95% inlet RH, constant gas flow rates with equivalent 2|2 stoichiometry at 1.2 A/cm^2.
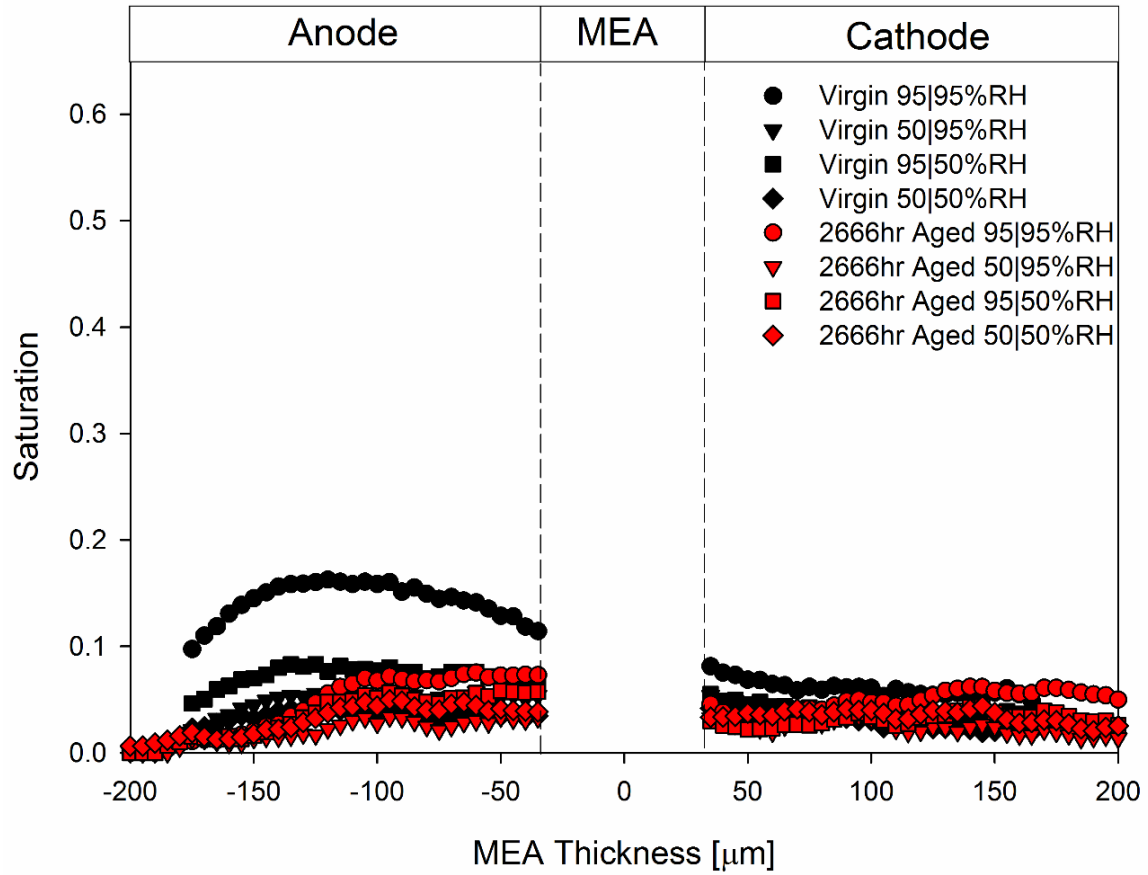
Figure 7-7: Saturation profiles for relative humidity conditions at 80°C operating at 1.5 A/cm^2. Test conditions: 95|95% inlet RH, constant gas flow rates with equivalent 2|2 stoichiometry at 1.2 A/cm^2.

Chapter 6 where higher thermal conductivity reduced transport to the anode and therefore water storage on the anode. Effects of ageing on thermal conductivity will be investigated later in this chapter.

Water accumulation for the virgin material begins at low current densities with noticeable saturation at 0.4 A/cm^2 and high saturation values occurring at 1.2 and 1.5 A/cm^2. The rapid accumulation in anode water content seen in the virgin material set with increasing current density is not seen in the 2666 hour material set as shown in Figure 7-8. Cathode profiles for 0.8 and 1.2 A/cm^2 show an increase in cathode peak saturation and channel interface saturation indicating a higher percentage of generated water leaving the cathode. Drainage on the anode, although enhanced for the 2666 hour set, shows a rate limit as the interface saturation with the channel increases with increasing water generation when going from 0.8 to 1.2 A/cm^2.

7.3.2 X-ray Photoelectron Spectroscopy Characterization

X-ray photoelectron spectroscopy (XPS) was used to determine if any surface occurred to the aged material sets. The XPS spectra for the samples were normalized to the carbon-carbon peak at a binding energy of 285 eV. Figure 7-9 shows the XPS spectra for the binding energies associated with carbon bonds. A shift in the shoulder of the peak in the 285.5 to 290 eV range can be seen for all of the aged materials. This shift indicates an increased level of carbon-oxygen bonding and carbon corrosion. The oxygen groups bonded to the carbon can include hydroxyl, phenol, and other hydrocarbon groups but requires further analysis to determine specifics on these functional groups. The addition of these oxygen groups increase the hydrophilic nature
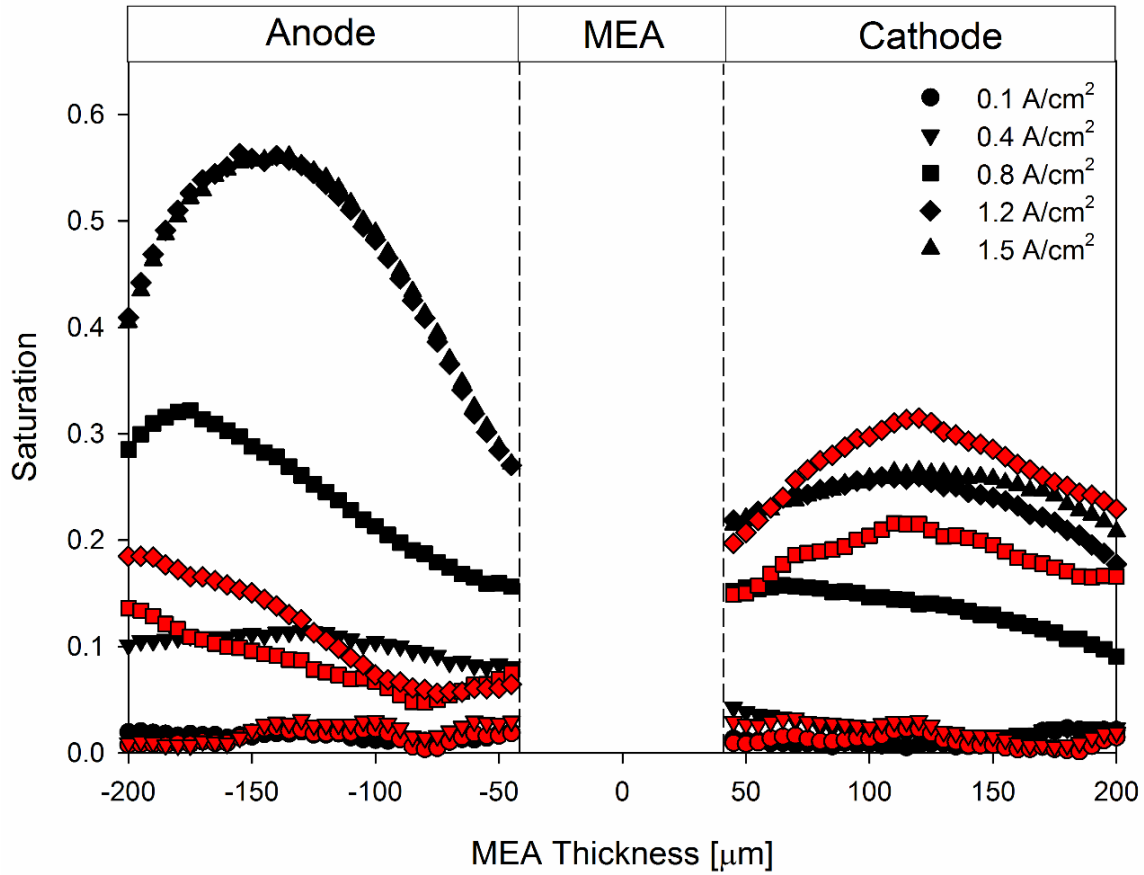
Figure 7-8: Saturation profiles as a function of current density at 60°C for the 150|150 kPa(a) test condition. Virgin material configuration shown in black and the 2666 hour aged material configuration is shown in red. 2666 hour 1.5 A/cm² condition is not plotted due to failure to complete test duration.
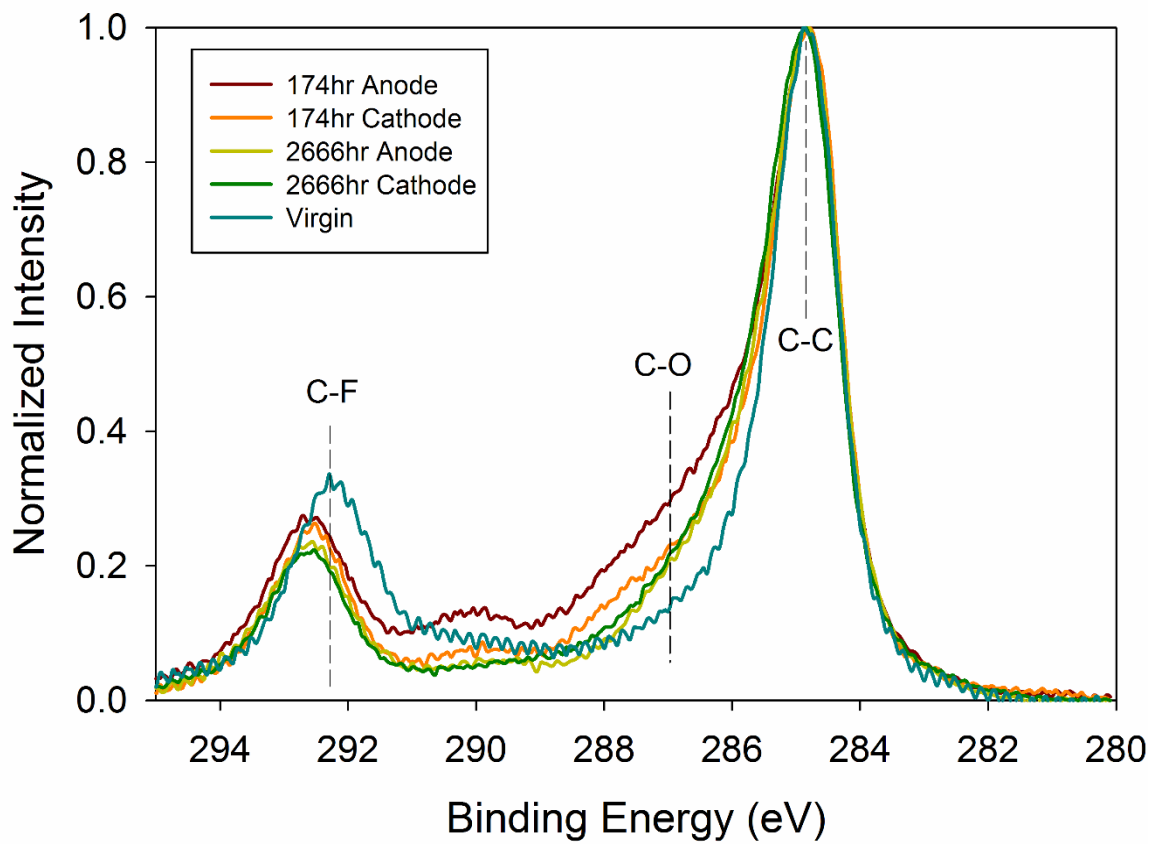
Figure 7-9: XPS spectra representing the binding energy for carbon bonds normalized to the carbon-carbon peak.

of the material which improves water drainage from the DM. In addition to the increased functionalization, a decrease in the carbon-fluorine peak occurs indicating a reduction in the amount of PTFE present in the samples. To improve the understanding of the changes to PTFE, Figure 7-10 shows the binding energy range associated with fluorine. In this spectra, a shift is present in the 691.5 to 695 eV range. A shift at this high binding energy is associated with sample charging due to accumulation of electrons on the sample. This shift combined with the reduction in carbon-fluorine bonds show that PTFE is breaking up into smaller isolated particles. PTFE is used as the wet proofing agent in the samples and reducing the quantity and quality increases the hydrophilic nature of the material. The reduction in hydrophobic wet proofing and increased surface functionalization improves capillary transport of liquid water through the material thus enhancing drainage.

7.3.3 *Thermal Transport Characterization*

Thermal conductivity measurements were carried out on virgin and aged materials at 2 MPa of compression pressure to match typical forces seen in operating fuel cells. Four virgin material configurations were tested to determine a baseline and range of thermal conductivity for new materials. These configurations include untreated plain MRC paper, MRC paper treated with 5% wt. PTFE, MRC treated paper with MPL, and MRC treated paper where the MPL has been partially removed. Testing of the untreated and treated papers was intended to determine the maximum change in thermal conductivity if PTFE washout was responsible while the partially removed MPL sample was to simulate the aged samples as the MPL tended to peel from the DM when
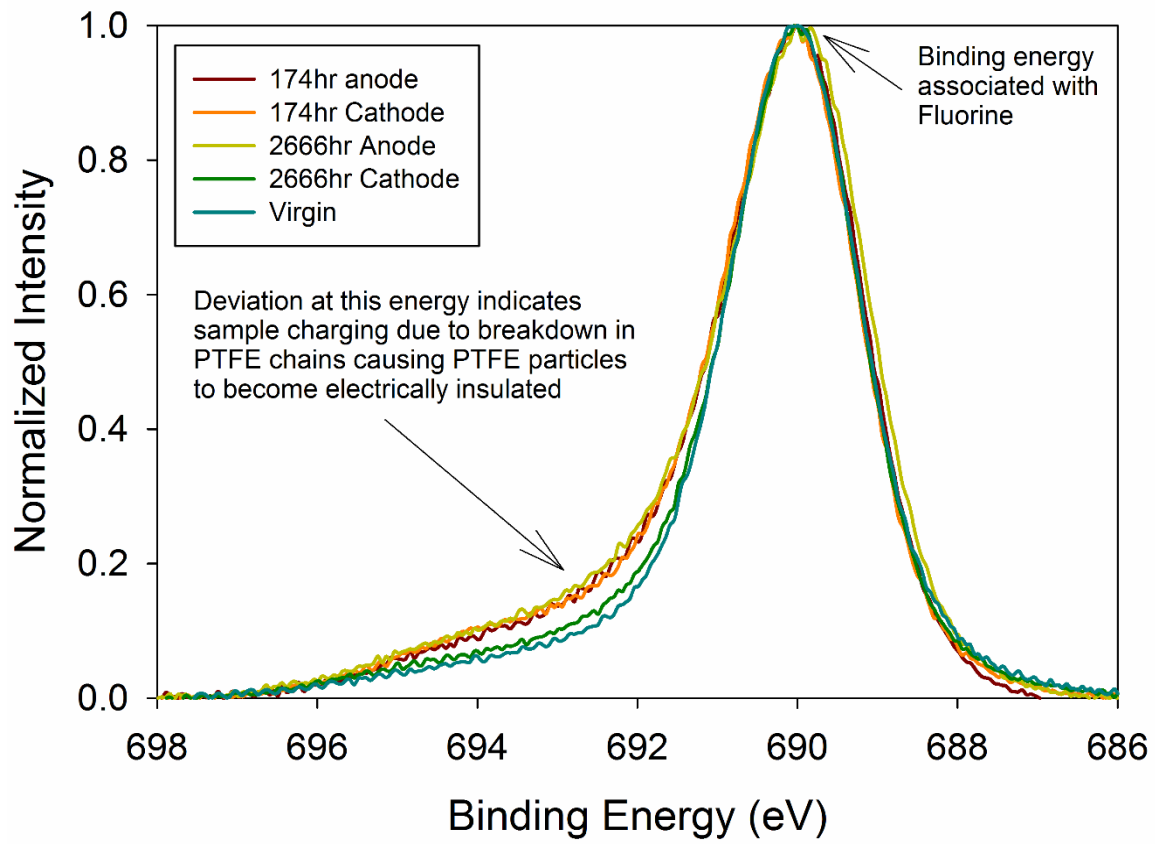
Figure 7-10: XPS spectra representing the binding energy for fluorine.

it was removed from the MEA. Aged samples were cut from the inlet, mid, and outlet regions of both the cathode and anode for the 174 and 2666 hour material sets.

Treated MRC without MPL and treated MRC with MPL represent the lower and upper bounds of expected values for thermal conductivity. The MPL has a large effect on thermal conductivity due to its higher stand-alone thermal conductivity, improvement to contact resistance, and the improved internal contact resistance for the comingled region. A marginal, 0.01 W/m-k, increase in thermal conductivity was found for the untreated sample. This would be expected as the wet-proofing only represents 5% by weight of the entire sample. The partially removed MPL sample falls roughly halfway between the no MPL and MPL coated samples and represents the expected value of the aged materials if no change to thermal conductivity occurred.

Values for thermal conductivity for all samples tested is given in Figure 7-11. It can be seen that thermal conductivity can vary significantly for the aged samples. The 174 hour anode inlet and mid regions, 174 hour cathode, and 2666 hour cathode inlet region show negligible changes compared to the virgin partially removed MPL case. Large changes in thermal conductivity begin in the anode outlet regions and increase with age. The stacks are known to accumulate significant amounts of water in the anode exit during operation and shutdown which could cause the changes seen here. The 2666 hour anode outlet region was not able to produce stable results at 2 MPa of compression and therefore is not shown in Figure 7-11. Thermal conductivity can be seen to increase with age for both the anode and cathode shown by the increase in value and spread between regions when comparing the 174 hour and 2666 hour cases. Environmental conditions on the anode have stronger influences on material changes
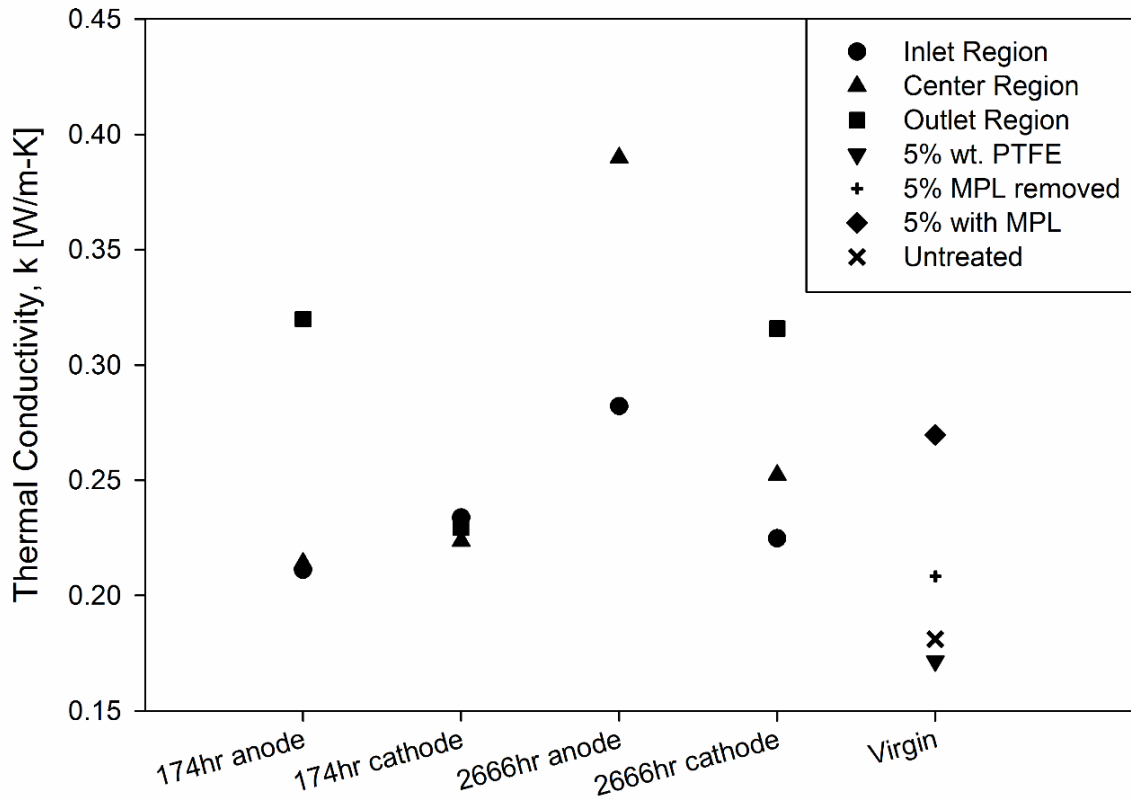
Figure 7-11: Thermal conductivity values for aged samples as a function of location in cell.

than on the cathode. Tabulated values for all plotted measurements is given in Table 7-3.

Peak cell temperature has been shown to be an important parameter for thermally driven flow. The values of thermal conductivity measured for the aged materials were entered into a COMSOL thermal model to determine the change in peak temperature compared to the virgin material case. Peak temperature is shown to decrease with operational age and anode region in Figure 7-12. For both age cases the anode inlet|cathode outlet region and the middle region have similar peak temperatures while the anode exit|cathode inlet region sees a 2° and 3° drop in peak temperature from the rest of the cell for the 174 hour and 2666 hour samples, respectively. The 2666 hour anode outlet region has an 8° temperature decrease compared to the virgin material case. This large drop in temperature significantly reduces the driving force for thermal transport through the cell.

The 2-dimensions temperature distributions that were produced with COMSOL were used to calculate TTN profiles, as described in previous chapters, for all of the aged cases. These profiles are compared to the virgin material set in Figure 7-13. The TTN profiles follow the peak temperature trends from Figure 7-12 with the 174 hour anode inlet and mid regions having the highest TTN of the aged samples. A minimum of a 50% reduction in peak TTN can be seen for the 2666 hour samples with the outlet region having an 82% reduction in peak TTN. This ageing effect could have significant impacts on full scale stack performance as these cells would typically operate in counter-flow. In this configuration, the wet cathode exit region would facilitate back diffusion to the anode inlet region which would remain in a dryer state due to the high

139

Table 7-3: Thermal conductivity values for all samples

	untreated	5% wt. PTFE	5% with MPL	5% w/ removed MPL
Virgin	0.1811	0.1716	0.2697	0.2083

	174hr		2666hr	
location	anode	cathode	anode	cathode
inlet	0.2111	0.2338	0.2821	0.2248
mid	0.2141	0.2236	0.3899	0.2522
outlet	0.3199	0.2293	*	0.3158

compression [MPa]	*2666hr anode
1	0.4757
1.5	0.9737
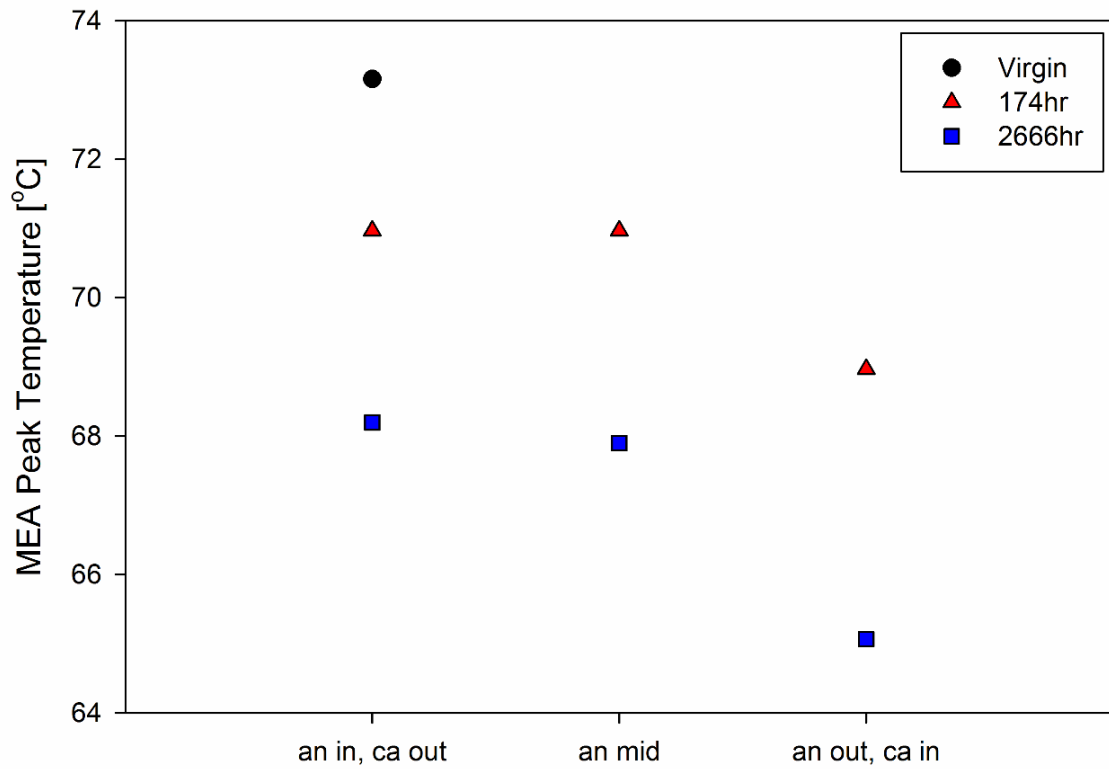
Figure 7-12: Peak catalyst temperature based on age and cell location calculated using measured thermal conductivity values.
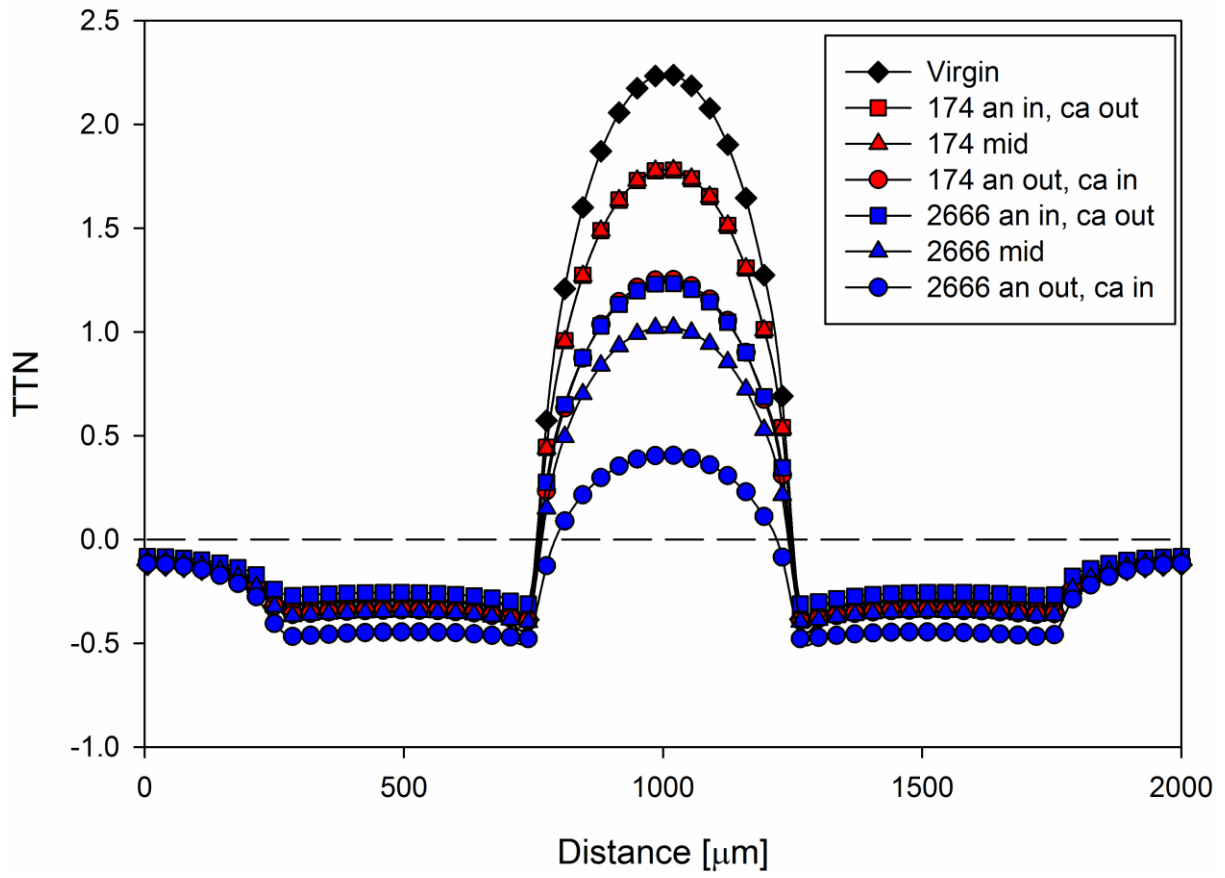
Figure 7-13: TTN profile plot comparing virgin maximum thermal driving force with all aged case for 60°C, 150|150 kPa, and 95|95% RH.

flow rate available in this location. Water that accumulates in the anode exit region would have a very small force to drive any water back to the cathode thus trapping it in the anode. This becomes a critical issue for purge as the high water volume would require longer and/or higher flow rate purges that would be detrimental to the efficiency of the system.

The saturation profiles presented earlier in this chapter show an increase in peak saturation in the cathode implying a larger percentage of water is transported out the cathode compared to the virgin material set. Figure 7-14 gives the relevant TTN profiles that correspond to the neutron imaging testing. The 2666 hour aged material has a 45% reduction in maximum possible thermal driving force. This reduced maximum would be further reduced when thermal conductivity is increased more due to the presence of saturation. By reducing the maximum driving force water transport to the anode is limited during the initial dry operation period preventing the buildup seen in the virgin case.

7.4 Conclusions

In this work, the effects of operational age on fuel cell water management characteristics were investigated with in situ and ex situ techniques. High resolution neutron imaging was used to determine the through-plane water content for virgin materials and materials aged for 2666 hours in a fuel cell vehicle. Total water content was found to significantly decrease from the virgin to aged materials. XPS found increased surface functionalization with oxygen groups and a decrease in quantity and quality of the PTFE wet proofing in the diffusion media. These two changes result in
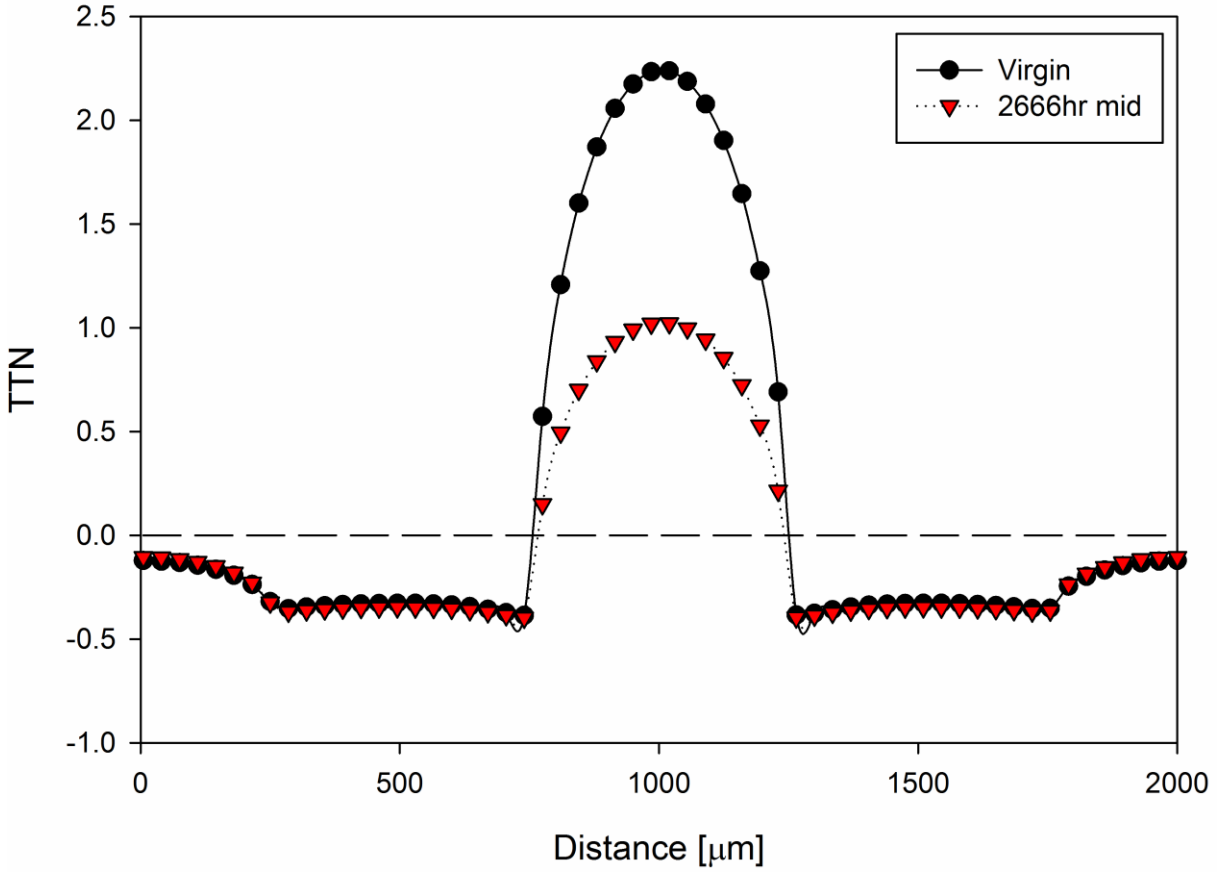
Figure 7-14: TTN profile for virgin and 2666 hour mid region cases used for neutron imaging testing for the 60°C, 150|150 kPa test condition.

increased hydrophilic nature of the DM and allow for improved drainage of stored water to the gas channels. Evidence of this improved draining was shown with increased channel water and wicking zones at the DM|channel interface in the neutron radiographs.

To further understand the reduction in water content, the thermal conductivity of the virgin and aged materials were measured using the transient plane source method. Measurements were taken for the anode and cathode individually at the inlet, mid, and outlet regions of the MEA for 174 and 2666 hour aged material sets. The anode was found to have large increases in thermal conductivity that increased with operational age with conductivity increasing from inlet to outlet. The increase in thermal conductivity was found to reduce the maximum thermal transport in the cell by 45%. This reduction in thermal driving force reduced the back diffusion of water from cathode to anode aiding in the reduction of water content with age.

To meet the recommended durability goals for fuel cells it will be necessary to properly understand these degradation modes. Increased thermal conductivity of the diffusion media has a strong influence on cell operating temperature and thermal transport of water vapor. These large material property changes can have significant effects on start/stop durability as they change the water balance of the cell and can alter the effectiveness of shutdown purge which could cause membrane damage or difficulty on startup.

CHAPTER 8: Design Guideline for Thermally Driven Transport in PEFCs – A Parametric Study of Transport Controlling Properties

This Chapter will be submitted for publication in The Journal of the Electrochemical Society with the following authors and title:

J.M. LaManna, and M.M. Mench, "Thermally driven water transport in PEFCs – Part 3: Parametric design guideline"

My contribution is the entirety of this chapter.

8.1 Introduction

In Chapters 4-7 it has been shown that thermally driven transport in the diffusion media of PEFCs has a strong influence on cell water balance and performance. Channel and land dimensions, DM tortuosity, DM thermal conductivity, and saturation for specific cases have been shown to have strong influence over the intensity of the thermally driven flow. To better understand how fuel cell materials can be engineered to control water balance and performance, a parametric study will be conducted over a large range of typical values for channel dimensions, land dimensions, porosity, thermal conductivity, tortuosity, and saturation to find the impact on thermally driven flow. These parameters represent engineering design considerations for fuel cell water management. This chapter will provide guidance for improved operation at higher

current densities where consideration must be given to proper water management. Thermally driven transport can be tailored to reduce anode water content in cases with high anode water content as seen in Chapter 3 or at the opposite end of the spectrum to drive water towards the anode to prevent or delay the onset of anode membrane dry out as seen in Refs. [95, 96].

8.2 Parametric Model

A thermal model has been developed in Chapters 4 and 5 that allows for quantification of thermally driven water transport. The model solves the two-dimensional steady-state temperature distribution for a given operating parameter to then determine the phase-change-induced (PCI) flow of water across the diffusion media. PCI flow is governed by Fick's Law of diffusion with dependency on distance and temperature as shown in Equations 8.1 and 8.2.

$$J_{PCI} = D_{eff} \frac{\partial C}{\partial x} \tag{8.1}$$

Where concentration, C, is a function of temperature.

$$C = \frac{P_{sat}}{RT} \tag{8.2}$$

To determine which side of the cell has the strongest PCI flux, a new parameter has been developed call the Thermal Transport Number (TTN) which is given in

Equation 8.3. The cathode PCI flux is normalized with the water generation quantity and is then subtracted from the normalized anode PCI flux. A positive TTN number indicates a preference for anode side water transport as long as water can transport across the membrane.

$$TTN = \left(\frac{J_{PCI}}{J_{gen}}\right)_{anode} - \left(\frac{J_{PCI}}{J_{gen}}\right)_{cathode} \qquad (8.3)$$

To determine how to control cell water balance using thermally driven transport, a parametric study will be performed on variables that control thermal transport in the cell such as DM thermal conductivity, porosity, tortuosity, and saturation and flow field channel and land width. Temperature distributions for each case will be solved using COMSOL 4.3a. The modeling domain for the temperature distribution is the symmetric baseline geometry from Chapter 5 and will be referred to as the study standard reference for this chapter. A schematic of the geometry is given in Figure 8-1 and constants for the COMSOL model are given in Table 8-1. Once the temperature distribution for each case is known, a MATLAB model is used to conduct the parametric study and calculate the TTN value for each case. The TTN value is the integrated value along the entire symmetrical repeat distance of the COMSOL model. The parametric variables for the study are given in Table 8-2 below.
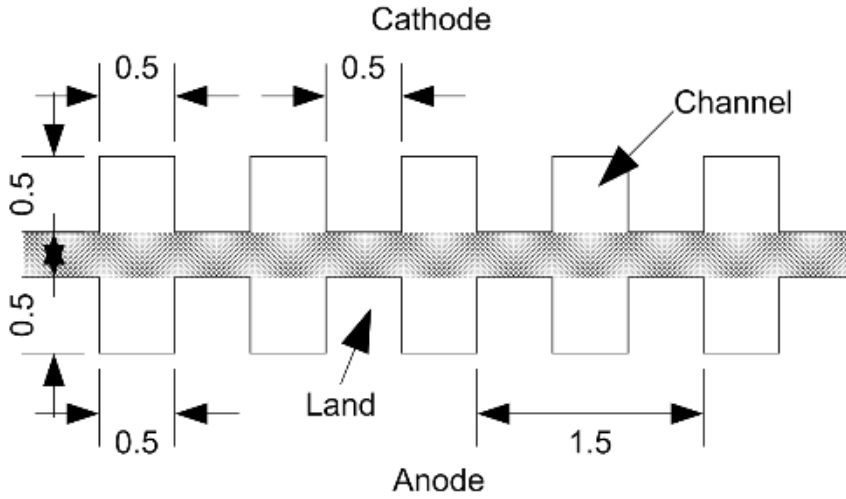
Figure 8-1: Parametric study standard comparison point channel dimensions.

Table 8-1: Constant model variables

Variable	Value
current density	1.2 A/cm^2
voltage	0.55 V
CL thermal conductivity	0.3 W/m-K
Membrane thermal conductivity	0.16 W/m-K
DM thickness	200 μm
CL thickness	10 μm
Membrane thickness	18 μm

Table 8-2: Parametric model variables

| | Parametric Properties [anode\|cathode] | |
	Standard Reference	Sweep Values
Thermal Conductivity [W/m-K]	0.18|0.18	0.1, 0.2, 0.3, 0.4, 0.5, 0.75, 1.0, 1.25, 1.5, 2.0
Porosity	0.68|0.68	0.4-0.85 in 0.05 steps
Tortuosity	1.5|1.5	1-8 in 1 steps
Saturation	0|0	0, 0.05, 0.1, 0.15, 0.2, 0.25, 0.3, 0.4, 0.5, 0.6
Land Width [mm]	0.5|0.5	0.25, 0.5, 0.75, 1.0, 1.5
Channel Width [mm]	0.5|0.5	0.25, 0.5, 0.75, 1.0

8.3   Results and Discussion

8.3.1 Diffusion Media Thermal Conductivity

Thermal conductivity of the diffusion media is an important parameter as this effects the waste heat removal from the cathode catalyst layer and governs the peak temperature in the catalyst layer. Typical thermal conductivity values for commercially available materials can range from 0.2 W/m-K to 1.8 W/m-K [6, 106]. One hundred thermal conductivity combinations were analyzed to determine the influence on thermally driven transport. Figure 8-2 plots anode PCI flux that has been normalized with water generation as a function of anode thermal conductivity along constant cathode conductivity lines. It can be seen that the lower the thermal conductivity for both halves of the cell the higher the anode PCI flux. This is due to the insulating effect of the DM raising the temperature drop across the layers resulting in stronger driving forces. Thermal conductivity has a strong influence on PCI flux as seen by the rapid decay in

plot lines as anode thermal conductivity increases. Once both anode and cathode thermal conductivities increase above 0.4 W/m-K, PCI flux no longer becomes a dominant driving force in water transport.

The star in Figure 8-2 designates where the study standard reference case falls within the ranges of PCI flux. It can be seen that to adjust the strength of the PCI flux for the standard reference, thermal conductivity would need to be reduced for one or both of the diffusion media in the cell. This could require a new approach to designing a diffusion medium as values of thermal conductivity much lower than 0.2 begins to go outside the ranges of standard materials. Reducing PCI flux, on the other hand, would be easier as selecting a high thermal conductivity DM would reduce the peak temperature in the cell. Most commercial DM have thermal conductivity values above the standard reference in this study.

To determine how thermal conductivity changes cell water balance the TTN was computed for the range of conductivities and plotted in Figure 8-3. It can be seen that thermal conductivity has a very small influence on water balance by the small variance in TTN from -0.41 to 0.0. Choosing an asymmetric configuration with anode and cathode diffusion media of different thermal conductivities would have minimal influence on water balance and therefore is not an important factor when tailoring water balance. Where thermal conductivity is important is in producing the largest possible temperature difference across the DM to thermally drive the largest flux possible. Since most of the heat is generated in the cathode catalyst layer, the cathode will always dominate PCI flow over the anode for symmetric flow geometries, hence the negative range on TTN.
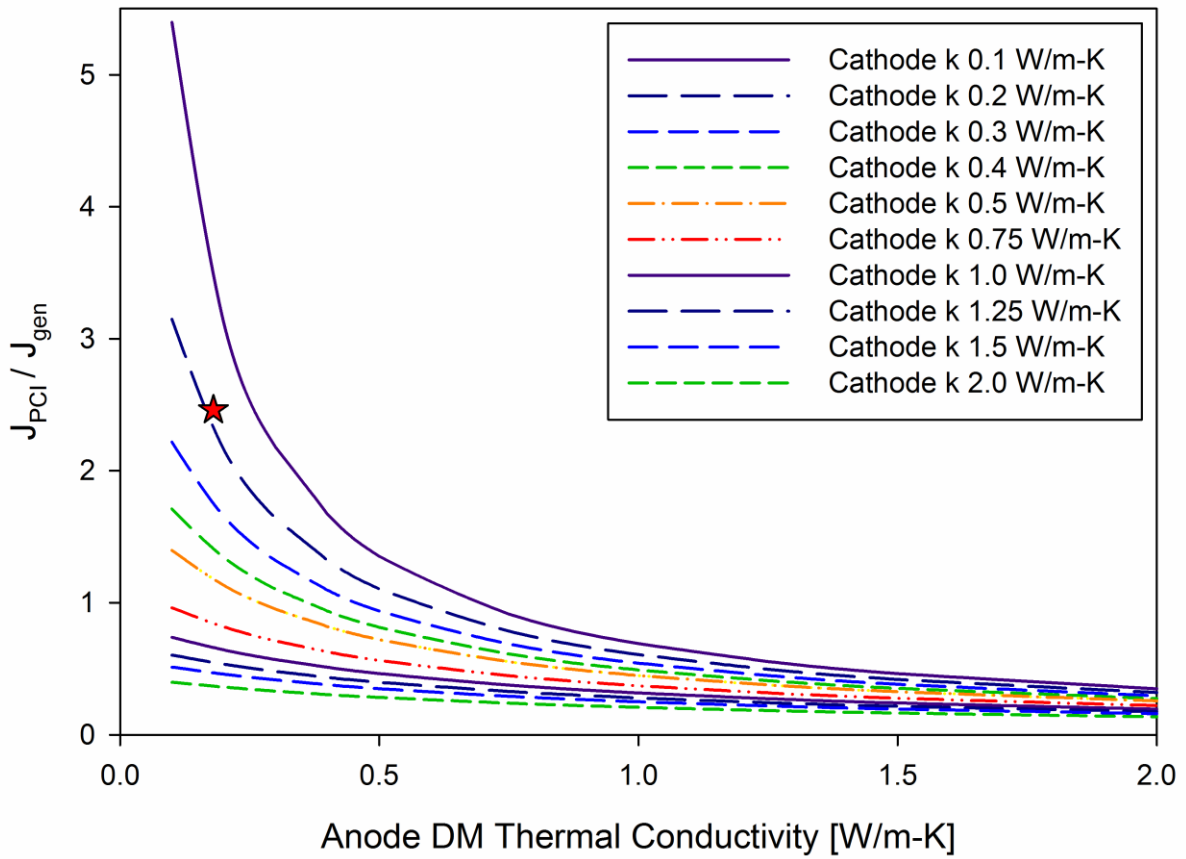
Figure 8-2: Normalized PCI flux for anode DM as a function of anode thermal conductivity. Star denotes study standard reference point.
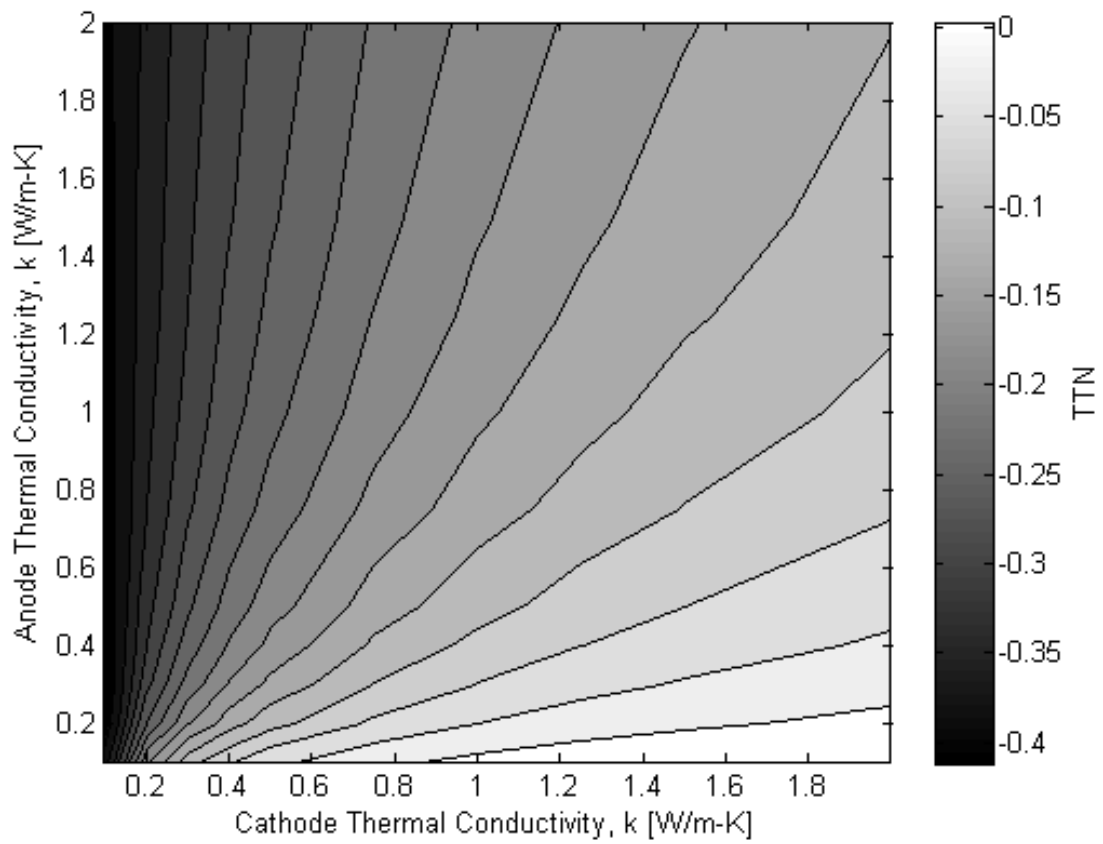
Figure 8-3: TTN distribution for anode and cathode thermal conductivity variation.

8.3.2 Diffusion Media Porosity

Porosity is an ideal parameter to engineer as it can be changed by several methods such as the addition of wet proofing, increasing or decreasing compression, use of filler materials, or through innovative new designs. Porosity has a direct effect on transport resistance through the material and therefore can be tailored to enhance or inhibit thermally driven and diffusive transport. To determine how porosity alters PCI flow through the anode, normalized PCI flux is plotted over the range of selected porosity in Figure 8-4. It can be seen that porosity can triple PCI flux with a doubling in porosity. The high end of the scale, 0.75-0.85, represents values of porosity for uncompressed commercial DM and would require a different material or manufacturing process to be achievable in actual operational fuel cells.

Cell water balance is strongly altered by porosity with the TTN ranging from -2.6 to 1.8. By increasing compressed porosity from a typical value of 0.6 of either the anode or cathode DM can drive preference towards the improved side. Reducing porosity would not be desirable as this may effect performance as similar water volumes would restrict diffusion to a greater extent in the reduced porosity case.

8.3.3 Diffusion Media Saturation

Saturation has been extensively shown to reduce performance and/or inhibit fuel cell operation at higher values in a process known as flooding. During this, liquid water occupies a significant enough fraction of the porous volume of the DM to restrict or stop the diffusion of hydrogen or oxygen. In this analysis, the effects of increased diffusion resistance due to saturation will be investigated along with the coupled reduction in

Figure 8-4: Normalized anode PCI flow as a function of DM porosity. Star denotes study standard reference point.
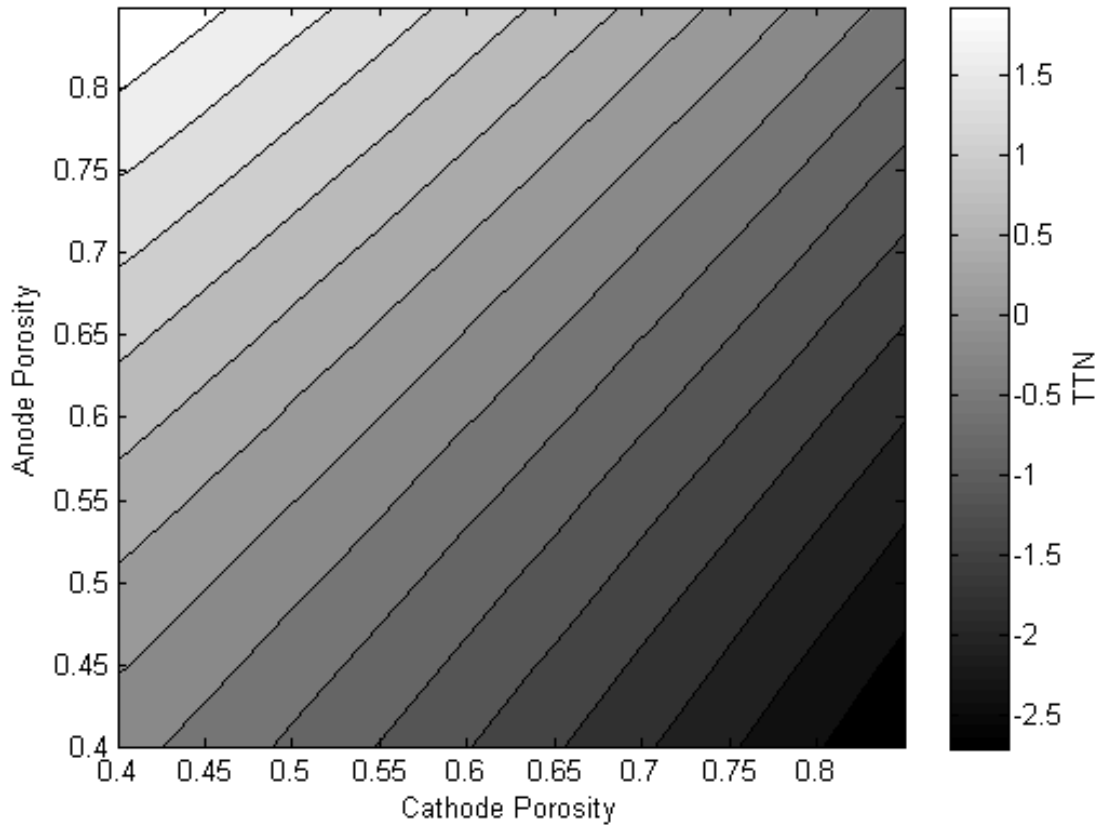
Figure 8-5: TTN distribution for anode and cathode DM porosity variation.

driving force due to increasing thermal conductivity with saturation. Figure 8-6 plots normalized PCI flux as a function of saturation with and without thermal conductivity changes with saturation. It can be seen by the rapid drop in maximum PCI flux that thermal effects associated with saturation are critical to predicting the correct water transport. Saturation only reduces the maximum driving force for the standard reference and therefore must be mitigated. This effect could be more profound in actual operation since this analysis does not account for the shape and distribution of water. In an actual fuel cell a film of water that could be equal to a low saturation value could completely block diffusion of reactants whereas this analysis assumes an even distribution of water and no complete gas phase blockage until 100% saturation. At 30% saturation, a value typically seen in fuel cell operation, the PCI flux is reduced to 20% its original value.

Chapter 3 has shown that it is possible to have significantly different saturation values between the anode and cathode, so it is important to determine how this influence cell water balance. Figure 8-7 shows the TTN distribution for the parametric analysis of saturation with and without coupled thermal effects. Saturation is shown to have a strong influence on water balance with preference switching to the opposite side when flooding occurs. At even rates of saturation for the anode and cathode, an even transport preference can exist. The influence of saturation on thermal transport is on the order of magnitude as porosity since saturation is only altering porosity in the top case of Figure 8-7, whereas when thermal conductivity is coupled as in the lower plot of Figure 8-7 the TTN range is halved. Therefore, to maintain high levels of thermally driven transport it is necessary to maintain saturation to as low as possible, especially when working with higher conductivity diffusion media.

Figure 8-6: Normalize anode PCI flux as a function of anode liquid water saturation.
Star denotes study standard reference point.
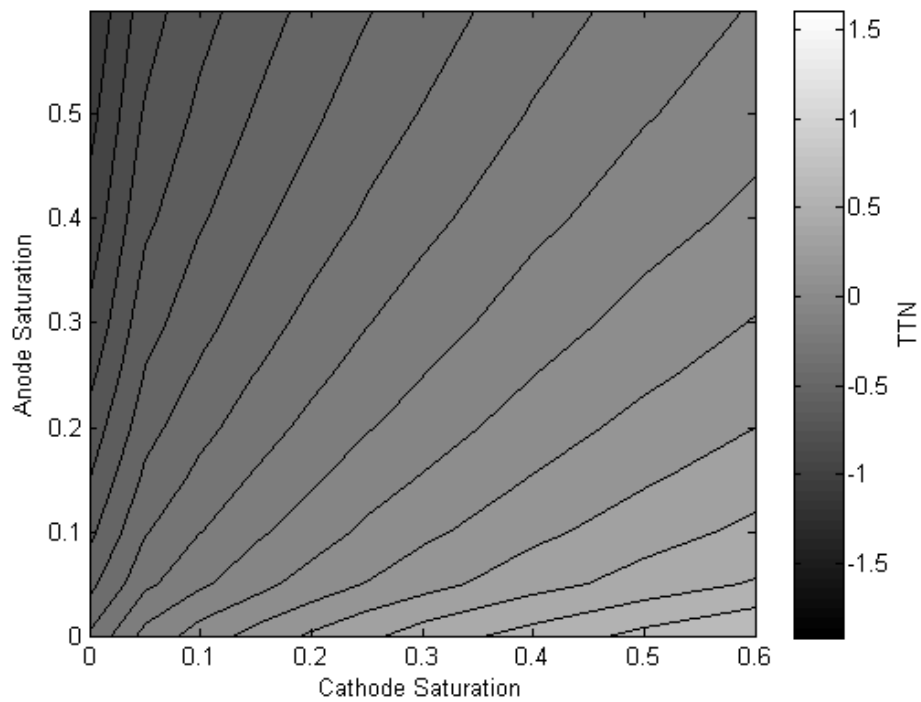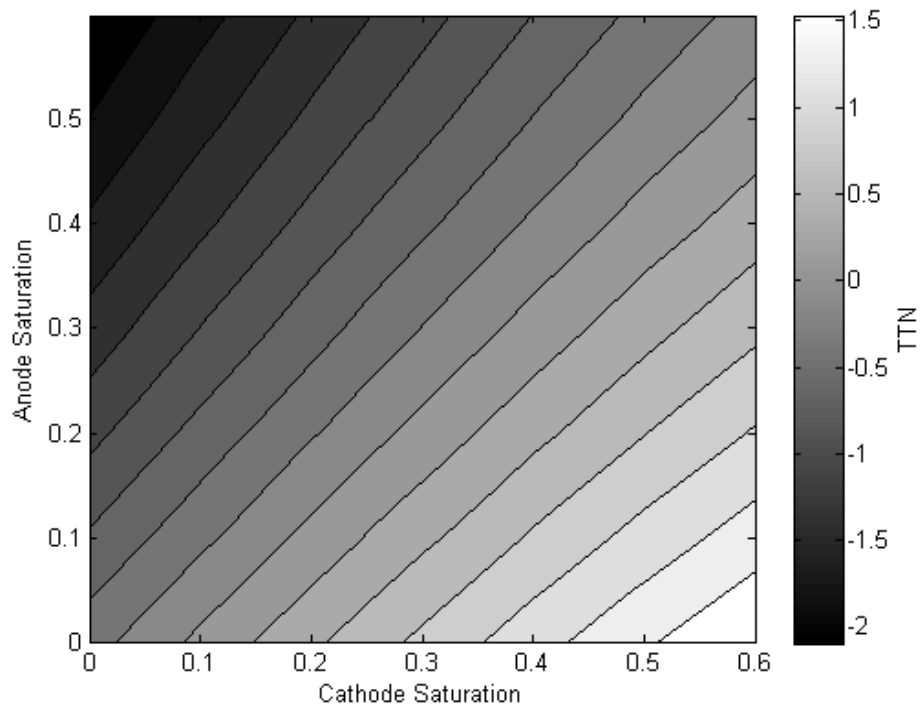
Figure 8-7: TTN distribution map for anode and cathode liquid water saturation. Top: without thermal conductivity effects, Bottom: with thermal conductivity effects.

8.3.4 Diffusion Media Tortuosity

Increasing tortuosity is a way to increase diffusion resistance without necessarily altering porosity. An example of this was shown in Chapter 6 where tortuosity was increased from 1.5 to 7.75 with a small increase in porosity when compared to a standard commercially available material. Increasing diffusion resistance would influence PCI flow by restricting diffusion and acting as a limiter on maximum flux. This is beneficial when it is desired to control water balance. Normalized anode PCI flux is plotted in Figure 8-8 and shows that PCI flux can be restricted to less than 10% of the standard reference maximum by dramatically increasing the anode DM tortuosity. Alter tortuosity is one of the strongest influencers of PCI flow along with saturation.

Water balance can be strongly influenced as shown by the TTN distribution in Figure 8-9 with a large range of potential values from -3.1 to 2.3. The standard reference falls in the lower left corner of the plot where a relatively zero preference occurs. Increasing the tortuosity of either side can push the water balance to the opposite side thus altering the preferential direction of transport from the standard reference case. Although it is possible to increase the tortuosity of either the anode or cathode diffusion medium, it would only be beneficial on the anode side as the hydrogen reaction rate can be reduced some before harm to performance occurs unlike the cathode where oxygen restriction would lower cell performance.

8.3.5 Flow Field Land Width

Land width can have a strong impact on cell performance due to governing heat removal, lateral diffusion distances, water accumulation, mechanical stress, and cell
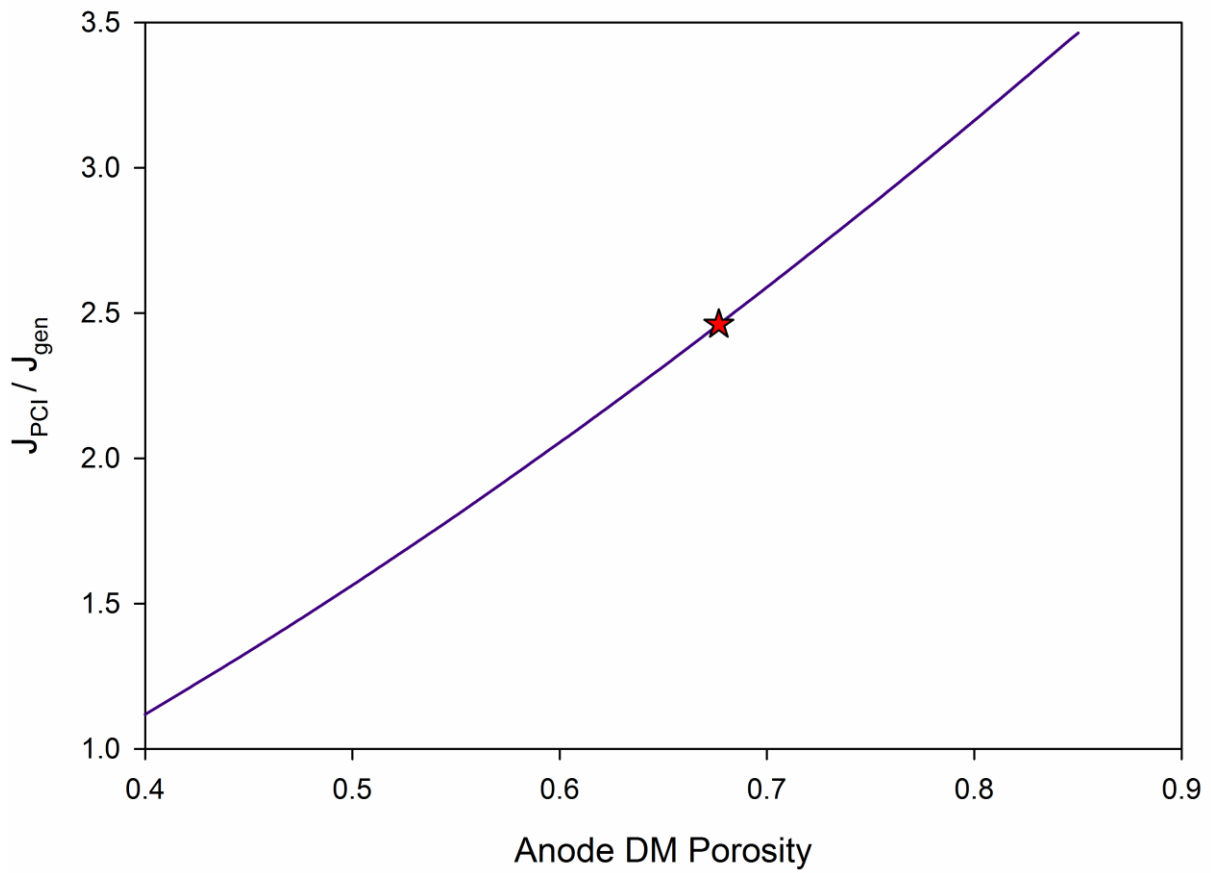
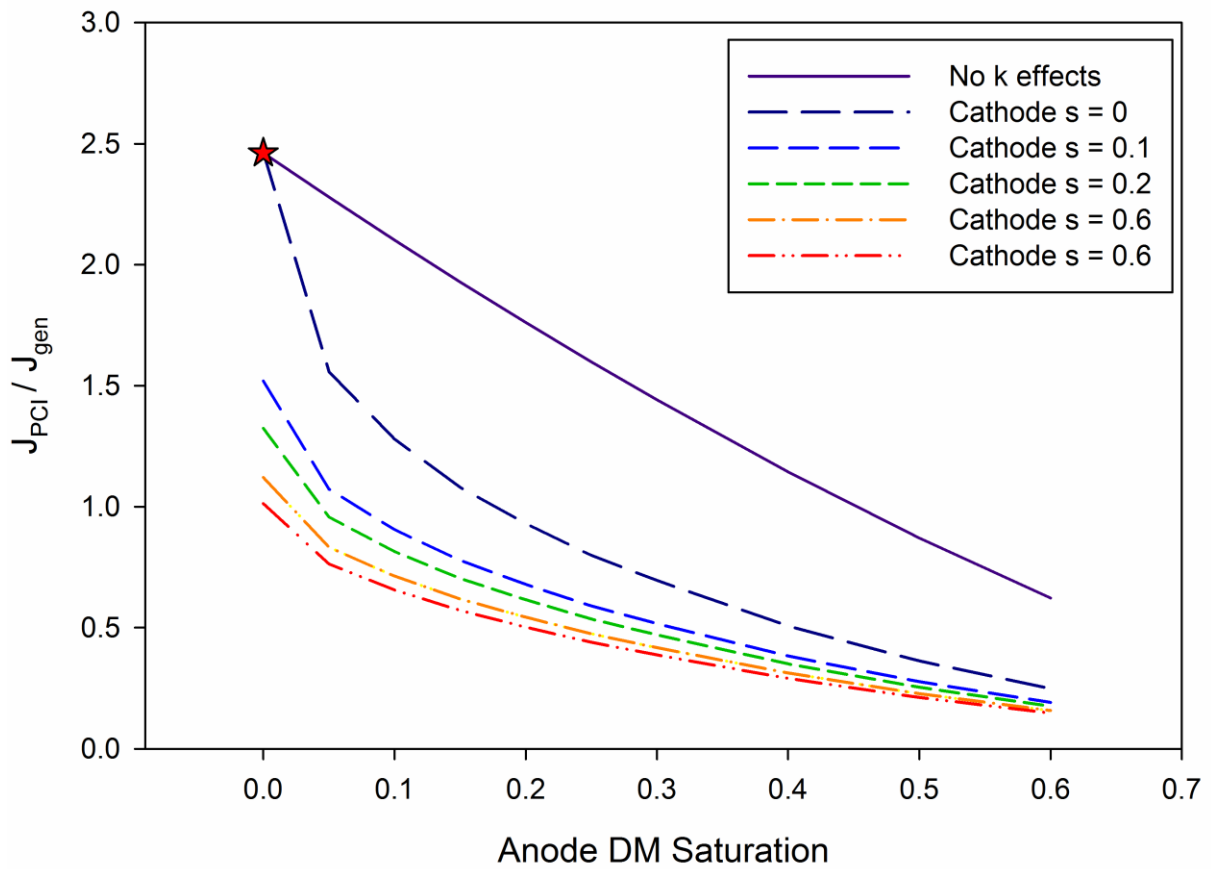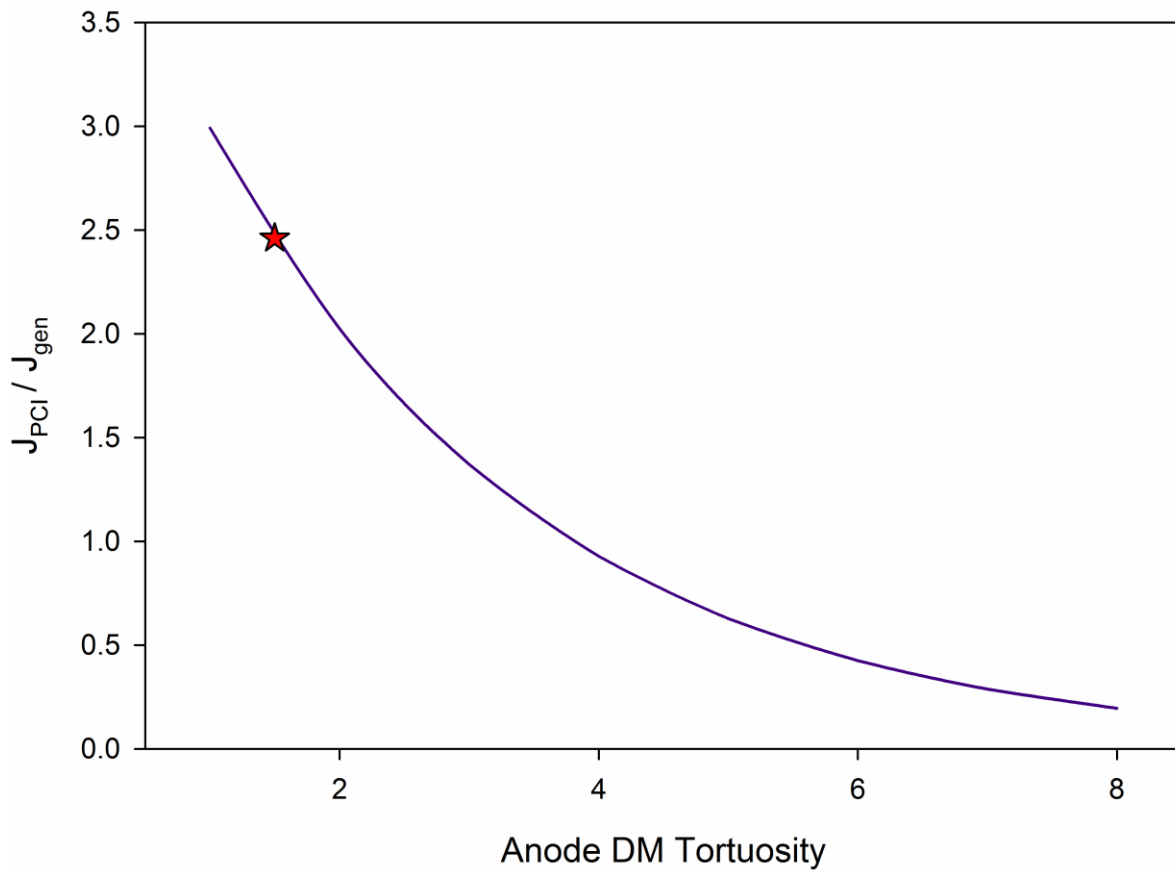Figure 8-8: Normalized anode PCI flux as a function of anode tortuosity. Star denotes study standard reference point.
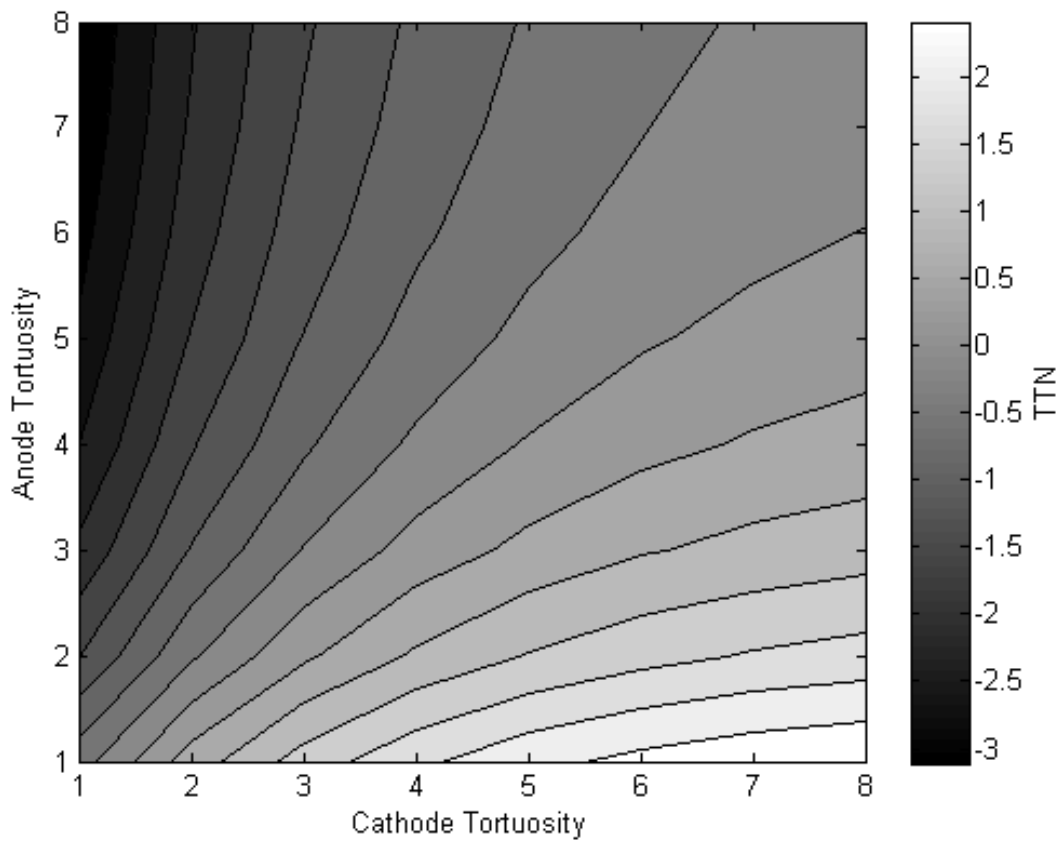
Figure 8-9: TTN distribution map for anode and cathode tortuosity variance.

electrical resistance. The property of concern for thermally driven transport is the heat removal of the lands as this affects the peak temperature and temperature distribution within the cell. To determine the influence of land width on PCI flux, Figure 8-10 plots PCI flux as a function of anode land width for the various cathode land widths. The smallest, 0.25 mm, cathode lands produce the highest peak temperature of all the land configurations due to the small heat removal area which results in the highest driving force possible but only improves the normalized flux from 2.25 to 2.6 for the symmetric cases. Larger anode lands and small cathode lands would be desirable to increase the PCI flux while the opposite could be used to decrease the amount of PCI flow in the anode.

Cell water balance preference is determined with the TTN distribution plot in Figure 8-11 below. Here it can be seen that land width has a moderate influence on overall cell water balance. The majority of land configurations show a preference towards cathode transport due to the higher temperature differential possible in the cathode compared to the anode. Since the TTN shows the ability to alter water balance, land width is an important parameter when designing a cell with improved thermally driven transport. This design must balance increasing thermally driven transport with diffusion resistance due to overly wide lands, increased cell resistance due to overly narrow lands, and mechanical stress on the materials.

8.3.6 Flow Field Channel Width

As with the land width, channel width governs heat removal, lateral diffusion distances, water accumulation, mechanical stress, and cell electrical resistance. In this
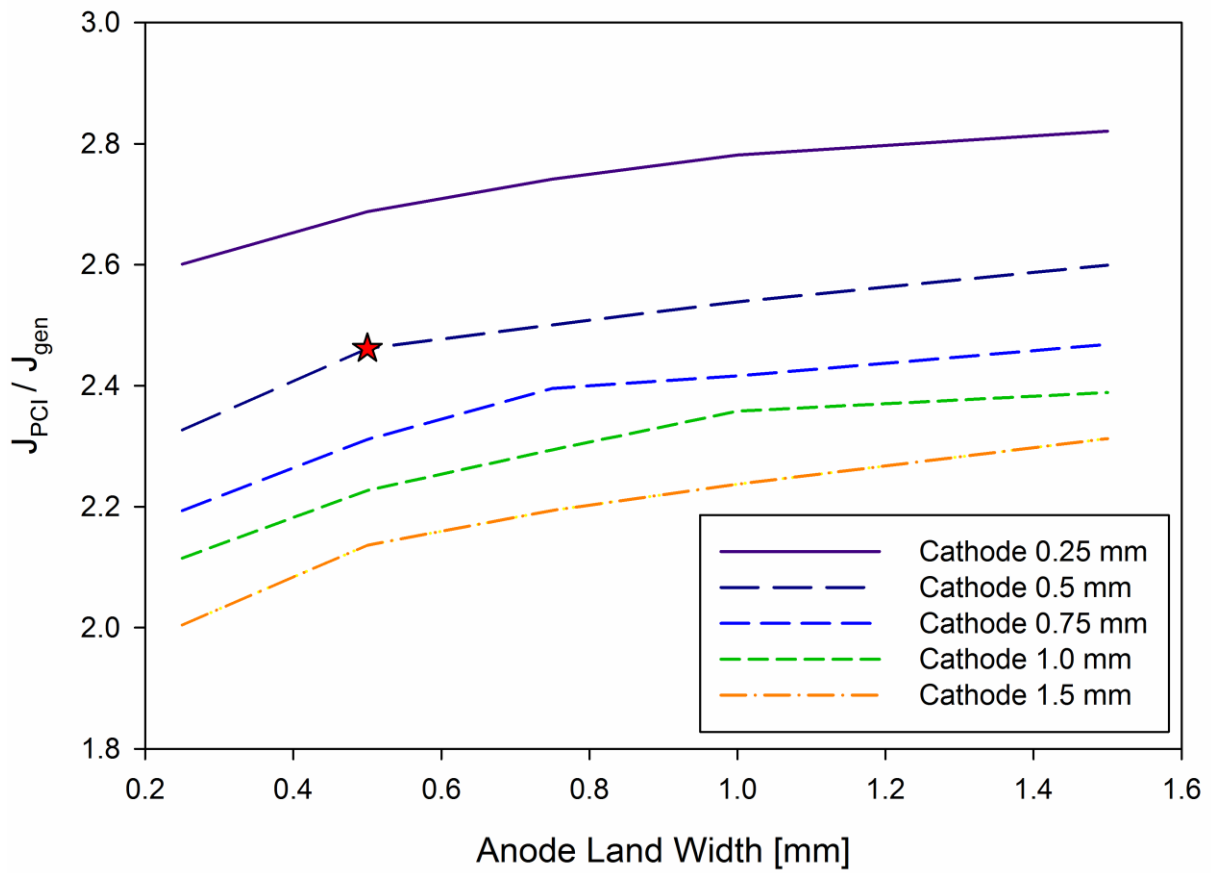
Figure 8-10: Normalized anode PCI flux as a function of anode land width with constant cathode land width lines. Star denotes study standard reference point.
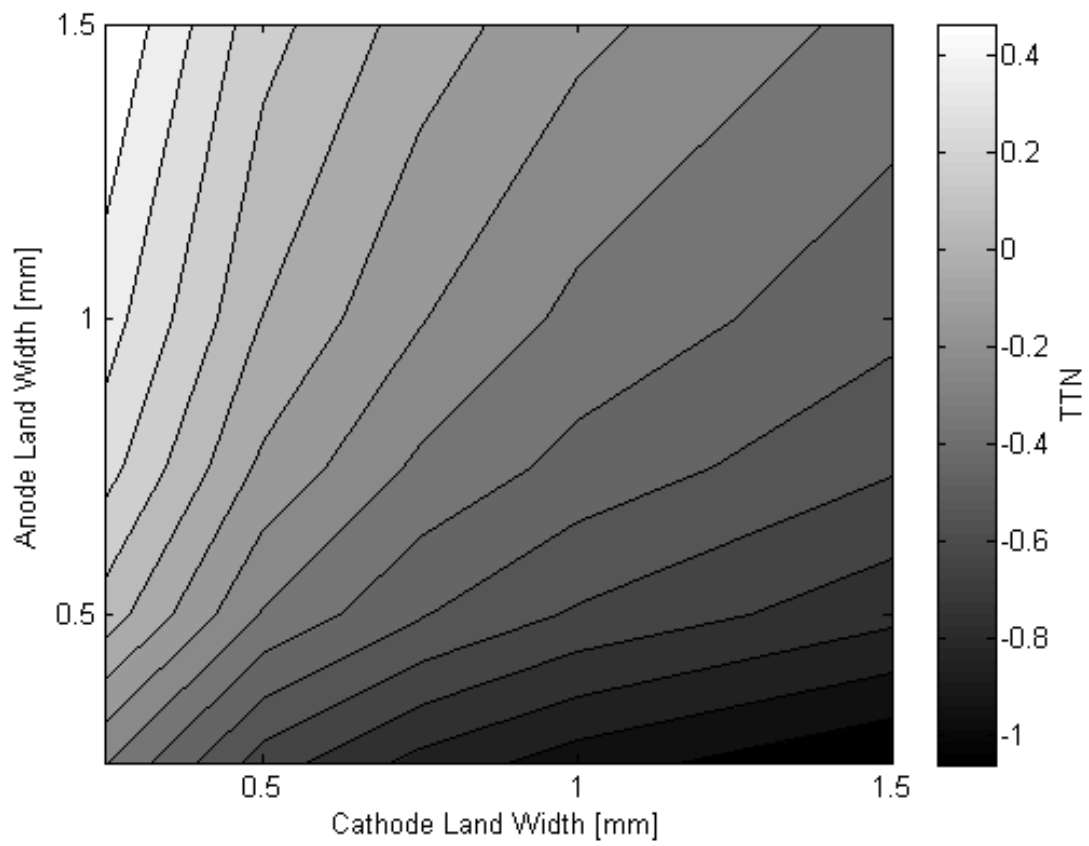
Figure 8-11: TTN distribution map for land width variance.

case, channel width influences heat removal by insulating the boundary over the channel. Normalized anode PCI flux as a function of anode channel width is given in Figure 8-12 along constant cathode channel width lines. PCI flux increases with increased cathode channel width due to the insulating effect of the channel increasing the peak temperature of the cell. The anode flux decreases with increasing anode channel width because the insulating effect of the channel decreases the temperature drop over a larger area with most PCI flux occurring in the regions over the lands. A reduction in anode channel width and/or an increase in cathode channel width is required to increase the anode PCI flux for this case.

Cell water balance is moderately influence by channel width as shown by the TTN distribution in Figure 8-13. The balance preference follows the opposite trend seen with the land width with increasing anode channel width pushing water balance towards the cathode. By increasing cathode channel width and reducing anode channel width, a temperature distribution can be established that preferentially transports water to the anode while the opposite preferentially drives water towards the cathode. Selection of channel width to provide water balance preference needs to be balanced with several other effects since large channels increase DM intrusion and reduce electrical contact area. The intrusion into the channel can cause issues with pressure drop and internal contact resistance between layers as the strain on the DM above the channel would be lower than the areas above the land.

8.4   Conclusions

A parametric study on the parameters that govern PCI flow has been performed in this chapter. Thermal conductivity, porosity, tortuosity, and saturation of the diffusion
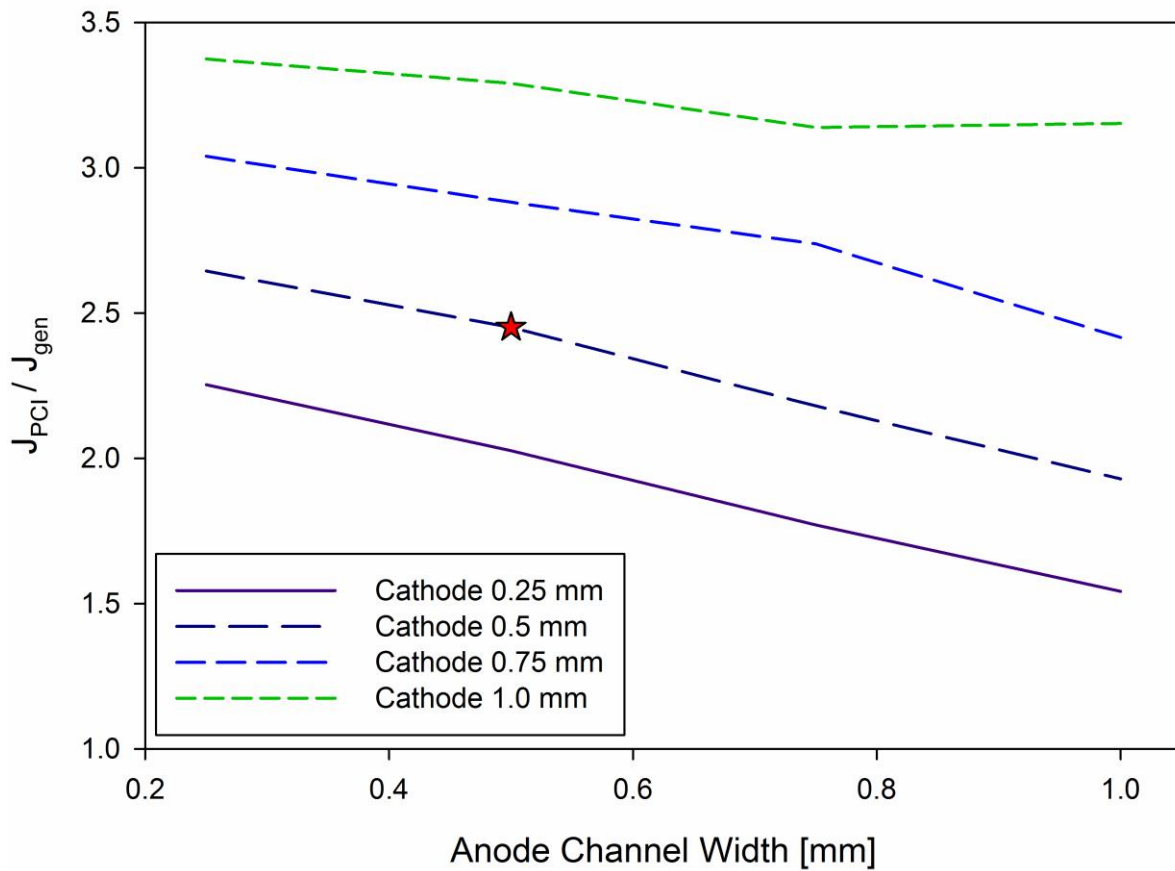
Figure 8-12: Normalized anode PCI flux as a function of anode channel width with constant cathode channel width lines. Star denotes study standard reference point.
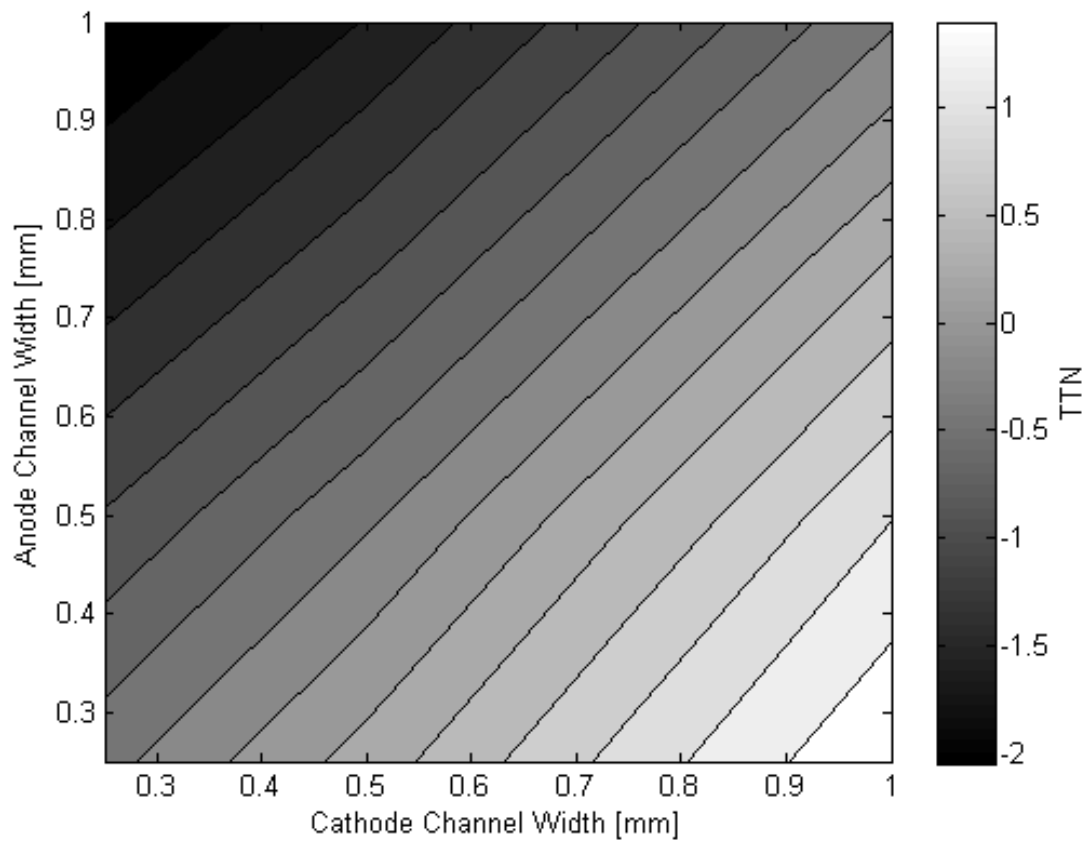
Figure 8-13: TTN distribution map for channel width variance.

media along with width of the channels and lands in the flow field were varied independently on the cathode and anode to determine if water transport to or from the anode was possible. It was found that tortuosity of the DM had the strongest influence on cell water balance for the standard geometry of this study while porosity, saturation, channel width, and land width had moderate influences on water balance. Thermal conductivity of the diffusion media was found to be an important parameter as it directly alters the temperature gradient across the diffusion media therefore controlling the maximum flux possible across the layer but was found to not have a significant role in cell water balance.

This work highlights the need to consider asymmetric geometries and material properties when designing a fuel cell. By altering the anode geometry and properties separately from the cathode, a desirable water balance can be designed into the cell. This balance can drive water to the anode in cases where anode dry out would be an issue or remove anode water in cases where anode flooding is an issue.

CHAPTER 9: Conclusions and Recommendations

9.1 Conclusions

This work has investigated coupled heat and mass transport of water in a polymer electrolyte fuel cell. High resolution neutron imaging coupled with a new non-dimensional transport number describe how water balance shifts in fuel cells due to the influence of channel-land architecture, diffusion media transport properties, and aging effects. These properties have shown strong influence on water balance and have driven a parametric study to determine how cell water balance can be engineered to optimize performance, start-up/shut-down efficiency, and durability.

Channel-land architecture has significant influence on cell water balance and water accumulation. By designing a flow field with large, 1.5 mm, anode lands and small, 0.5 mm, cathode lands, a ΔT inversion can be designed into the cell that facilitates water transport to the anode. This inversion is driven by the insulating effect that the cathode channel has that aligns with the center of the large anode land causing a small ΔT across the cathode while the cool anode land can support a large ΔT. The large lands also allow for greater storage than smaller lands that require greater accumulation before the water becomes connected enough to drain to the gas channels. When considering saturation effects on temperature and diffusion resistance this thermal driving force is greatly attenuated with a reduction of approximately 85%.

Tailoring of diffusion media transport properties has shown great promise in providing materials that can control the water accumulation in the cell. Larger anode lands coupled with small cathode lands provide benefits for performance and durability

by reducing shearing stress on the MEA but at the cost of high anode water accumulation that can result in purge difficulties and voltage reversals. To provide the benefits of this architecture while also reducing anode water content a new experimental high diffusion resistance anode diffusion media was tested. This material increases diffusion resistance by increasing the tortuosity of the material while maintaining similar porosity levels to commercially available DM. The experimental material proved effective at reducing water content by 66% over standard materials. Analysis of the individual property contributions to the overall transport behavior of the material found that the increased diffusion resistance would be enough to restrict water transport to the anode but was aided by the increased thermal conductivity of the experimental material. The increase in thermal conductivity from the commercial material 0.2 W/m-k to 0.9 W/m-k reduced the operating temperature of the cell and thus reduced the maximum amount of PCI flow through the cell.

Operational age of the MEA was found to have a strong influence on cell water balance and the thermal conductivity of the diffusion media. Water accumulation was reduced by over 50% from the virgin baseline case for materials that operated for 2666 hours in a fuel cell vehicle. The reduction in water was driven by increased surface functionalization, reduced wet-proofing, and increased thermal conductivity of the diffusion media. X-ray photoelectron spectroscopy found increased levels of carbon-oxygen bonds and a reduction in carbon-fluorine bonds which indicate an overall increase in the hydrophilic nature of the aged diffusion media. This increase allows for improved drainage to the channels by reducing the pressures necessary for capillary drainage. Thermal conductivity was found to increase from inlet to outlet and with

increasing age with the greatest changes occurring on the anode. These increases in conductivity drive the peak cell temperature down reducing the effects of PCI flow and the transport of water to the anode. The combined effect of reduced transport to the anode and the improved drainage drive the reduction in anode water content.

Engineering of the fuel cell architecture and material properties was shown to have a strong influence on water transport. A parametric study in this work found that DM thermal conductivity has a small effect on balance but controls the ΔT available for thermal transport and that porosity, tortuosity, and flow field architecture can be successfully used to control water accumulation within the cell. By carefully engineering the thermal management of the cell, water placement can be engineered to provide superior performance and durability.

9.2 Recommendations

This work has shown the important role of thermally driven transport of water in a fuel cell and how it can be engineered to provide beneficial water balance. Additional studies could be performed to enhance this understanding and provide greater details on the controllability of water content.

With the high probability of increased resolution to levels near 1 μm for neutron imaging with the advent of neutron microscopes it will be possible to probe the catalyst layers and MPLs of actual fuel cells. State-of-the-art catalyst layers and MPLs are on the order of 10 to 30 μm thick and are too thin to get any information on water content with current 15 μm resolution. Understanding of water transport within these layers will provide invaluable information on water generation, transport, and control. By

172

understanding these layers and their associated interfaces, engineering of cell water balance will greatly improve.

Although this work touched on many aspects that can be engineered to control water transport and accumulation within a cell, a more comprehensive validation is warranted to prove the effectiveness of the TTN in predicting water balance in a cell. Neutron imaging data for a greater number of commercial diffusion media with varying thermal conductivity and transport resistances, channel-land architecture, and imposed gradients would provide rich information to match to predicted levels based on TTN. This work would require significant beam-time allotments and optimization on testing parameters to produce the most efficient set of data. The channel-land architecture of this work could also be extended to advanced flow field design that utilize metallic foams instead of the standard land channel. This type of architecture could provide interesting engineering challenges in designing foam materials that can produce thermal effects similar to the channel-land architecture while still providing the superior gas distribution of foam.

Operational age has been shown to have significant influence on cell water balance in this work with material characterization sufficient to describe what was seen in the neutron images. Greater material characterization would be desired to gain an understanding on how to prevent the degradation modes that result in increased thermal conductivity and hydrophilic nature. This would ensure that any thermal considerations that are engineered into the cell at start-of-life will remain in place during the entire operational life of the fuel cell.

List of References

[1] W.R. Grove, Philosophical Magazine Series 3, 14 (1839) 127-130.

[2] M.M. Mench, Fuel Cell Engines, 2008.

[3] M.L. Perry, T.F. Fuller, Journal of The Electrochemical Society, 149 (2002) S59-S67.

[4] A.A. Kornyshev, A.M. Kuznetsov, E. Spohr, J. Ulstrup, The Journal of Physical Chemistry B, 107 (2003) 3351-3366.

[5] A.Z. Weber, J. Newman, Journal of The Electrochemical Society, 151 (2004) A311-A325.

[6] M. Khandelwal, M.M. Mench, Journal of Power Sources, 161 (2006) 1106-1115.

[7] M.F. Mathias, J. Roth, J. Fleming, W. Lehnert, Diffusion Media Materials and Characterization, in: W. Vielstich, A. Lamm, H.A. Gasteiger (Eds.) Handbook of Fuel Cells - Fundamentals, Technology and Applications, Wiley, 2003.

[8] K.T. Cho, M.M. Mench, Physical Chemistry Chemical Physics, 14 (2012) 4296-4302.

[9] Z. Fishman, A. Bazylak, Journal of The Electrochemical Society, 158 (2011) B846-B851.

[10] F.E. Hizir, S.O. Ural, E.C. Kumbur, M.M. Mench, Journal of Power Sources, 195 (2010) 3463-3471.

[11] M.S. Ismail, D. Borman, T. Damjanovic, D.B. Ingham, M. Pourkashanian, International Journal of Hydrogen Energy, 36 (2011) 10392-10402.

[12] Z. Lu, S.G. Kandlikar, C. Rath, M. Grimm, W. Domigan, A.D. White, M. Hardbarger, J.P. Owejan, T.A. Trabold, International Journal of Hydrogen Energy, 34 (2009) 3445-3456.

[13] J.M. Sergi, S.G. Kandlikar, International Journal of Hydrogen Energy, 36 (2011) 12381-12392.

[14] J.P. Owejan, T.A. Trabold, D.L. Jacobson, D.R. Baker, D.S. Hussey, M. Arif, International Journal of Heat and Mass Transfer, 49 (2006) 4721-4731.

[15] S. von Dahlen, M.H. Bayer, I.A. Schneider, Electrochemistry Communications, 14 (2012) 55-58.

[16] J.P. Feser, A.K. Prasad, S.G. Advani, Journal of Power Sources, 161 (2006) 404-412.

[17] S.G. Goebel, Journal of Power Sources, 196 (2011) 7550-7554.

[18] K.T. Cho, M.M. Mench, International Journal of Hydrogen Energy, 35 (2010) 12329-12340.

[19] É. Fontana, E. Mancusi, A. da Silva, V.C. Mariani, A.A. Ulson de Souza, S.M.A.G. Ulson de Souza, International Journal of Heat and Mass Transfer, 54 (2011) 4462-4472.

[20] P. Oberholzer, P. Boillat, A. Kaestner, E.H. Lehmann, G.G. Scherer, T.J. Schmidt, A. Wokaun, Journal of The Electrochemical Society, 160 (2013) F659-F669.

[21] J.P. Owejan, T.A. Trabold, D.L. Jacobson, M. Arif, S.G. Kandlikar, International Journal of Hydrogen Energy, 32 (2007) 4489-4502.

[22] A. Higier, H. Liu, International Journal of Hydrogen Energy, 35 (2010) 2144-2150.

[23] R. Flückiger, S.A. Freunberger, D. Kramer, A. Wokaun, G.G. Scherer, F.N. Büchi, Electrochimica Acta, 54 (2008) 551-559.

[24] D. Kramer, S.A. Freunberger, R. Flückiger, I.A. Schneider, A. Wokaun, F.N. Büchi, G.G. Scherer, Journal of Electroanalytical Chemistry, 612 (2008) 63-77.

[25] J.M. LaManna, S.G. Kandlikar, International Journal of Hydrogen Energy, 36 (2011) 5021-5029.

[26] N. Astrath, J. Shen, D. Song, J. Rohling, F. Astrath, J. Zhou, T. Navessin, Z.S. Liu, C. Gu, X. Zhao, Physical Chemistry, 113 (2009) 8369-8374.

[27] D.R. Baker, D.A. Caulk, K.C. Neyerlin, M.W. Murphy, Journal of The Electrochemical Society, 156 (2009) B991-B1003.

[28] C. Quick, D. Ritzinger, W. Lehnert, C. Hartnig, Journal of Power Sources, 190 (2009) 110-120.

[29] U. Beuscher, Journal of The Electrochemical Society, 153 (2006) A1788-A1793.

[30] D.R. Baker, C. Wieser, K.C. Neyerlin, M.W. Murphy, ECS Transactions, 3 (2006) 989-999.

[31] J.M. Morgan, R. Datta, Journal of Power Sources.

[32] J. Stumper, M. Löhr, S. Hamada, Journal of Power Sources, 143 (2005) 150-157.

[33] M.S. Ismail, T. Damjanovic, K. Hughes, D.B. Ingham, L. Ma, M. Pourkashanian, M. Rosli, Journal of Fuel Cell Science and Technology, 7 (2010) 051016-051016.

[34] Y.-I. Chou, Z.-Y. Siao, Y.-F. Chen, L.-Y. Sung, W.-M. Yang, C.-C. Wang, Journal of Power Sources, 195 (2010) 536-540.

[35] J.T. Gostick, M.W. Fowler, M.D. Pritzker, M.A. Ioannidis, L.M. Behra, Journal of Power Sources, 162 (2006) 228-238.

[36] H. Ito, K. Abe, M. Ishida, A. Nakano, T. Maeda, T. Munakata, H. Nakajima, T. Kitahara, Journal of Power Sources.

[37] J.G. Pharoah, Journal of Power Sources, 144 (2005) 77-82.

[38] C.-J. Hung, C.-H. Liu, T.-H. Ko, W.-H. Chen, S.-H. Cheng, W.-S. Chen, A. Yu, A.M. Kannan, Journal of Power Sources.

[39] K. Tüber, D. Pócza, C. Hebling, Journal of Power Sources, 124 (2003) 403-414.

[40] J. Lobato, P. Cañizares, M. Rodrigo, C. Ruiz-López, J. Linares, Journal of Applied Electrochemistry, 38 (2008) 793-802.

[41] G.-G. Park, Y.-J. Sohn, T.-H. Yang, Y.-G. Yoon, W.-Y. Lee, C.-S. Kim, Journal of Power Sources, 131 (2004) 182-187.

[42] R. Alink, J. Haußmann, H. Markötter, M. Schwager, I. Manke, D. Gerteisen, Journal of Power Sources, 233 (2013) 358-368.

[43] M.P. Manahan, M.C. Hatzell, E.C. Kumbur, M.M. Mench, Journal of Power Sources, 196 (2011) 5573-5582.

[44] M.P. Manahan, M.M. Mench, Journal of The Electrochemical Society, 159 (2012) F322-F330.

[45] R. Alink, D. Gerteisen, M. Oszcipok, Journal of Power Sources, 182 (2008) 175-187.

[46] J. Ihonen, M. Mikkola, G. Lindbergh, Journal of The Electrochemical Society, 151 (2004) A1152-A1161.

[47] S.G. Kandlikar, Z. Lu, Journal of Fuel Cell Science and Technology, 6 (2009) 044001-044013.

[48] E.C. Kumbur, M.M. Mench, FUEL CELLS – PROTON-EXCHANGE MEMBRANE FUEL CELLS | Water Management, in: G. Editor-in-Chief: Jürgen (Ed.) Encyclopedia of Electrochemical Power Sources, Elsevier, Amsterdam, 2009, pp. 828-847.

[49] H. Li, Y. Tang, Z. Wang, Z. Shi, S. Wu, D. Song, J. Zhang, K. Fatih, J. Zhang, H. Wang, Z. Liu, R. Abouatallah, A. Mazza, Journal of Power Sources, 178 (2008) 103-117.

[50] P. Deevanhxay, T. Sasabe, S. Tsushima, S. Hirai, Journal of Power Sources, 230 (2013) 38-43.

[51] P. Krüger, H. Markötter, J. Haußmann, M. Klages, T. Arlt, J. Banhart, C. Hartnig, I. Manke, J. Scholta, Journal of Power Sources, 196 (2011) 5250-5255.

[52] Z. Dunbar, R.I. Masel, Journal of Power Sources, 171 (2007) 678-687.

[53] K.W. Feindel, S.H. Bergens, R.E. Wasylishen, Physical Chemistry Chemical Physics, 9 (2007) 1850-1857.

[54] M.M. Daino, Z. Lu, J.M. LaManna, J.P. Owejan, T.A. Trabold, S.G. Kandlikar, Electrochemical and Solid-State Letters, 14 (2011) B51-B54.

[55] D.S. Hussey, D.L. Jacobson, M. Arif, J.P. Owejan, J.J. Gagliardo, T.A. Trabold, Journal of Power Sources, 172 (2007) 225-228.

[56] E.H. Lehmann, P. Boillat, G. Scherrer, G. Frei, Nuclear Instruments and Methods in Physics Research Section A: Accelerators, Spectrometers, Detectors and Associated Equipment, 605 (2009) 123-126.

[57] H. Murakawa, D. Wada, K. Sugimoto, H. Asano, N. Takenaka, R. Yasuda, Nuclear Instruments and Methods in Physics Research Section A: Accelerators, Spectrometers, Detectors and Associated Equipment, 651 (2011) 286-289.

[58] P. Boillat, D. Kramer, B.C. Seyfang, G. Frei, E. Lehmann, G.G. Scherer, A. Wokaun, Y. Ichikawa, Y. Tasaki, K. Shinohara, Electrochemistry Communications, 10 (2008) 546-550.

[59] P. Boillat, G.G. Scherer, A. Wokaun, G. Frei, E.H. Lehmann, Electrochemistry Communications, 10 (2008) 1311-1314.

[60] P. Boillat, P. Oberholzer, R. Perego, R. Siegrist, A. Kaestner, E.H. Lehmann, G.G. Scherer, A. Wokaun, ECS Transactions, 41 (2011) 27-38.

[61] R. Yasuda, K. Nittoh, C. Konagai, M. Shiozawa, N. Takenaka, H. Asano, H. Murakawa, K. Sugimoto, T. Nojima, H. Hayashida, H. Iikura, T. Sakai, M. Matsubayashi, Nuclear Instruments and Methods in Physics Research Section A: Accelerators, Spectrometers, Detectors and Associated Equipment, 651 (2011) 268-272.

[62] D.S. Hussey, D.L. Jacobson, M. Arif, K.J. Coakley, D.F. Vecchia, Journal of Fuel Cell Science and Technology, 7 (2010) 021024-021024.

[63] D.S. Hussey, D. Spernjak, A.Z. Weber, R. Mukundan, J. Fairweather, E.L. Brosha, J. Davey, J.S. Spendelow, D.L. Jacobson, R.L. Borup, Journal of Applied Physics, 112 (2012) 104906-104913.

[64] M.A. Hickner, N.P. Siegel, K.S. Chen, D.S. Hussey, D.L. Jacobson, M. Arif, Journal of The Electrochemical Society, 155 (2008) B427-B434.

[65] D. Spernjak, P.P. Mukherjee, R. Mukundan, J. Davey, D.S. Hussey, D. Jacobson, R.L. Borup, ECS Transactions, 33 (2010) 1451-1456.

[66] A.Z. Weber, M.A. Hickner, Electrochimica Acta, 53 (2008) 7668-7674.

[67] S. Kim, M.M. Mench, Journal of The Electrochemical Society, 156 (2009) B353-B362.

[68] M.C. Hatzell, A. Turhan, S. Kim, D.S. Hussey, D.L. Jacobson, M.M. Mench, Journal of The Electrochemical Society, 158 (2011) B717-B726.

[69] R.S. Fu, J.S. Preston, U. Pasaogullari, T. Shiomi, S. Miyazaki, Y. Tabuchi, D.S. Hussey, D.L. Jacobson, Journal of The Electrochemical Society, 158 (2011) B303-B312.

[70] R.S. Fu, U. Pasaogullari, T. Shiomi, Y. Tabuchi, D.S. Hussey, D.L. Jacobson, Journal of The Electrochemical Society, 159 (2012) F545-F553.

[71] J. Mishler, Y. Wang, P.P. Mukherjee, R. Mukundan, R.L. Borup, Electrochimica Acta, 65 (2012) 127-133.

[72] P. Oberholzer, P. Boillat, R. Siegrist, R. Perego, A. Kästner, E. Lehmann, G.G. Scherer, A. Wokaun, Journal of The Electrochemical Society, 159 (2011) B235-B245.

[73] C. Chacko, R. Ramasamy, S. Kim, M. Khandelwal, M. Mench, Journal of The Electrochemical Society, 155 (2008) B1145-B1154.

[74] R. Mukundan, J. Davey, J.D. Fairweather, D. Spernjak, J.S. Spendelow, D.S. Hussey, D. Jacobson, P. Wilde, R. Schweiss, R.L. Borup, ECS Transactions, 33 (2010) 1109-1114.

[75] A. Turhan, S. Kim, M. Hatzell, M.M. Mench, Electrochimica Acta, 55 (2010) 2734-2745.

[76] Y. Tabuchi, T. Shiomi, O. Aoki, N. Kubo, K. Shinohara, Electrochimica Acta, 56 (2010) 352-360.

[77] A. Bazylak, International Journal of Hydrogen Energy, 34 (2009) 3845-3857.

[78] P. Deevanhxay, T. Sasabe, S. Tsushima, S. Hirai, International Journal of Hydrogen Energy, In Press, Corrected Proof.

[79] R. Flückiger, F. Marone, M. Stampanoni, A. Wokaun, F.N. Büchi, Electrochimica Acta, 56 (2011) 2254-2262.

[80] I. Manke, C. Hartnig, M. Grünerbel, W. Lehnert, N. Kardjilov, A. Haibel, A. Hilger, J. Banhart, H. Riesemeier, Applied Physics Letters, 90 (2007) -.

[81] H. Markötter, R. Alink, J. Haußmann, K. Dittmann, T. Arlt, F. Wieder, C. Tötzke, M. Klages, C. Reiter, H. Riesemeier, J. Scholta, D. Gerteisen, J. Banhart, I. Manke, International Journal of Hydrogen Energy.

[82] H. Markötter, J. Haußmann, R. Alink, C. Tötzke, T. Arlt, M. Klages, H. Riesemeier, J. Scholta, D. Gerteisen, J. Banhart, I. Manke, Electrochemistry Communications.

[83] H. Markötter, I. Manke, P. Krüger, T. Arlt, J. Haussmann, M. Klages, H. Riesemeier, C. Hartnig, J. Scholta, J. Banhart, Electrochemistry Communications, In Press, Accepted Manuscript.

[84] S. Tsushima, S. Hirai, Progress in Energy and Combustion Science, 37 (2011) 204-220.

[85] R. Satija, D.L. Jacobson, M. Arif, S.A. Werner, Journal of Power Sources, 129 (2004) 238-245.

[86] R. Mosdale, G. Gebel, M. Pineri, Journal of Membrane Science, 118 (1996) 269-277.

[87] R.J. Bellows, M.Y. Lin, M. Arif, A.K. Thompson, D. Jacobson, Journal of The Electrochemical Society, 146 (1999) 1099-1103.

[88] A. Turhan, K. Heller, J.S. Brenizer, M.M. Mench, Journal of Power Sources, 180 (2008) 773-783.

[89] D. Kramer, E. Lehmann, G. Frei, P. Vontobel, A. Wokaun, G.G. Scherer, Nuclear Instruments and Methods in Physics Research Section A: Accelerators, Spectrometers, Detectors and Associated Equipment, 542 (2005) 52-60.

[90] D. Kramer, J. Zhang, R. Shimoi, E. Lehmann, A. Wokaun, K. Shinohara, G.G. Scherer, Electrochimica Acta, 50 (2005) 2603-2614.

[91] T.A. Trabold, J.P. Owejan, D.L. Jacobson, M. Arif, P.R. Huffman, International Journal of Heat and Mass Transfer, 49 (2006) 4712-4720.

[92] D.S. Hussey, D.L. Jacobson, High-Resolution Neutron Radiography Analysis of Proton Exchange Membrane Fuel Cells, in: C.-Y. Wang, U. Pasaogullari (Eds.) Modeling and Diagnostics of Polymer Electrolyte Fuel Cells, Springer New York, 2010, pp. 175-200.

[93] D.S. Hussey, D.L. Jacobson, Neutron radiography for high-resolution studies in low temperature fuel cells, in: C. Hartnig, C. Roth (Eds.) Polymer Electrolyte Membrane and Direct Methanol Fuel Cell Technology, Vol 2: In Situ Characterization Techniques for Low Temperature Fuel Cells, Woodhead Publ Ltd, Cambridge, 2012, pp. 188-213.

[94] Y. Ashraf Gandomi, M.M. Mench, ECS Transactions, 58 (2013) 1375-1382.

[95] A.K. Srouji, L.J. Zheng, R. Dross, A. Turhan, M.M. Mench, Journal of Power Sources, 239 (2013) 433-442.

[96] A.K. Srouji, L.J. Zheng, R. Dross, A. Turhan, M.M. Mench, Journal of Power Sources, 218 (2012) 341-347.

[97] J.M. LaManna, S. Chakraborty, J.J. Gagliardo, M.M. Mench, International Journal of Hydrogen Energy, 39 (2014) 3387-3396.

[98] Y. Wang, K.S. Chen, Journal of The Electrochemical Society, 157 (2010) B1878-B1886.

[99] J.S. Preston, R.S. Fu, U. Pasaogullari, D.S. Hussey, D.L. Jacobson, Journal of The Electrochemical Society, 158 (2011) B239-B246.

[100] www.pemfcdata.org, in.

[101] J.P. Owejan, J.J. Gagliardo, J.M. Sergi, S.G. Kandlikar, T.A. Trabold, International Journal of Hydrogen Energy, 34 (2009) 3436-3444.

[102] L.J. Zheng, A.K. Srouji, R. Dross, A. Turhan, M.M. Mench, Journal of The Electrochemical Society, 160 (2013) F119-F128.

[103] O.H.W. Siegmund, J.V. Vallerga, A. Martin, B. Feller, M. Arif, D.S. Hussey, D.L. Jacobson, Nuclear Instruments and Methods in Physics Research Section A: Accelerators, Spectrometers, Detectors and Associated Equipment, 579 (2007) 188-191.

[104] D.S. Hussey, D.L. Jacobson, Neutron radiography for high-resolution studies in low temperature fuel cells, in: C.R. C Hartnig (Ed.) Polymer electrolyte membrane and direct methanol fuel cell technology: In situ characterization techniques for low temperature fuel cells, Woodhead Publishing Ltd, 2012.

[105] S.G. Kandlikar, Z. Lu, Applied Thermal Engineering, 29 (2009) 1276-1280.

[106] G. Xu, J.M. LaManna, J.T. Clement, M.M. Mench, Journal of Power Sources, 256 (2014) 212-219.

[107] Y. Wang, C.-Y. Wang, Journal of The Electrochemical Society, 153 (2006) A1193-A1200.

[108] M. Khandelwal, M.M. Mench, Journal of Power Sources, 195 (2010) 6549-6558.

[109] Z.Y. Liu, B.K. Brady, R.N. Carter, B. Litteer, M. Budinski, J.K. Hyun, D.A. Muller, Journal of The Electrochemical Society, 155 (2008) B979-B984.

[110] J. Chen, J.B. Siegel, T. Matsuura, A.G. Stefanopoulou, Journal of The Electrochemical Society, 158 (2011) B1164-B1174.

[111] J.P. Owejan, J.J. Gagliardo, S.R. Falta, T.A. Trabold, Journal of The Electrochemical Society, 156 (2009) B1475-B1483.

[112] R.B. Montgomery, Journal of Meteorology, 4 (1947) 193-196.

[113] S. Kim, M.M. Mench, Journal of Membrane Science, 328 (2009) 113-120.

[114] J.M. LaManna, J.V. Bothe Jr, F.Y. Zhang, M.M. Mench, Journal of Power Sources, 271 (2014) 180-186.

[115] R. Zaffou, H.R. Kunz, J.M. Fenton, ECS Transactions, 3 (2006) 909-913.

[116] R. Zaffou, J.S. Yi, H.R. Kunz, J.M. Fenton, Electrochemical and Solid-State Letters, 9 (2006) A418-A422.

[117] T. Ha, J. Cho, J. Park, K. Min, H.-S. Kim, E. Lee, J.-Y. Jyoung, International Journal of Hydrogen Energy, 36 (2011) 12436-12443.

[118] M.L. Perry, T. Patterson, C. Reiser, ECS Transactions, 3 (2006) 783-795.

[119] W. Gu, in: USDOE Fuel Cell Program Annual Merit Review, 2013.

[120] W. Gu, in: USDOE Fuel Cell Program Annual Merit Review, 2014.

[121] J.M. LaManna, J.V. Bothe Jr, F.Y. Zheng, M.M. Mench, Journal of Power Sources.

[122] USCAR, (2013).

[123] J. Péron, Y. Nedellec, D.J. Jones, J. Rozière, Journal of Power Sources, 185 (2008) 1209-1217.

[124] L. Kim, C.G. Chung, Y.W. Sung, J.S. Chung, Journal of Power Sources, 183 (2008) 524-532.

[125] Y. Zhang, S. Chen, Y. Wang, W. Ding, R. Wu, L. Li, X. Qi, Z. Wei, Journal of Power Sources, 273 (2015) 62-69.

[126] A.A. Franco, M. Gerard, Journal of The Electrochemical Society, 155 (2008) B367-B384.

[127] J. Speder, A. Zana, I. Spanos, J.J.K. Kirkensgaard, K. Mortensen, M. Hanzlik, M. Arenz, Journal of Power Sources, 261 (2014) 14-22.

[128] C. Lim, L. Ghassemzadeh, F. Van Hove, M. Lauritzen, J. Kolodziej, G.G. Wang, S. Holdcroft, E. Kjeang, Journal of Power Sources, 257 (2014) 102-110.

[129] B. Wu, M. Zhao, W. Shi, W. Liu, J. Liu, D. Xing, Y. Yao, Z. Hou, P. Ming, J. Gu, Z. Zou, International Journal of Hydrogen Energy, 39 (2014) 14381-14390.

[130] J. Wu, J.J. Martin, F.P. Orfino, H. Wang, C. Legzdins, X.-Z. Yuan, C. Sun, Journal of Power Sources, 195 (2010) 1888-1894.

[131] R.A. Antunes, M.C.L. Oliveira, G. Ett, V. Ett, International Journal of Hydrogen Energy, 35 (2010) 3632-3647.

[132] M.F. Peker, Ö.N. Cora, M. Koç, International Journal of Hydrogen Energy, 36 (2011) 15427-15436.

[133] O.S. Burheim, G. Ellila, J.D. Fairweather, A. Labouriau, S. Kjelstrup, J.G. Pharoah, Journal of Power Sources.

Appendix

Table A-1: Cell voltage values for Chapter 3 conditions

Figure	Condition (anode|cathode)	Voltage [V]
Fig 3-3, Fig 3-4	40°C, 100|150 kPa, 0.8 A/cm^2	0.608
Fig 3-3, Fig 3-4	40°C, 150|150 kPa, 0.8 A/cm^2	0.690
Fig 3-3, Fig 3-4	40°C, 150|100 kPa, 0.8 A/cm^2	0.701
Fig 3-3, Fig 3-4	60°C, 100|150 kPa, 0.8 A/cm^2	0.658
Fig 3-3, Fig 3-4	60°C, 150|150 kPa, 0.8 A/cm^2	0.695
Fig 3-3, Fig 3-4	60°C, 150|100 kPa, 0.8 A/cm^2	0.699
Fig 3-3, Fig 3-5	80°C, 100|150 kPa, 0.8 A/cm^2	0.670
Fig 3-3, Fig 3-5	80°C, 150|150 kPa, 0.8 A/cm^2	0.665
Fig 3-3, Fig 3-5	80°C, 150|100 kPa, 0.8 A/cm^2	0.619
Fig 3-5	80°C, 100|150 kPa, 1.5 A/cm^2	0.496
Fig 3-5	80°C, 150|150 kPa, 1.5 A/cm^2	0.508
Fig 3-5	80°C, 150|100 kPa, 1.5 A/cm^2	0.383
Fig 3-9	60°C, 50%|95%, 0.1 A/cm^2	0.836
Fig 3-9	60°C, 50%|95%, 0.4 A/cm^2	0.763
Fig 3-9	60°C, 50%|95%, 0.8 A/cm^2	0.709
Fig 3-9, Fig 3-11	60°C, 50%|95%, 1.2 A/cm^2	0.667
Fig 3-6, Fig 3-7, Fig 3-9	60°C, 50%|95%, 1.5 A/cm^2	0.595
Fig 3-9	60°C, 50%|50%, 0.1 A/cm^2	0.839
Fig 3-9	60°C, 50%|50%, 0.4 A/cm^2	0.752
Fig 3-9	60°C, 50%|50%, 0.8 A/cm^2	0.708
Fig 3-9, Fig 3-11	60°C, 50%|50%, 1.2 A/cm^2	0.650
Fig 3-6, Fig 3-7, Fig 3-9	60°C, 50%|50%, 1.5 A/cm^2	0.598
Fig 3-9	60°C, 95%|50%, 0.1 A/cm^2	0.839
Fig 3-9	60°C, 95%|50%, 0.4 A/cm^2	0.756
Fig 3-9	60°C, 95%|50%, 0.8 A/cm^2	0.695
Fig 9, Fig 11	60°C, 95%|50%, 1.2 A/cm^2	0.576
Fig 3-6, Fig 3-7, Fig 3-9	60°C, 95%|50%, 1.5 A/cm^2	0.583
Fig 3-9	60°C, 95%|95%, 0.1 A/cm^2	0.826
Fig 3-9	60°C, 95%|95%, 0.4 A/cm^2	0.753
Fig 3-9	60°C, 95%|95%, 0.8 A/cm^2	0.695
Fig 3-9, Fig 3-11	60°C, 95%|95%, 1.2 A/cm^2	0.618
Fig 3-7, Fig 3-9	60°C, 95%|95%, 1.5 A/cm^2	0.580
Fig 3-6, Fig 3-8	80°C, 50%|95%, 1.5 A/cm^2	0.544
Fig 3-6, Fig 3-8	80°C, 50%|50%, 1.5 A/cm^2	0.495

Table A-1: Continued

Figure	Condition (anode|cathode)	Voltage [V]
Fig 3-6, Fig 3-8	80°C, 95%|50%, 1.5 A/cm^2	0.516
Fig 3-8	80°C, 95%|95%, 1.5 A/cm^2	0.508

Vita

Jacob M. LaManna was born in Syracuse, NY on December 1st, 1985, to Gerald and Susan LaManna. He grew up in Fabius, NY and graduated from the Fabius-Pompey High School in 2004. Jacob attended the Rochester Institute of Technology where he received his Bachelor of Science and Master of Science degrees in mechanical engineering in 2010. The focus of his Master's thesis was in effective diffusivity of water vapor in polymer electrolyte fuel cells. Jacob joined Professor Matthew Mench's Electrochemical Energy Storage and Conversion Laboratory at the University of Tennessee in August 2010 where he continued his work in fuel cells. He will graduate with his Ph.D. in mechanical engineering from the University of Tennessee in December, 2014.